Doctoral Dissertation

Nanostructured Thermoelectric Materials Fabricated using Chemically-synthesized Cu-Sn-S Based Nanoparticles as Building Blocks

Zhou Wei

Supervisor: Professor Shinya Maenosono

Graduate School of Advanced Science and Technology

Japan Advanced Institute of Science and Technology

Materials Science

September 2019

Abstract

Thermoelectric (TE) technique has attracted much attention due to the dramatical demand for energy conversion. The researches on TE materials is hotpot. However, most of the high efficiency TE materials contains toxicity and rare elements such as Te and Se that are not feasible for real application. To investigate the sustainable TE materials with high efficiency, copper tin sulfide (CTS), which emerged as promising TE material and has been widely studied for solar cells, was chosen as the target material because it contains environmentally friendly, earth abundance and low cost elements. However, it used as TE material is lack of understanding. The impacts of nanostructuring, Zn doping effect and grain size effect on the final TE performance of CTS material have been systematically investigated. This dissertation research surrounds on the work of CTS based nanoparticles (NPs) as building block for TE materials, which synthesized by chemical methods that can control over the size, shape, composition and structure of NPs. The fabrication approaches, characterizations and TE properties of the copper tin sulfide based materials are all presented in this work.

Chapter 1 gave a basic introduction of thermoelectricity and background about CTS material and its potential and challenges for being chosen as TE materials. A brief review of the chosen strategies to enhance the TE efficiency and current research work on CTS based TE materials have been given.

Chapter 2 demonstrated the chemically synthesized uniform hole-doped $Cu_2Sn_{1-x}Zn_xS_3$ (x=0-0.2) NPs and fabricated TE materials by sintering the NPs into dense bulk materials using pulse electric current sintering (PECS) technique after ligand exchange. Then, the structure and composition-property relationships in the $Cu_2Sn_{1-x}Zn_xS_3$ TE materials were analyzed. By introducing Zn doping effect and nanostructuring, the highest ZT value of 0.37 at 670 K was achieved in both $Cu_2Sn_{0.95}Zn_{0.05}S_3$ and $Cu_2Sn_{0.85}Zn_{0.15}S_3$ nanostructured materials, which was comparable to the ZT value at the same temperature of the $Cu_2Sn_{0.9}Zn_{0.1}S_3$ non-nanostructured material.

Chapter 3 described the one pot chemical method and hot injection method synthesized copper tin sulfide materials with controllable size, shape and structure. The resulting particles after ligand exchange were pelletized by using PECS technique for further TE measurements. The grain size effect and composition-property relationships in the CTS TE materials have been analyzed. It was found that the lattice thermal conductivities decreased with grain sizes and could be strongly suppressed when the grain size of pellet decreased to around 30nm. In addition, the ratio of Sn/Cu in CTS materials has been found to have huge effect on the carrier concertation.

Chapter 4 studied the enhanced TE properties of blended $Cu_2Sn_{1-x}Zn_xS_3$ nanobulk materials, which fabricated by sintering a mixture of chemically synthesized $Cu_2Sn_{0.85}Zn_{0.15}S_3$ (high σ and high κ) and $Cu_2Sn_{0.9}Zn_{0.1}S_3$ (low σ and low κ) NPs with different weight ratios into dense bulk materials by PECS technique. $Cu_2Sn_{0.85}Zn_{0.15}S_3$ has been used as a host material and $Cu_2Sn_{0.9}Zn_{0.1}S_3$ used as nanoinclusions. By using different chemical mixing methods, these two heterogeneous (but nearly identical) NPs were blended in a weight fraction of 9:1 for making a nanobulk material, the pellet showed ZT = 0.64 at 670 K, which is 1.7 and 1.9 times higher than the ZT values of the pristine $Cu_2Sn_{0.85}Zn_{0.15}S_3$ and $Cu_2Sn_{0.9}Zn_{0.1}S_3$ nanobulk materials, respectively.

Chapter 5 gave the general conclusions, and future prospects of the overall research work.

Keywords: Thermoelectric, Copper Tin Sulfides, Chemical Method, Nanoparticles, Size effect

Acknowledgements

Firstly, I would like to show the most sincere gratitude to my supervisor Prof. Shinya Maenosono. This thesis could not be finished without his support. During the research, his guidance and suggestion pointed me the way to close to the targets when I was in confusing moment. His patience and strictness made me try to become a better myself. Moreover, I also thank him for providing so many chances for me to practice my presentations for research work, which has been big challenges for me in the past time. During this short study time in Japan, I learnt a lot from him, not only the knowledge of research but also the attitude in work and life that is always keep enthusiasm.

I also express my heartiest thanks to Prof. Mikio Koyano to be my second supervisor. Every time, after the discussion with him, his idea and guidance always inspire me to expand large field of physical knowledge of thermoelectric. Thanks for him to support the PPMS machine and hot press machine for my experiments. I also would like to show my gratitude to Assist. Prof. Masanobu Miyata, he guided me for the sample preparation for hall measurement and electricity measurement. I really thank for his support in operating the PPMS machine and hot press machine. I learnt a lot from him not only physical knowledge but also his strict attitude in science work.

I also show my heartiest thanks to former Assist. Prof. Derrick Mott in Maenosono lab. I really thanks for his help in proofing scientific papers. His valuable comments in the group meeting really pointed towards new ideas in the field of my research. I also want to thank him for guiding me to arrange waste disposal in lab.

My thanks will go to Prof. Yoshifumi Oshima for accepting me to do minor research in his lab. His kindly guidance and discussions in the observation of my samples by using STEM technique strongly rich my knowledge of crystal structures of materials.

I would like to express my thanks to Mr. Takeo Akatsuka and Mr. Hiroshi Takida from Nippon Shokubai for helping me in operating the machine to make pellets by using pulsed electric current sintering (PECS) technique. I would like to show my gratitude to Dr. Michiro Ohta and Ms. Naoko Fujimoto from AIST for helping me in operating the machine for thermoelectric properties measurements. I also express my thanks to Dr. Koichi Higashimine from nanocenter of JAIST for helping in the observation of SAED and STEM-HADDF images of my samples that shown in this thesis.

I also express my sincere gratitude to the former students in Maenosono lab, Dr. Priyank Mohan, Mr. Simone Famiani, Dr. Mari Takahashi, Dr. Maninder Singh, Mr. Koichi Kitaura, Mr. Yujin Wang, Mr. Takeshi Nakada and current students Mr. Masahito Hatsukano, Ms. Pratibha Dwivedi, Mr. Shujie Fei, Mr. Kimihiro Numano, Mr. Congkang Hu and former researchers Dr. Buhe Bateer, Mrs. Chiko Shijimaya. Thank you so much for supporting my research work in lab and sharing the happy time in my life.

I would like to show my heartiest thanks for my dear friends Mr. Zhongwang Wang, Mr. Youren Wang, Dr. Buhe Bateer, Mr. Shujie Fei, Dr. Priyank Mohan, Dr. Maninder Singh for sharing the happiest time and being in difficulties with me in my life in Japan.

At last, I really want to say thanks to my family. Thank you for continuing support and endless love for me. Thank you for all the understanding of hard time in my life.

Zhou Wei

Table of Contents

Chapter 1: Introduction

1.1 Introduction to Basics of Thermoelectrics

Recently, due to the increasing energy demand and prominent environmental issue, energy diversification and multi-level efficiently utilize of energy have become important technical approaches to systematically solve the problem.[1,2] Thermoelectric (TE) technique have attracted much attention in the field of industry and academia because it act as a green energy technology. For example, the efficient multi-stage utilization of industrial waste heat, the recovery of environmental energy and the development of special power technology lead to the urgent requirements for the efficient thermal energy conversion technology.[3] Meanwhile, the development of modern industries such as electronic information and new energy vehicles put forward the urgent need for the technique, which can quickly control temperature in tiny spaces and actively thermal control high density heat flux at local area. Therefore, thermoelectric power generation have attracted unprecedented expectations due to their advantages of irreplaceable flexibility, diversity, and reliability.[4]

The Seebeck effect is the first physical effect of direct conversion of TE energy, which was found by German scientist Thomas Johann Seebeck in 1821.[5] In his experiment, two different metal wires were connected end to end to form a loop, when one of the junction is heated and the other was kept cold as shown in Figure 1.1 (a), a magnetic field generated around the loop. In 1823, Hans Christian Oersted gave the physical interpretation. This phenomenon is due to the temperature gradient creates a potential difference between the junctions of different materials lead to generate a circuit current that causes a magnetic field around the wire. Thereby, the concept of thermoelectricity is proposed. However, Seebeck was the first to found this phenomenon and it named as Seebeck effect. The potential difference can be expressed in the equation 1.1 as flowing:

$$S = \Delta V / \Delta T \tag{1.1}$$

Where S is Seebeck coefficient (μV/K), ΔV is potential difference (V), ΔT is temperature gradient (K). The principle can be explained by the illustration as shown in Figure 1.1 (b).

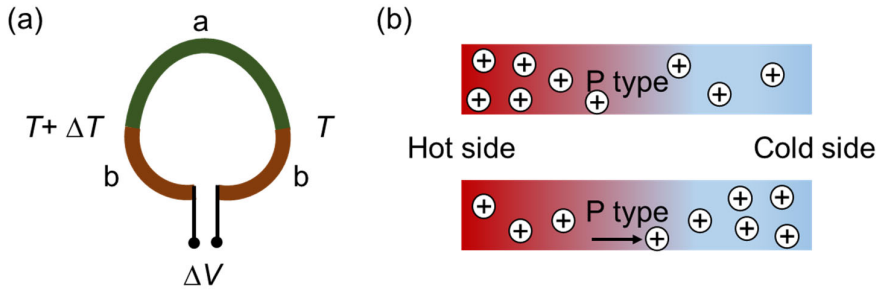

Figure 1.1. (a) Illustration of Seebeck effect, (b) Schematic diagram for principle of Seebeck effect.

As shown in Figure 1.1 (b), when a p type semiconductor kept in a uniform temperature field, the carriers are uniform distributed inside. When a temperature difference exists between the two ends, the holes in the hot side get much more energy than that of cold side that leads to more holes generated at the hot end. Thus, the hole concentration difference leads to holes diffuse to the cold end resulting in uneven distribution of internal charge concentration of materials forming a space electric field inside of the material. Meanwhile, it produces a reverse drift charge flow under the influence of the potential difference, when the charge diffusion flow caused by the thermal diffusion and the drift charge flow generated by the electric field are dynamically balanced. A stable potential difference formed at both ends of the semiconductor.

In 1834, France scientist Jean-Charles-Athanase Peltier discovered the reverse process of the Seebeck effect named Peliter effect[6] that is when an electric current flow produced in a loop connecting two different conductors, one junction became hot and another become cold. In 1855, William Thomson, also called Lord Kelvin related these two important effects by

thermodynamic theory and predicted another effect which had been proved by experiment in 1867, known as Thomson effect.[7] In 1911, Edmund Altenkirc analyzed the TE energy conversion efficiency and gave a theory to calculate it.[8] He also pointed out that a high TE conversion efficiency should improve the absolute Seebeck coefficient and electrical conductivity and meanwhile should low the thermal conductivity. Based on them, Abram Fedorovich Ioffe quantified the expression to the dimensionless of figure of-merit (ZT) as shown in the equation 1.2.

$$ZT = S^2\sigma T/\kappa \tag{1.2}$$

Wher σ is the electrical conductivity (S/m); T is the temperature (K); κ is the thermal conductivity ((W·m^{-1}·K^{-1}).

1.2. Thermoelectric Efficiency and the Figure of Merit (*ZT*)

A simplest thermoelectric generator consisting of a single thermocouple with thermoelements fabricated from n- and p-type materials as shown in Figure 1.2.

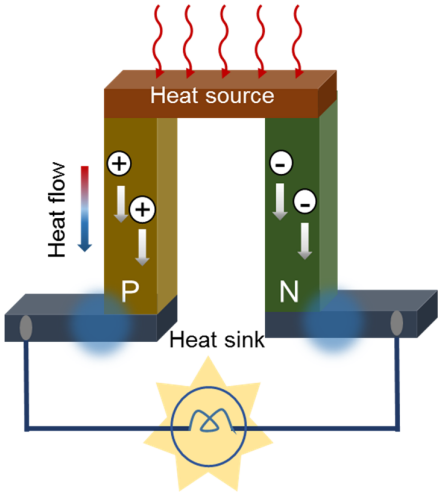

Figure 1.2. Illustration of thermoelectric generator based on Seebeck effect.

The efficiency of the generator[9] is given in the equation 1.3.

$$\eta = \frac{P}{Q_{\mathrm{h}}} \tag{1.3}$$

Where η is generator efficiency of generator, P is the energy supplied to the load, Q_{h} is the heat energy absorbed at hot junction. Assumption that the electrical conductivities, thermal conductivities, and Seecbeck coefficients of materials are constant within an arm, and that the contact resistances at the hot and cold junctions are negligible compared with the sum of the arm resistance. The maximum efficiency can be expressed as equation 1.4.

$$\eta_{\max} = \frac{T_{\mathrm{h}} - T_{\mathrm{l}}}{T_{\mathrm{h}}} \frac{\sqrt{1+ZT}-1}{\sqrt{1+ZT}+T_{\mathrm{l}}/T_{\mathrm{h}}} \tag{1.4}$$

Where T_{h}, T_{l} are the temperature of hot and cold side, respectively. T is the average temperature of hot and cold side. $(T_{\mathrm{h}}\text{-}T_{\mathrm{l}})/T_{\mathrm{h}}$ is Carnot efficiency. The maximum efficiency is thus the product of the Carnot efficiency, which is clearly less than unity. Figure 1.3 shows the relationship of maximum efficiency and the temperature difference between hot and cold side when the cold side temperature is 300K. It is known that the higher ZT value, the better generator efficiency.

.

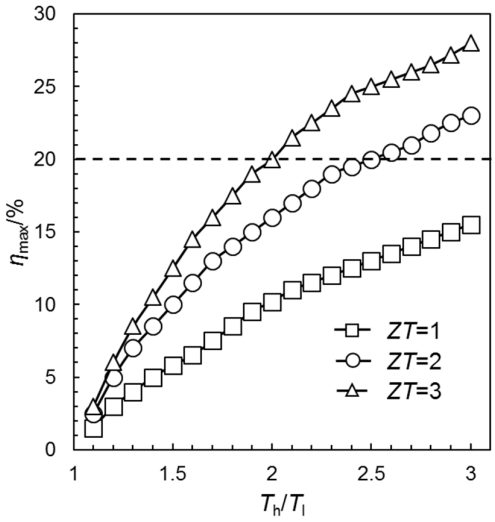

Figure 1.3. Relationship between the maximum efficiency and $T_{\mathrm{h}}/T_{\mathrm{l}}$ when T_{l} is 300K.[10]

If we want to achieve the same efficiency 25% as a traditional heat engine, the *ZT* value of material should be more than two. However, most of the materials are less than unity, which lead to the low efficiency less than traditional heat engine. Therefore, how to improve the *ZT* value of material has become the core work of TE materials.

The dimensionless of figure of merit (*ZT*) is an important parameter for judging a thermoelectric material. For a long time, researches on TE materials have focused on how to improve *ZT* value of materials. As we know, $ZT=S^2\sigma/\kappa$, a high performance TE material should have high power factor ($PF= S^2\sigma$) and low thermal conductivity (κ). However, *S*, σ and κ are interrelated to each other in a reverse manner. The Seebeck coefficient can be expressed by using Fermi-Dirac statistics.[11] Mott-Jones relation is useful for metals and highly degenerate semiconductors, which mainly applicable for simple transport models[12] is shown in the equation 1.5.

$$S = \frac{8\pi^2 K_B^2}{3eh^2} m^* T \left(\frac{\pi}{3n}\right)^{2/3} \tag{1.5}$$

Where k_B, *e*, *m**, *h* and *n* are Boltzmann constant, carrier charge, effective mass of the carrier, Planck's constant and carrier concentration, respectively.

The electrical conductivity is related to carrier concentration is given by equation 1.6.

$$\sigma = ne\mu \tag{1.6}$$

Where μ is carrier mobility. It is clearly to observe that an increase in carrier concentration decreases the Seebeck coefficient whereas the electrical conductivity increases with the increase in carrier concentration. Fundamentally, it limits the efforts of improving the power factor.

Further, the total thermal conductivity is given by equation 1.7.

$$\kappa = \kappa_e + \kappa_{lat} \tag{1.7}$$

Where κ_e and κ_{lat} are the electronic and lattice thermal conductivity, respectively. It indicates that κ_e and κ_{lat} both contribute to the total thermal conductivity. According to Weidemann-Franz law,[13-14] the electronic conductivity can be estimated in equation 1.8.

$$\kappa_e = L\sigma T \tag{1.8}$$

Where L is the Lorenz number (2.44×10^{-8} WΩK^{-2}). From the above equation, it reveals that the materials with high electrical conductivity also possess high thermal conductivity. Therefore, monotonic increase in carrier concentration leads to increase thermal conductivity and hence affects adversely on ZT value. Figure 1.4 describes the variation of Seebeck coefficient (S), electrical conductivity (σ), electronic thermal conductivity (κ_e), lattice thermal conductivity (κ_{lat}) and power factor ($S^2\sigma$) relationships of carrier concentration (n) over a wide range. It shows that the best materials for thermoelectric applications are semiconductors with optimum power factors.

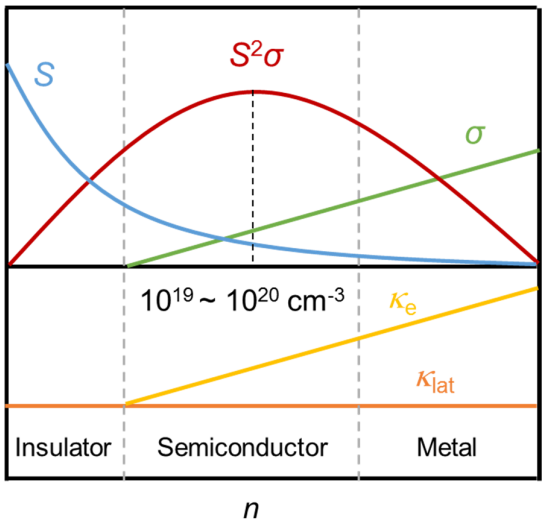

Figure 1.4. Interrelation between carrier concentration (n) and σ, S, PF, κ_e, κ_{lat}.[15]

Among them, lattice thermal conductivity is relatively independent; however, the scattering mechanisms of electrons and phonons are usually related to each other, the reduction of lattice thermal conductivity by scattering phonons often affects electrical conductivity. Therefor, three

important parameters (σ, S, κ) that determine the TE properties of a material are closely related, which is the basic reason of the difficulty in continuing improve *ZT* values of TE materials.

1.3 Approaches to Improve the Thermoelectric Efficiency

Several approaches have been introduced as modern concepts to improve the TE performance. (1) Enhance the Seebeck coefficients by electronic band structure convergence,[16-17] (2) Increase the electrical conductivity by doping effect[18-20] and (3) Reduce the lattice thermal conductivity through nanostructuring and all-scale hierarchical architecturing.[21-23] For example, design of isostructural solid solution alloys,[24-31] complex crystal structuring,[32-33] doping,[34-38] etc. Among these approaches, nanostructuring and all all-scale hierarchical architecturing are important strategies to reduce the lattice thermal conductivity, which has been proven to be very promising. Hereby, some of these approaches will be discussed briefly in the following text.

1.3.1 Isostructural Solid Solution Alloys

The solid solution alloying between two isostructural phases (e.g., A and B) results in a minimum of thermal conductivity at a certain composition $A_{1-x}B_x$, which has been proven to be a successful and classical strategy to increase *ZT* by introducing point defects.[39-40] The solid solutions feature atomic mass fluctuations in the crystal lattice (i.e., disorder), which causes strong phonon scattering and generally can lead to significant lower thermal conductivity. It has been proven in many systems such as $PbTe_{1-x}Se_x$,[41] $CuGa_{1-x}In_xTe$,[42] Mg_2Si based solid solution,[43] $CoSbS_3$ based solid solution[44] and so on. For example, compared to pure PbTe, the point defects in $PbTe_{1-x}Se_x$ scatter the phonons and result in a large decrease around 20% in the thermal conductivity at 800K and hence an enhancement in overall thermoelectric efficiency.

1.3.2 Complex Crystal Structuring

In 1996, Sales filled rare elements La and Ce into the hole of crystal structure $(Fe_xCo_{1-x})_4Sb_{12}$ which significantly reduced the lattice thermal conductivity of material.[45] This is a classic case of filling in atoms to the complex symmetry. The crystal structure with "cages" or "tunnels" that is large enough to allow atoms locate inside to rattle without destroying the favorable electronic structure. "Rattling" frequencies are low and produce phonon damping that can result in dramatic reduction of the lattice thermal conductivity.

In 1990s, Slack proposed the idea of "Phonon glass and electron crystal" (PGEC)[46] as a design concept for good TE materials. That is, an ideal TE material should achieve record low lattice thermal conductivities and meanwhile has excellent electronic performance. Some "clathrate" and "skutterudite" compounds[32] have recently emerged as a new class of materials for thermoelectric because of their quite complex crystal structures that are likely working according to the PGEC concept. Unfortunately, until now, it has not been proven that a PGEC material exists. In most cases of PGEC materials, many factors were accounted to coexist in the reduction of thermal conductivity.

1.3.3 Doping

To achieve high *ZT* values of materials. Optimization of carrier concentration is necessary, which can be done by doping foreign elements in the compounds.[47] When the energy level of a dopant is close to either valence band or conduction band or sometimes inside these bands due to heavy doping, there is a possibility of changing of density of state (DOS) around Fermi level. It was pointed out that most of the TE materials are heavily doped semiconductors with carrier concentration approximately 10^{18}-10^{20} cm^{-3}.

Kim group investigated the effect of Pb, Ag, and Cu doping on the TE transport parameters of p-type $Bi_{0.52}Sb_{1.48}Te_3$ both theoretically and experimentally.[48] They found that the concentration of majority of hole carriers could be increased by controlling doping of Pb, Ag,

and Cu in a low temperature range. In addition, a *ZT* value of 1 could be obtained over the wide temperature range of 300-400 K by optimizing the doping elements and contents. Recently, Wu et al.[27] reported that a record *ZT* reached to 2.3 at 923K, realized in 3% Na doped $(PbTe)_{1-x}(PbS)_x$ when $x = 0.2$. Duong et al.[49] reported that n-type SnSe single crystals were successfully synthesized by doping bismuth (Bi) and achieved the maximum *ZT* value of 2.2 along b axis at 733 K and with a carrier density of 2.1×10^{19} cm^{-3} at 773 K in the most highly doped sample. Doping has been proven an effective method to improve TE performance.

1.3.4 Nanostructuring and All-scale Hierarchical Architecturing

The *ZT* value of material can also be enhanced by decreasing the thermal conductivity. The complex relationship between thermoelectric parameters (S, σ, κ_e) indicate that the lattice thermal conductivity (κ_{lat}) is the only independent one on the carrier concentration. The lattice thermal conductivity (κ_{lat}) can be expressed in the equation 1.9.

$$\kappa_{\mathrm{lat}} = \frac{1}{3} C_{\mathrm{v}} v l \tag{1.9}$$

Where C_v is the heat capacity and v is the phonon velocity that are constant values; l is the phonon mean free path (MFP), so the κ_{lat} is governed by the MFP.[50] When the dimension of grain boundaries, the inclusions/defects in the material are comparable to the MFP, the phonons will be effectively scattered. Therefore, suppressing the lattice thermal conductivity by effective phonon scattering is an important method to enhance the TE performance. Acoustic phonons have a spectrum of wavelengths and MFP distribution, which carry the most of heat in a material. The including short, medium and long wavelength phonons, synergetically contributes to the total thermal conductivity.[10, 21, 51] Therefore, all length-scale structures (point defects, nano-scale precipitates and grain boundaries) corresponding to the broad spectrum of phonons should be the main design principle for decreasing the lattice thermal conductivity in TE materials.

Nanostructuring and all-scale hierarchical architectureing are effective methods to scatter most of phonons in TE materials. In general, there are two types of nanostructured TE materials. The first type consists of a single phase and it is defined by an assembly of nanosized particles or grains. The second type is a system comprising a major bulk phase containing a minor second phase embedded in the matrix. Here, the second phase is nanoscale size whereas the matrix itself need not be.

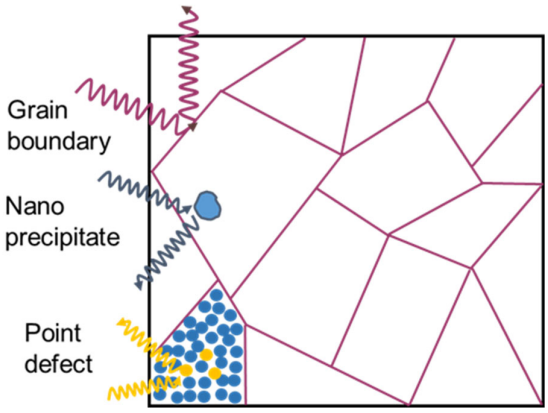

Figure 1.5. All-scale hierarchical architectures to scatter phonons.[51]

Particularly, many experiments and theoretical investigations have been done to predict a large reduction in thermal conductivity in bulk nanostructured materials with improved *ZT* values.[51-52] The all-scale hierarchical architecturing strategy was also successfully introduced and applied to various lead chalcogenides PbQ (Q = Te[53], Se[54], and S[55]). In our research group, nanostructuring and all-scale hierarchical architectureing strategies have been successfully proceed in reducing the lattice thermal conductivity, which further lead to the enhancement in the TE performance of copper sulfide based materials.[56-58]

1.4 Typical Materials for Thermoelectric Applications

Back to the TE materials. The working temperature of TE materials can be divided into three ranges: low-, middle- and high- temperature ranges varying from <400K, 400K~900K and

>900K, respectively.[32] TE materials have the most optimal TE performances in different temperatures is due to the nature of material itself. In the following text, I will introduce some typical TE materials along with their challenges for real application.

1.4.1 State-of-the-art Thermoelectric Materials and Their Challenges

Bi_2Te_3-based materials have been found in 1950s, which emerged to propose excellent TE performance near room temperature and have been widely used in commercial ways. Their *ZT* values are larger than unity. Recently, the research work shown that the superlattices and quantum dots of Bi_2Te_3 with further improvement of $ZT > 2$.[59]

PbX (X=S, Se, Te) based materials were one of the first found well-known TE materials.[60-61] In 1822, Seebeck found PbS material has high Seebeck coefficient, however, the systematically investigation on its compounds were done after the second world war. PbTe is one of the most attractive materials, the study of which throughout the history of thermoelectric.[62-64] It has optimal TE performance at middle temperature range. By using multi-scale hierarchical architecture to control phonon scattering, the *ZT* value of PbTe have achieved to 2.2.[21] In 2014, Rachel et al reported a high *ZT* value of 2 at 800K in the 2% Na doped $(PbTe)_{1-2x}(PbSe)_x(PbS)_x$ material when x=0.07.[65]

In 1960s, people found that SiGe alloy has lower thermal conductivity without significantly destroying carrier mobility resulted in an excellent TE performance compare to pristine Si and Ge. After that, SiGe alloy has been used as one of the particular TE materials for high temperature applications. Its working temperature can range from room temperature to 1300K. The highest *ZT* values of p type and n type of $Si_{80}Ge_{20}$ are 0.5 and 0.93 (1173K~1223K), respectively.[66] By using nanostructuring approach, the *ZT* value of $Si_{80}Ge_{20}$ have been raised to near 1.3.[67] SiGe alloy has been used for space missions, which converts radio-isotope heat

into electricity. As we know, Ge is expensive element, which is not suitable for practical application.

Bi_2Te_3, PbX (X=S, Se, Te) based materials have been studied for TE materials extensively. However, the use of these compounds limited by several reasons such as the used of heavy elements Te and Pb are toxicity, rare, expensive and their compounds have difficulty in processing, etc. For instance, Te is the main candidate used in the promising TE materials and its abundance in the earth's crust is only 0.001 ppm, which is even less than gold (Au) which is about 0.004 ppm.[68] The low cost-effective, lack of resources, environmental hazards of these materials are the major reasons to restrict the use of making large-scale thermoelectric generators in electrical power generation.

1.4.2 Copper Sulfide Thermoelectric Materials and Their Challenges

Many new materials have been developed, however the limitations either in the low conversion efficiency or in the cost made them are not feasible in large-scale thermoelectric energy conversion applications. Another important candidate here is copper sulfide material. It has been reported that around 34 % of the energy has been utilized from the total consumed energy from coal, petroleum, natural gas etc. and rest of the consumed energy is dissipated as waste heat. And the their temperature is under 400 ^{o}C. In this temperature range, the TE efficiency of copper sulfide is comparable to the classical material Bi_2Te_3, PbTe systems as discussed above in section 1.4.1. Moreover, Copper sulfide contain low cost, earth abundance and environmentally friendly elements. In addition, many research groups have reported promising electronic properties of these materials.

Copper sulfides are usually expressed as $Cu_{2-x}S$, where the value of x varies between 0 and 1. Depending on the x value, the stoichiometry of copper sulfide varies from Cu_2S to CuS.[69-72] To date, many kinds of phases have been identified as well as promising TE efficiencies. In 2011,

it was reported that digenite ($Cu_{1.8}S$) with a second djurleite ($Cu_{1.96}S$) phase exhibited $ZT = 0.5$ at 673 K.[73] In 2014, the relatively high ZT values are 1.4 at 1000 K for $Cu_{1.98}S$, and 1.7 at 1000 K for $Cu_{1.97}S$ which were reported by He et al.[74] Recently, Na doped $Cu_{1.8}S$ have been prepared with improved ZT of 1.1.[75] Zhao et al reported a maximum thermoelectric efficiency with ZT equal to 1.9 is observed in $Cu_{1.97}S$ bulks at 970 K.[76] Even though many promising TE efficiencies have been observed in copper sulfides. However, the TE properties are very sensitive to change in the ratio of Cu/S. Moreover, the optimum Cu/S ratio of Cu_xS are favorable for high power factors and ZT values. It has been proven that Copper sulfides are thermally unstable, the second phase may generate during measurement, meanwhile, a slight composition change also has impact on the TE efficiency.[77] Need for strict control of the composition in compounds as well as thermally unstable are big challenges for practical application.

1.4.3 Copper Tin Sulfide as Thermoelectric Materials

As another choice, many research works have been carried on alloys, which consist of copper and sulfur as main candidates, one of the most frequently studied compounds is copper tin sulfide. Cu-Sn-S system has been emerged as promising earth-abundant photovoltaic absorber materials based on the DFT calculation. [78] Among them Cu_2SnS_3, hereafter CTS, which has been intensively studied in the photovoltaic field,[79-80] and recently has attracted much attention as an outstanding p-type eco-friendly TE material due to its stability for wide temperature range.

CTS has a melting point of 1129 K and a direct band gap of 0.9-1.3 eV.[80-82] It has also been reported that the bulk form of Cu_2SnS_3 shows monoclinic,[83] tetragonal[84] and triclinic[85] structures at low temperatures (<780 ºC). The metastable zincblende (ZB) and wurtzite (WZ) phases were observed only at higher temperatures (>780 ºC). However, in the nano-scale region, ZB and WZ structures exist even at low temperatures.[86] ZB and WZ CTS structures are

considered to be derived from ZnS structure. The 2/3 and 1/3 Zn^{2+} cations in ZnS are replaced by Cu^{+} and Sn^{4+} cations in cubic and wurtzite CTS. The Cu^{+}, Sn^{4+} and sulfur occupy the same position in the CTS as they have in ZnS zincblende structure. Figure 1.6 shows the unit cells and structure relations of Cu_2SnS_3 with ZB and WZ structures.

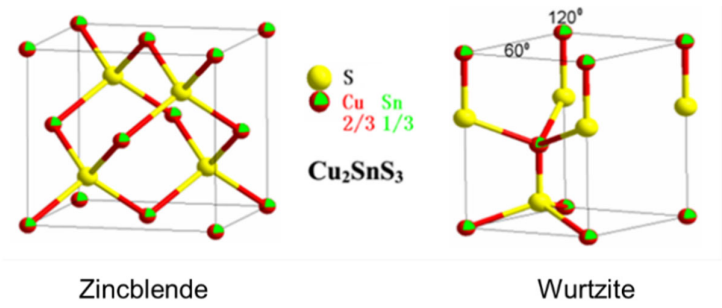

Figure 1.6. The zincblende (left) and wurtzite (right) structures of CTS material.[86]

Recently, Shen et al. have systematically studied the Zn-doped CTS as TE materials, which synthesized by direct reaction at high temperature followed by spark plasma sintering (SPS) at 773 K. As a result, $Cu_2Sn_{0.9}Zn_{0.1}S_3$ exhibited ZT = 0.58 at 723 K.[87] In-doped CTS bulk materials were prepared by the mechanical alloying (MA) combined with SPS. In that work, $Cu_2Sn_{0.9}In_{0.1}S_3$ displayed ZT = 0.56 at 773 K , which has been reported by Tan et al.[88] Zhao et al. also studied the Co-doped CTS, which synthesized by direct reaction at high temperature followed by SPS. The sample of $Cu_2Sn_{0.8}Co_{0.2}S_3$ showed ZT = 0.85 at 723 K.[89] The same group also reported a ZT of ~0.75 has been achieved in the Fe doped sample $Cu_2Sn_{0.85}Fe_{0.15}S_3$ at 723 K.[90] Xu et al. reported a relatively high ZT up to 0.56 in the $Cu_2Sn_{0.9}Ni_{0.1}S_3$ sample at 723 K.[91] Zhang et al. investigated the Mn doped CTS , a high ZT ~0.68 at 723 K was obtained.[92] Cu_2SnS_3 was also successfully synthesized by Nakamura group, they used a solid phase reaction with binary compounds and obtained high a Seebeck coefficient and a low thermal conductivity. However, the low electric conductivity results in a low ZT of less than 0.1.[93]

No report about nanostructured CTS as building block for TE materials have been studied before. In our research, in order to investigate sustainable TE materials with high efficiency; CTS was chosen as the based TE material for study, doping and nanostructuring strategies would be employed to investigate the related TE properties. Moreover, in this research Zn was the first selected element as the acceptor dopant for substituting Sn considering its similar radius (60 pm, C.N.= 4) to that of Sn^{4+} (55 pm, C.N.= 4) and Cu^{+} (60 pm, C.N.= 4) as well as its cost benefit. Even though there are other elements could be considerable choices such as Fe, Ni and Co, however, they are magnetic elements with many valence states, which might have unexpected effects on the TE properties and it is difficult to clarify the mechanism.

Until now, many groups have focused on the bulk CTS based compounds as TE materials and introduced many strategies to improve the *ZT* values. All of the samples were fabricated by solid-state reaction. Physical methods are costly due to the complex operation, complex equipment structure and vacuum is need for operation.[94] On the other hand, chemical methods are easily to operate with low cost, no use of vacuum and low wastage of material. Moreover, chemical methods can easily tune the shape, size and electronic properties of the materials during the reaction.

1.5 Chemical Methods for Synthesis of Copper Tin Sulfide Nanoparticles

The most often used chemical methods for synthesis of CTS nanoparticles (NPs) are the solvothermal/hydrothermal method, hot injection method, one pot chemical method.[95] The recent developments in CTS NPs synthesis by various chemical methods with its working mechanism and the effect of various experiment parameters will be briefly discussed in the following text.

1.5.1 Solvothermal/Hydrothermal method

Solvothermal/hydrothermal method can be described to be a closed vessel reaction system, which involves decomposition or reaction between precursors in the presence of solvent.[96] In addition, the reaction is accomplished by applied temperature and pressure. The pressure is self-generated as increased with temperature and the percentage filled in the vessel and the dissolved salts. The solvothermal process can be affected by many factors such as chemical property of solvent, composition, structure of solvent precursors, chemical properties of additives, pH, reaction temperature and time. In this synthesis scheme, water and ethanol are widely used as solvent. Ethylene glycol (EG) act as both solvent and reducing regent. In general, ethylenediamine (EDA), polyethylene glycol (PEG), dimethyl formamide (DMF) are also used as solvent. The different combination of mixed solvent can have great influence on morphology and chemical structure of NPs.[97] In hydrothermal method, the solvent used is water. In both cases, commonly used copper sources are hydrated based chloride, acetate and copper powder. Tin sources used only hydrated chloride sources and tin powder. Sulfur sources are sulfur powder, thiourea, L-cysteine, thioacetamide, thiosemicarbazide and 1-dodecanethiol (DDT). The difference in reactivity of cationic and anionic precursors results in separation of nucleus and phases. Reaction temperature has impact on nuclei formation and crystallization of particles. Reaction time plays role in tuning size, phase and morphology of particles. Many shapes and sizes such as naosphere,[98] nanorod,[99] nanoflower[100] of CTS particles have been synthesized based on them.

The reaction mechanism of CTS formation by solvothermal/hydrothermal method have been investigated.[101] Initially, Cu^{2+} ions are reduced to Cu^{+} by sulfur source to form Cu^{+}-S complexes. Meanwhile, Sn^{2+} ions are oxidized to Sn^{4+} ions by Cu^{2+} ions. These two reactions proceed simultaneously. As the temperature and pressure increases, the Cu^{+}-sulfur complex will decompose to release Cu^{+}, H_2S species produced from sulfur source as well. The produced Sn^{4+} ions then react with H_2S can form $[Sn_2S_6]^{4-}$ monomer anions, which further react with

newly formed Cu^{+} ions to form Cu_2SnS_3. The timely breaking of Cu^{+}-sulfur complex and the reaction of split Cu^{+} ions with the monomer anions is very important. Otherwise, the reaction will be not complete, and it may form impurities. Because of the drawbacks such as long processing time, low dispersibility, no control of composition and wide distribution of particle size.[102] This method is not suitable for large-scale synthesis.

1.5.2 Hot Injection Method

Hot injection reaction is carried out in a three-neck flask. It starts with a rapid injection of cold precursor into hot complex precursor solvent followed by ageing at certain temperature.[103] The sudden injection of cold precursor into hot complex precursor causes lowering of the temperature of the complex precursor leading to rapid nucleation followed by slower growth of particles. It is usually preferred for nanoparticle synthesis due to its advantage in greater controlling over size, composition and phase.

For the synthesis of CTS compounds, initially, copper and tin metal precursors are mixed in the coordinating solvent and heated at a certain temperature followed by ageing for some time (100-160 ^{o}C and 30 min). It forms copper tin complex. Further, sulfur source is rapidly injected into the hot complex solution. Then the complex is heated to temperature (220-260 ^{o}C) and is allowed to age for some time to complete the reaction and tune the size of particles.[104-106] The formation of complex is associated with color change.

Usually chloride, acetate, acetylacetonate and iodide metal precursors are used, elemental sulfur powder, thiourea, DDT are commonly used as sulfur sources. Oleylamine (OLA) and octadecene (ODE) are the commonly used solvents. Capping agents like oleic acid and trioctylphosphine oxide (TOPO) are commonly used for phase and size tuning.[105,107] Different metal precursors, sulfur source and solvents combining can affect CTS nanoparticle synthesis. Size, shape and phase tunability can be achieved using different solvents and varying metal

precursor molar concentration. Using highly reactive sulfur source, strong coordinating solvent and capping agents can produce metastable phase of CTS in this method.[86] The reaction mechanism has been studied in details.[107,108] In this method, copper sulfide nanocrystals formed first and then it transformed to CTS by Sn interdiffusion with increasing aging time. The general reaction mechanism in hot injection method can be described in Figure 1.7.

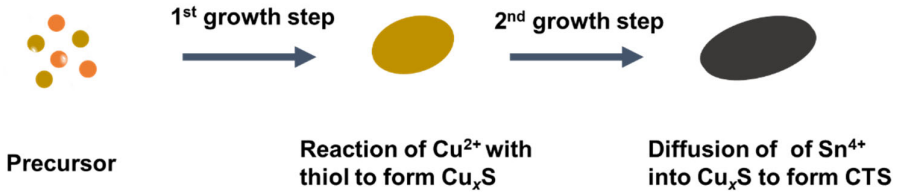

Figure 1.7. Schematic representation of the growth process for the formation of CTS NPs. [107]

1.5.3 One Pot Chemical Method

Pellet shape of material is required for TE properties measurements, hence, larger scale of nanoparticles synthesis method is preferred. One pot chemical method is an ideal option for large-scale synthesis.[109] It can be described as a reaction, which all precursor were added into the solvent at the beginning of the reaction. The mixture is heated to induce thermal decomposition of precursors followed by nucleation and growth. The general reaction mechanism is similar to the hot injection method, initially; Cu_xS seed generated and followed with Sn ions diffusion to form CTS nanoparticles. Lin et al.[110] synthesized kuramite-tetragonal CTS phase using elemental sulfur powder as sulfur source and OLA as solvent. It was found that the atomic composition did not change while the size of NPs increased from 10.7 nm to 16.4 nm with the reaction time increased from 5 to 45 min. Thus, it was concluded that the crystal structure formed at the beginning with the desired atomic composition does not change throughout the reaction. However, unfortunately, it is difficult to control the phase and size of CTS NPs simultaneously by using this method.

As we all know, the crystal structure of NPs has great influence on the final TE properties. However, the work on the studied of phase selectivity mechanism of CTS NPs in this method is still incomplete; the difficulty is due to the various reaction parameters. Many researchers have studied the phase selective mechanism and suggested that the crystal structures of the final CTS NPs were indeed related to the initial structure forms of the Cu_xS seeds.[111] Liang proposed that the initial redox conditions is the key reason for forming different phase structures. When the reaction was conducted under reducing conditions, Cu_2S (or $Cu_{31}S_{16}$) seeds were formed, leading to the formation of wurtzite CTS nanocrystals. When the conditions were less reducing, the initial CuS (or $Cu_{1.84}S$) seeds resulted in zincblende structure CTS nanocrystals.[112] Kuzuya et al. reported that the anion sources with different capabilities of providing electrons result in the various structure forms of Cu_xS seed.[113] Regulacio et al. suggested that the organic surfactant used in the synthesis that induced the different crystal phase of the Cu_xS seeds.[114] It should be noticed that the reaction temperature, time, metal precursor concentration and reactivity of precursor sources and so on also are responsible for phase formation and size tenability. It is a big challenge to identify the exact parameter.

1.6 Research Objective

The energy and environmental issue drive people to look for sustainable TE materials. Even though, many approaches have been introduced to improve the TE efficiencies of Te based, Se based materials; the toxicity and low abundance in nature still limit them for commercial use. In this environment, to investigate sustainable TE materials with high efficiency, CTS used as TE material was chosen as a model for study. Moreover, the nanostucturing, all-scale hierarchical architectureing and Zn doping strategies were employed in this research work to investigate their effect on the final TE efficiencies of CTS materials for designing the sustainable TE materials. Keep this in mind; my research work has devoted to address the

investigations in the chemically synthesized CTS based nanostructed materials as TE materials in terms of structures, compositions, sizes and TE properties, which will support the foundation information for the future practical use. Meanwhile, hot injection and one pot chemical methods will be proceeded to control over the size, shape and phases of NPs as building block for making naobulk TE materials. My research will address the following items; the details are discussed later:

(1) Fabrication of CTS NPs with different structures and Zn contents by chemical methods, which served as building blocks for TE materials.

(2) Investigation on the doping effect and nanostructuring effect of CTS based materials on the TE properties.

(3) Synthesis of CTS NPs with controllable sizes, phases and structures by chemical method, which served as building blocks for TE nanomaterials.

(4) Study on the grain size effect of CTS materials on their TE properties.

(5) Design a new approach to introduce inclusions with different structures in blended $Cu_2Sn_{1-x}Zn_xS_3$ materials by chemical method, which served as building blocks for TE materials.

(6) Investigation on the impact of sizes and structures of inclusions included in blended $Cu_2Sn_{1-x}Zn_xS_3$ materials on the final TE properties.

The general introduction of thermoelectrics, the basic information of the focused materials, the fabrication methods and the effective strategies employed to improve the TE efficiency in this research were given in chapter 1.

In Chapter 2, one pot chemical approach was employed to fabricate CTS NPs with main zincblende cubic phase and main wurtzite hexagonal phase. Moreover, main wurtzite phase CTS NPs with different Zn compositions will be synthesized, all the samples used as building

block for TE materials. DDT was used as the sulfur source and capping ligand as well in the chemical synthesis, the long chains on the surface of NPs might have effect on the electronic transport. Thus, thiourea with shorter chain and lower boiling temperature was chosen for ligand exchange that can be easily removed during the sintering process as compared to DDT. Pulse electric current sintering (PECS) technique has been proceed to make pellets for further TE measurements. The work systematically investigated the nanostructuring and Zn doping effect on the TE properties of nanostructured CTS nanobulk materials.

In Chapter 3, one pot chemical method and hot injection method were proceed to fabricate CTS particles with different sizes used as building blocks for TE materials. As we know, the grain size has impact on the lattice thermal conductivity, which related to the mean free paths of phonons. It is necessary to understand the grain size dependence of CTS material with the TE properties. By controlling the sintering conditions, naobulk materials with different grain sizes could be obtained. Therefore, the systematical study of the grain size effect on the final TE performance of CTS materials were investigated.

In Chapter 4, the objective is to further enhance the *ZT* value of CTS based materials. It was found that the nanobulk $Cu_2Sn_{0.9}Zn_{0.1}S_3$ with mixture phase (zincblende + wurtzite) exhibits low σ and κ, nanobulk $Cu_2Sn_{0.85}Zn_{0.15}S_3$ with pure zincblende phase has high σ and κ. Surprisingly, they shown almost the same *ZT* values at 673K. Keep this in mind, the chemical methods were designed to make $Cu_2Sn_{1-x}Zn_xS_3$ nanobulk materials using $Cu_2Sn_{0.85}Zn_{0.15}S_3$ as a host material and $Cu_2Sn_{0.9}Zn_{0.1}S_3$ as inclusions with different weight ratios, which could reduce thermal conductivity without dramatically destroying electronic transport. The size and structure of inclusions on the TE properties of $Cu_2Sn_{1-x}Zn_xS_3$ nanobulk were investigated.

In Chapter 5, the general conclusions and the future proposals will be given based on this dissertation work.

References

(1) Franco, A.; Shaker, M.; Kalubi, D.; Hostettler, S. A review of sustainable energy access and technologies for healthcare facilities in the Global South. *Sustainable Energy Technol. Assess*. **2017**, *22*, 92-105.

(2) Owusu, P. A.; Asumadu-Sarkodie, S.; Ameyo, P.; Dubey, S. A review of renewable energy sources, sustainability issues and climate change mitigation. *Cogent Eng*. **2016**, *3*, 1167990.

(3) DiSalvo, F. J. Thermoelectric cooling and power generation. *Science*. **1999**, *285*, 703-706.

(4) LeBlanc, S. Thermoelectric Generators: Linking Material Properties and Systems Engineering for Waste Heat Recovery Applications. *Sustain. Mater. Technol.* **2014**, *1*, 26-35.

(5) Seebeck, J. Magnetische polarisation der metalle und erze durch temperature-differenz *abh. Akad. Wiss. Berlin*. **1822**, 289-346.

(6) Peliter, J. A. C. Nouvelles expériemence sur la caloricite descourants électriques. *Ann. Chim. Phys.* **1834**, *56*, 371-386.

(7) Thomson, W. On a mechanical theory of thermos-electric currents. *Proc. R. Soc. Edinburgh.* **1851**, 91-98.

(8) Altenkrich, E. Elektrothermische kalteerzeugung. *Physik. Zeitschr.* **1911**, *12*, 920.

(9) Rowe, D. M. *Thermoelectrics Handbook: Macro to Nano* (pp. 1-4); CRC/Taylor & Francis: Boca Raton, **2006**.

(10) Zhang, X.; Zhao, L-D. Thermoelectric materials: Energy conversion between heat and electricity. *J. Materiomics*. **2015**, *1*, 92-105.

(11) Shakouri. A. Recent Developments in Semiconductor Thermoelectric Physics and Materials. *Annu. Rev. Mater. Res.* **2011**, *41*, 399-431.

(12) Hicks, L. D.; Dresselhaus, M. S. Effect of quantum-well structures on the thermoelectric figure of merit. *Phys. Rev. B*. **1993**, *47*, 12727-12731.

(13) William, J.; Norman, H. M. *Theoretical Solid State Physics*; Courier Dover Publications, **1985**.

(14) Franz, R.; Wiedemann, G. Ueber die Wärme-Leitungsfähigkeit der Metalle. *Ann. Phys. Lpz.* **1853**, *165*, 497-531.

(15) Masood, K. B.; Kumar, P.; Singh, R. A.; Singh, J. Odyssey of Thermoelectric Materials: Foundation of the Complex Structure. *J. Phys. Commun.* **2018**, *2*, 062001.

(16) Pei, Y.-Z; Shi X.-Y; Lalonde A, W, H; Cheng, L.-D; Snyder, J. G. Convergence of electronic bands for high performance bulk thermoelectrics. *Nature*. **2011**, *473*, 66.

(17) Liu, W; Tan, X.-J, Yin, K; Liu, H.-J; Tang, X.-F; Shi, J; Zhang, Q.-J; Uher, C. et al. Convergence of electronic bands as a means of enhancing thermoelectric performance of n-type $Mg_2Si_{1-x}Sn_x$ solid solutions. *Phys. Rev. Lett*. **2012**, *108*, 166601.

(18) Szczech, J.R.; Higgins, J. M.; Jin, S. Enhancement of the thermoelectric properties in nanoscale and nanostructured materials. *J. Mater. Chem*. **2011**, *21*, 4037-4055.

(19) Heremans, J. P.; Jovovic, V.; Toberer, E. S.; Saramat, A.; Kurosaki, K.; A. Charoenphakdee, A.; Yamanaka, S.; Snyder, G. J. Enhancement of thermoelectric efficiency in PbTe by distortion of the electronic density of states. *Science.* **2008**, *321*, 554-557.

(20) Liu, M.-L; Chen, I-W; Huang, F.-Q; Chen, L.-D. Improved thermoelectric properties of Cu-doped quaternary chalcogenides of $Cu_2CdSnSe_4$. *Adv. Mater*. **2009**, *21*, 3808-3812.

(21) Biswas, K.; He, J.; Blum, I. D.; Wu, C.-I.; Hogan, T. P.; Seidman, D. N.; Dravid, V. P.; Kanatzidis, M. G. High-Performance Bulk Thermoelectrics with All-Scale Hierarchical Architectures. *Nature.* **2012**, *489*, 414-418.

(22) Mao, J.; Liu, Z.; Ren, Z. Size effect in thermoelectric materials. *npj Quantum Mater.* **2016**, *1*, 16028.

(23) Minnich, A. J.; Dresselhaus, M. S.; Ren, Z. F.; Chen, G. Bulk nanostructured thermoelectric materials: current research and future prospects. *Energy Environ. Sci.* **2009**, *2*, 466.

(24) Kaur, P.; Bera, C. Effect of alloying on thermal conductivity and thermoelectric properties of CoAsS and CoSbS. *Phys. Chem. Chem. Phys.* **2017**, *19*, 24928-24933.

(25) Fan, Z.; Wang, H.; Wu, Y.; Liu, X. J.; Lu. Z. P. Thermoelectric high-entropy alloys with low lattice thermal conductivity. *RSC Adv.* **2016**, *6*, 52164-52170.

(26) Körmann, F.; Ikeda, Y.; B. Grabowski, B.; Sluiter, M. H. F. Phonon broadening in high entropy alloys. *npj Comp. Mater.* **2017**, *3*, 36.

(27) Wu, D.; Zhao, L.-D.; Tong, X.; Li, W.; Wu, L.; Tan, Q.; Pei, Y.; Huang, L.; Li, J.-F.; Zhu, Y.; Kanatzidis, M. G.; He, J. Superior thermoelectric performance in PbTe-PbS pseudo-binary: extremely low thermal conductivity and modulated carrier concentration. *Energy Environ. Sci.* **2015**, *8*, 2056-2068.

(28) Androulakis, J.; Todorov, I.; He, J.; Chung, D.-Y.; Dravid, V.; Kanatzidis, M. Thermoelectrics from Abundant Chemical Elements: High-Performance Nanostructured PbSe-PbS. *J. Am. Chem. Soc.* **2011**, *133*, 10920-10927.

(29) Wu, C.-F.; Wei, T.-R.; Li, J.-F. Electrical and thermal transport properties of $Pb_{1-x}Sn_xSe$ solid solution thermoelectric materials. *Phys. Chem. Chem. Phys.* **2015**, *17*, 13006-13012.

(30) Yamini, S. A.; Mitchell, D. R. G.; Gibbs, Z. M.; Santos, R.; Patterson, V.; Li, S.; Pei, Y. Z.; Dou, S. X.; Snyder, G. J. Heterogeneous Distribution of Sodium for High Thermoelectric Performance of p-type Multiphase Lead-Chalcogenides. *Adv. Energy Mater.* **2015**, *5*, 1501047.

(31) Zhang, Q.; Chere, E. K.; Sun, J.; Cao, F.; Dahal, K.; Chen, S.; Chen, G.; Ren, Z.-F. Studies on Thermoelectric Properties of n-type Polycrystalline $SnSe_{1-x}S_x$ by Iodine Doping. *Adv. Energy Mater.* **2015**, *5*, 1500360.

(32) Snyder, G. J.; Toberer, E. S. Complex thermoelectric materials. *Nat. Mater.* **2008**, *7*, 105-114.

(33) Brown, S. R.; Kauzlarich, S. M.; Gascoin, F.; Snyder, G. J.; $Yb_{14}MnSb_{11}$: New High Efficiency Thermoelectric Material for Power Generation. *Chem. Mater.* **2006**, *18*, 1873-1877.

(34) He, J.-Q.; Zhao, L.-D.; Zheng, J.-C.; Doak, J. W.; Wu, H.-J.; Wang, H.-Q.; Lee, Y.; Wolverton, C.; Kanatzidis, M. G.; Dravid, V. P. Role of sodium doping in lead chalcogenide thermoelectrics. *J. Am. Chem. Soc.* **2013**, *135*(12), 4624-4627.

(35) Zhang, Q.-Y.; Wang, H.; Liu, W.-S.; Yu, B.; Zhang, Q.; Tian, Z.-T.; Ni, G.; Lee, S.; Esfarjani, K.; Chen, G.; Ren, Z.-F. Enhancement of thermoelectric figure-of-merit by resonant states of aluminum doping in lead selenide. *Energy Environ. Sci.* **2012**, *5*, 5246-5251.

(36) Girard, S. N.; He, J.-Q.; Zhou, X.-Y.; Shoemaker, D.; Jaworski, C. M.; Uher, C.; Dravid, V. P.; Heremans, J. P. and Kanatzidis, M. G. High performance Na-doped PbTe-PbS thermoelectric materials: Electronic density of sates modification and shape-controlled nanostructures. *J. Am. Chem. Soc.* **2011**, *133* (41), 16588-16597.

(37) Liu, W.; Zhang, Q.; Tang, X.-F.; Li, H.; Sharp, J. Thermoelectric properties of Sb-doped $Mg_2Si_{0.3}Sn_{0.7}$. *J. Electron. Mater.* **2011**, *40*(5), 1062-1066.

(38) Liu, W.-S.; Kim, H. S.; Chen, S. Jie, Q.; Lv, B.; Yao, M.-L.; Ren, Z,-S.; Opeil, C.P.; Wilson, S,; Chu, C.-W. and Ren, Z.-F. n-type thermoelectric material $Mg_2Sn_{0.75}Ge_{0.25}$ for high power generation. *PNAS*. **2015**, *112*(11), 3269-3274.

(39) Kanatzidis, M. G. Nanostructured Thermoelectrics: The New Paradigm? *Chem. Mater*. **2010**, *22*, 648-659.

(40) Rowe, D. M. *Thermoelectrics Handbook: Macro To Nano*; CRC/Taylor & Francis: Boca Raton, **2006**.

(41) Wang, H.; Lalonde, A. Pei, Y. Z.; Snyder, G. J. The criteria for beneficial disorder in thermoelectric solid solutions. *Adv. Funct. Mater*. **2013**, *23*, 1586-1596.

(42) Qin, Y.-T.; Qiu, P.-F.; Liu, R.-H.; Li, Y.-L.; Hao, F.; Zhang, T.-S.; Ren, D.-D.; Shi, X.; Chen, L.-D. Optimized thermoelectric properties in pseudocubic diamond-like $CuGaTe_2$ compounds. *J. Mater. Chem. A*. **2016**, *4*, 1277-1289.

(43) Bashir, M. B. A.; Said M. F. M.; Sabri, M. F. M.; Shnawah, D. A.; Elsheikh, M. H. Recent advances on $Mg_2Si_{1-x}Sn_x$ materials for thermoelectric generation. *Renew. Sustain. Energy Rev.* **2014**, *37*, 569-584.

(44) Meisner G. P.; Morelli D. T.; Hu, S.; Yang, J.; Uher, C. Structure and lattice thermal coductivity of fabricationally filled skutterudites: Solid solutitions of fully filled and unfilled members. *Phys. Rev. Lett.* **1998,** *80*, 3551-3554.

(45) Sales B. C.; Mandrus, D. Williams, R. K. Filled skutterudite antimonides: A new class of thermoelectric materials. *Science*. **1996**, *272*(266), 1325.

(46) Rowe D. M.; *CRC handbook of Thermoelectrics*; Boca Raton: CRC Press, **1995**.

(47) Dehkordi, A. M.; Zebarjadi, M.; He, J.; Tritt, T. M. Thermoelectric power factor: Enhancement mechanisms and strategies for higher performance thermoelectric materials. *Mater. Sci. Eng. R*. **2015**, *97*, 1-22.

(48) Kim, K.; Kim, G.; Kim, S.; Lee, K. H.; Lee, W. Clarification of electronic and thermal transport properties of Pb-, Ag-, and Cu-doped p-type $Bi_{0.52}Sb_{1.48}Te_3$. *J. Alloys Compd*. **2019**, *772*, 593-602.

(49) Duong, A. T.; Nguyen, V. Q.; Duvjir, G.; Duong, V. T.; Kwon, S.; Song, J. Y.; Lee, J. K.; Lee, J. E.; Park, S.-D.; Min, T.; Lee, J.; Kim, J.; Cho, S. Achieving ZT = 2.2 with Bi-doped n-type SnSe single crystals. *Nat. Commun*. **2016**, *7*, 13713.

(50) Slack, G. A. The Thermal Conductivity of Nonmetallic Crystals. *Solid State Phys.* **1979,** *34*, 1-71.

(51) Zhao, L.-D.; Dravid, V. P. and Kanatzidis, M. G. The panoscopic approach to high performance thermoelectrics. *Energy Environ. Sci.* **2014**, *7*, 25.

(52) Hicks, L. D.; Dresselhaus, M. S. Thermoelectric figure of merit of a one-dimensional conductor. *Phys. Rev. B*. **1993**, *47*, 16631-16634.

(53) Ahn, K.; Han, M. K.; He, J.-Q.; Androulakis, J.; Ballikaya, S.; Uher, C.; Dravid, V. P.; Kanatzidis, M. G. Exploring resonance levels and nanostructuring in the PbTe-CdTe system and enhancement of the thermoelectric figure of merit. *J. Am. Chem. Soc.* **2010**, *132*, 5227-5235.

(54) Lee, Y.; Lo, S. H.; Androulakis, J.; Wu, C.-I.; Zhao, L.-D.; Chung, D.-Y.; Hogan, T. P.; Dravid, V. P.; Kanatzidis, M. G. High-performance tellurium-free thermoelectrics: All-scale hierarchical structuring of p-type PbSe-MSe systems (M = Ca, Sr, Ba). *J. Am. Chem. Soc.* **2013**, *135*, 5152-5160.

(55) Zhao, L.-D.; He, J.-Q.; Wu, C.-I.; Hogan, T. P.; Zhou, X.-Y.; Uher, C.; Dravid, V. P.; Kanatzidis, M. G. Thermoelectrics with Earth Abundant Elements: High Performance p-type PbS Nanostructured with SrS and CaS. *J. Am. Chem. Soc.* **2012**, *134*, 16327-16336.

(56) Zhou, W.; Shijimaya, C.; Takahashi, M.; Miyata, M.; Mott, D.; Koyano, M.; Ohta, M.; Akatsuka, T.; Ono, H.; Maenosono, S. Sustainable Thermoelectric Materials Fabricated by using $Cu_2Sn_{1-x}Zn_xS_3$ Nanoparticles as Building Blocks. *Appl. Phys. Lett*. **2017**, *111*, 263105.

(57) Zhou, W.; Dwivedi, P.; Shijimaya, C.; Ito, M.; Higashimine, K.; Nakada, T.; Takahashi, M.; Mott, D.; Miyata, M.; Ohta, M.; Miwa, H.; Akatsuka, T.; Maenosono, S. Enhancement of the Thermoelectric Figure of Merit in Blended $Cu_2Sn_{1-x}Zn_xS_3$ Nanobulk Materials. *ACS Appl. Nano Mater.* **2018**, *1*, 4819.

(58) Singh, M.; Dwivedi, P.; Mott, D.; Higashimine, K.; Ohta, M.; Miwa, H.; Akatsuka, T.; and Maenosono, S. Colloid Chemical Approach for Fabricating Cu-Fe-S Nanobulk Thermoelectric Materials by Blending Cu_2S and FeS Nanoparticles as Building Blocks. *Ind. Eng. Chem. Res.* **2019**, *58*, 3688.

(59) Poudel, B.; Hao, Q.; Ma, Y.; Lan, Y.; Minnich, A.; Yu, B.; Yan, X.; Wang, D.; Muto, A.; Vashaee, D.; Chen, X.; Liu, J.; Dresselhaus, M. S.; Chen, G.; Ren, Z. High-thermoelectric performance of nanostructured bismuth antimony telluride bulk alloys. *Science*. **2008**, *320*, 634-638.

(60) Zhao, L.-D.; Lo, S. H.; He, J.-Q.; Li, H.; Biswas, K.; Androulakis, J.; Wu, C.-I.; Hogan, T. P.;Chung, D.-Y.; Dravid, V. P.; Kanatzidis, M. G. High performance thermoelectrics from earth-abundant materials: enhanced figure of merit in PbS by second phase nanostructures. *J. Am. Chem. Soc.* **2011**, *133*, 20476-20487.

(61) LaLonde, A. D.; Pei, Y.; Wang, H.; Snyder, G. J. Lead telluride alloy thermoelectrics. *Mater. Today*. **2011**, *14*, 526-532.

(62) Allgaier, R. S. Houston, B. B. Hall coefficient behavior and the second valence band in lead telluride. *J. Appl. Phys.* **1966**, *37*, 302-309.

(63) Allgaier, R. S. Valence bands in lead telluride. *J. Appl. Phys.* **1961**, *32*, 2185-2189.

(64) Allgaier, R. S.; Scanlon, W. W. Mobility of electrons and holes in PbS, PbSe and PbTe between room temperature and 4.2K. *Phys. Rev.* **1958**, *111*, 1029-1037.

(65) Korkosz, R. J.; Chasapis, T. C.; Lo, S. H.; Doak, J. W.; Kim, Y. J.; Wu, C.-I.; Euripidis Hatzikraniotis, E.; Hogan, T. P.; Seidman, D. N.; Wolverton, C.; Dravid, V. P.

and Kanatzidis, M. G. High *ZT* in p-type $(PbTe)_{(1-2x)}$ $(PbSe)_{(x)}$ $(PbS)_{(x)}$ thermoelectric materials. *J. Am. Chem. Soc.* **2014**, *136* (8), 3225-3237.

(66) Slack, G. A.; Hussain, M. A. The maximum possible conversion efficiency of silicon-germanium thermoelectric generators. *J. Appl. Phys.* **1991**, *70*, 2694-2718.

(67) Joshi, G.; Lee, H.; Lan, Y. H.; Wang, X. W.; Zhu, G.-H.; Wang, D.-Z.; Gould, R. W.; Cuff, D. C.; Tang, M. Y.; Dresselhaus, M. S.; Chen, G. and Ren, Z.-F. Enhanced thermoelectric figure-of-merit in nanostructured p-type silicon-germanium bulk alloys. *Nano Lett*. **2008**, *8*, 4670-4674.

(68) Liu, W.; Yan, X.; Chen, G.; Ren, Z.-F. Recent advances in thermoelectric nanocomposites. *Nano Energy*. **2012**, *1*, 42-56.

(69) Zhao, Y.; Pan, H.; Lou, Y.; Qiu, X.; Zhu, J.; Burda, C. Plasmonic Cu(2-x)S nanocrystals: optical and structural properties of copper-deficient copper(I) sulfides. *J. Am. Chem. Soc.* **2009**, *131*, 4253-4261.

(70) Rabinal, M. H. K.; Gunnagol, R. M.; Hodlur, R. M. Recent Developments in the Green Syntheses of Chalcogenide Based Semi-conductor Nanoparticles. *Current Nanomaterials.* **2016**, *1*, 12-60.

(71) Li, N.; Zhang, X.; Chen, S.; Yang, W.; Kang, H.; Tan, W. One-pot self-assembly of flower-like Cu_2S structures with near-infrared photoluminescent properties. *CrystEngComm.* **2011**, *13*, 6549.

(72) Sun, S.-D.; Li, P.-G.; Liang, S.-H. and Yang, Z.-M. Diversified copper sulfide ($Cu_{2-x}S$) micro-/nanostructures: a comprehensive review on synthesis, modifications and applications. *Nanoscale*. **2017**, *9*, 11357-11404.

(73) Ge, Z.-H.; Zhang, B.-P.; Chen, Y.-X.; Yu, Z.-X.; Liu, Y.; Li, J.-F. Synthesis and transport property of $Cu_{1.8}S$ as a promising thermoelectric compound. *Chem. Commun.* **2011**, *47*, 12697.

(74) He, Y.; Day, T.; Zhang, T.; Liu, H.; Shi, X.; Chen, L.; Snyder, G. J. High thermoelectric performance in non-toxic earth-abundant copper sulfide. *Adv. Mater.* **2014**, *26*, 3974-3978.

(75) Ge, Z.-H.; Liu, X.; Feng, D.; Lin, J.; He, J. High-Performance Thermoelectricity in Nanostructured Earth-Abundant Copper Sulfides Bulk Materials. *Adv. Energy Mater.* **2016**, *6*, 1600607.

(76) Zhao, L.; Wang, X.; Fei, F. Y.; Wang, J.; Cheng, Z.; Dou, S.; Wang, J.; Snyder, G. J. High thermoelectric and mechanical performance in highly dense $Cu_{2-x}S$ bulks prepared by a melt-solidification technique. *J. Mater. Chem. A*. **2015**, *3*, 9432-9437.

(77) Mansour, B. A.; Soud, A. M. A. E.; Tahoon, K. H. Evaluation of Some Physical Quantities in the Two-Phase Region in Copper Sulphides. *Phys. Status Solidi A.* **1992**, *132*, 59-65.

(78) Guan, P.-W.; Shang, S.-L.; Lindwall, G.; Anderson, T.; Liu, Z.-K. Phase stability of the Cu-Sn-S system and optimal growth conditions for earth-abundant Cu_2SnS_3 solar materials. *Sol. Energy*. **2017**, *155*, 745-757.

(79) Umehara, M.; Takeda, Y.; Tajima, S.; Motohiro, T.; Sakai, T. and Maekawa, R. Improvement of red light response of $Cu_2Sn_{1-x}Ge_xS_3$ solar cells by optimization of CdS buffer layers. *J. Appl. Phys.* **2015**, *118*, 154502.

(80) Ghorpade, U. V.; Suryawanshi, M.P.; Shin, S. W.; Kim, I.; Ahn, S. K.; Yun, J. H.; Jeong, C.; Kolekar, S. S. and Kim, J. H. Colloidal Wurtzite Cu_2SnS_3 (CTS) Nanocrystals and Their Applications in Solar Cells. *Chem. Mater*. **2016**, *28*, 3308-3317.

(81) Fiechter, S.; Martinez, M.; Schmidt, G.; Henrion, W.; Tomm, Y. Phase relations and optical properties of semiconducting ternary sulfides in the system Cu-Sn-S. *J. Phys. Chem. Solids*. **2003**, *64*, 1859-1862.

(82) Su, Z.-G.; Sun, K.-W.; Han, Z.-L.; Liu, F.-Y.; Lai, Y.-Q.; Li, J. and Liu, Y. X. Fabrication of ternary Cu-Sn-S sulfides by a modified successive ionic layer adsorption and reaction (SILAR) method. *J. Mater. Chem.* **2012**, *22*, 16346.

(83) Onoda, M.; Chen, X.-A.; Sato, A.; Wada, H. Crystal structure and twinning of monoclinic Cu_2SnS_3. *Mater. Res. Bull.* **2000**, *35*(9), 1563-1570.

(84) Dias, S.; Murali, B.; Krupanidhi, S. B. Solution processible Cu_2SnS_3 thin films for cost effective photovoltaics: Characterization. *Mater. Chem. Phys.* **2015**, *167*, 309-314.

(85) Han, J.; Zhou, Y.; Tian, Y.; Huang, Z.; Wang, X.; Zhong, J.; Xia, Z.; Yang, B.; Song, H.; Tang, J. Hydrazine processed Cu_2SnS_3 thin film and their application for photovoltaic devices. *Front. Optoelectron*. **2014**, *7*(1), 37-45.

(86) Liu, Q.-G.; Zhao, Z.-C.; Lin, Y.-L.; Guo, P.; Li, S.-J.; Pan, D.-C.; Ji, X.-L. Alloyed $(ZnS)_x(Cu_2SnS_3)_{1-x}$ and $(CuInS_2)_x(Cu_2SnS_3)_{1-x}$ Nanocrystals with Arbitrary Composition and Broad Tunable Band Gaps. *Chem. Commun.* **2011**, *47*, 964-966.

(87) Shen, Y.; Li, C.; Huang, R.; Tian, R.; Ye, Y.; Pan, L.; Koumoto, K.; Zhang, R.; Wan, C. and Wang, Y. Eco-friendly *p*-type Cu_2SnS_3 thermoelectric material: crystal structure and transport properties. *Sci. Rep.* **2016**, ***6***, 32501.

(88) Tan, Q.; Sun, W.; Li, Z. and Li, J.-F. Enhanced thermoelectric properties of earth-abundant Cu_2SnS_3 via In doping effect. *J. Alloys Compd*. **2016**, *672*, 558.

(89) Zhao, H.; Xu, X.; Li, C.; Zhang, R.; Huang, R.; Lv, Y.; Li, D.; Hu, X.; Pan, L. and Wang, Y. Cobalt-doping in Cu_2SnS_3: enhanced thermoelectric performance by synergy of phase transition and band structure modification. *J. Mater. Chem. A.* **2017**, *5*, 23267.

(90) Zhao, L.; Pan, L.; Hu, X. H.; Lu, C. H. and Wang, Y. Magnetic iron doping in Cu_2SnS_3 ceramics for enhanced thermoelectric transport properties. *J. Appl. Phys.* **2019**, *125*, 095107.

(91) Xu, X.-X.; Zhao, H.-W.; Hu, X.-H.; Pan, L.; Chen, C. C.; Li, D.X.; Wang. Y. Synergistic role of Ni-doping in electrical and phonon transport properties of $Cu_2Sn_{1-x}Ni_xS_3$. *J. Alloys Compd*. **2017**, *728*, 701-708.

(92) Zhang, Z.; Zhao, H.-W.; Wang. Y.-F.; Hu, X.-H.; Lyu, Y.; Chen, C. C.; Pan, L.; Lu, C.-H. Role of crystal transformation on the enhanced thermoelectric performance in Mn-doped Cu_2SnS_3. *J. Alloys Compd*. **2019**, *780*, 618-625.

(93) Nakamura, S.; Funabiki, H. and Shiga, S. Electrical conductivity improved Cu_2SnS_3 thermoelectrics. *Phys. Status Solidi C*. **2017**, *14*, 1600172.

(94) Li, Y.; Zhang, T.; Qin, Y.; Day, T.; Snyder, G. J.; Shi, X.; Chen, L. Thermoelectric Transport Properties of Diamond-Like $Cu_{1-x}Fe_{1+x}S_2$ Tetrahedral Compounds. *J. Appl. Phys.* **2014**, *116*, 203705.

(95) Lokhande, A.C.; Gurav, K.V.; Jo, E.; Lokhande, C.D.; Kim, J. H. Chemical synthesis of Cu_2SnS_3 (CTS) nanoparticles: A status review. *J. Alloys Compd*. **2016**, *656*, 295-310.

(96) Demazeau, G. Review. Solvothermal processes: Definition, Key Factors Governing the Involved Chemical Reactions and New Trends. *Z. Naturforsch*. **2010**, *65*b, 999-1006.

(97) Bahramzadeh, S.; Abdizadeh, H.; Golobostanfard, M. R. Controlling the morphology and properties of solvothermal synthesized Cu_2ZnSnS_4 nanoparticles by solvent type. *J. Alloys Compd.* **2015**, *642*, 124-130.

(98) Chen, X.; Wang, X.; An, C.; Liu, J.; Qian, Y.; Preparation and characterization of ternary Cu-Sn-E (E=S,Se) semiconductor nanocrystallites via a solvothermal element reaction route. *J. Cryst. Growth*. **2003**, *256*, 368-376.

(99) Xiong, Y.; Xie, Y.; Du, G.; Su, H. From 2D framework to quasi- 1d nanomaterial: preparation, characterization, and formation mechanism of Cu_3SnS_4 nanorods. *Inorg. Chem.* **2002**, *41*, 2953-2959.

(100) Chen, Q.; Ma, D. Preparation of nanostructured Cu_2SnS_3 photocatalyst by solvothermal method. *Int. J. Photoenergy*. **2013**, *2013*, 5.

(101) Wu, H.; Liu, D.; Zang, H.; Wei, C.; Zeng, B.; Shi, J.; Yang, S. Solvothermal synthesis and optical limiting properties of carbon nanotube-based hybrids containing ternary chalcogenides. *Carbon*. **2012**, *50*, 4847-4855.

(102) Ghorpade, U.; Suryawanshi, M.; Shin, S.W.; Gurav, K.; Patil, P.; Pawar, S.; Hong, C.W.; Kim, J.H.; Kolekar, S. Towards environmentally benign approaches for the synthesis of CZTSSe nanocrystals by a hot injection method: a status review. *Chem. Commun.* **2014**, *50*, 11258-11273.

(103) Talapin, D.V.; Rogach, A.L.; Haase, M.; Weller, H.Evolution of an ensemble of nanoparticles in a colloidal solution: theoretical study. *J. Phys. Chem. B.* **2001**, *105*, 12278-12285.

(104) Okano, S.; Takeshita, S.; Isobe, T.; Formation of Cu_2SnS_3 nanoparticles by sequential injection of tin and sulfur oleylamine solutions into $Cu_{1.8}S$ nanoparticle dispersion. *Mater. Lett.* **2015**, *145*, 79-82.

(105) Liu, X.; Wang, X.; Swihart, M.T. Composition-dependent crystal phase, optical properties, and self-assembly of Cu-Sn-S colloidal nanocrystals. *Chem. Mater.* **2015**, *27*, 1342-1348.

(106) Chang, J.; Waclawik, E.R. Controlled synthesis of $CuInS_2$, Cu_2SnS_3 and Cu_2ZnSnS_4 nano-structures: insight into the universal phase selectivity mechanism. *Chem. Eng. Commun.* **2013**, *15*, 5612-5619.

(107) Kruszynska, M.; Parisia, J.; Kolny-Olesiaka, J. Synthesis and shape control of copper tin sulphide nanocrystals and formation of gold-copper tin sulphide hybrid nanostructures. *Z. Naturforsch.* **2014**, *69*a, 446-450.

(108) Yi, L.; Wang, D.; Gao, M. Synthesis of Cu_3SnS_4 nanocrystals and nanosheets by using $Cu_{31}S_{16}$ as seeds. *Chem. Eng. Commun.* **2012**, *14*, 401-404.

(109) Liang, Q.; Han, L.; Deng, X.; Yao, C.; Meng, J.; Liu, X.; Meng, J. Compositionally tunable $Cu_2Sn(S_xSe_{1-x})_3$ nanocrystals: facile direct solution-phase synthesis, characterization, and scalable procedure. *CrystEngComm*. **2014**, *16*, 4001-4007.

(110) Lin, X.; Steigert, A.; Steiner, M. C. L.; Ennaoui, A. One step solution based synthesis and characterization ok kuramtie Cu_3SnS_4 nanocrystals, *RSC Adv*. **2012**, *2*, 9798-9800.

(111) Tan, J. M. R.; Lee, Y. H.; Pedireddy, S.; Baikie, T.; Ling, X. Y. and Wong, L. H. Understanding the Synthetic Pathway of a Single-Phase Quarternary Semiconductor Using Surface-Enhanced Raman Scattering: A Case of Wurtzite Cu_2ZnSnS_4 Nanoparticles. *J. Am. Chem. Soc.* **2014**, *136*, 6684-6692.

(112) Liang, Q. Phase-Controlled Synthesis of Cu_2SnS_3 Nanocrystals: The Effect of Redox Conditions on the Initial Binary $Cu_{2-x}S$ Nucleation. *Eur. J. Inorg. Chem*. **2016**, *2016*, 3634.

(113) Kuzuya, T.; Hamanaka, Y.; Itoh, K.; Sumiyama, K.; Fukunaka, Y.; Hirai, S. Phase control and its mechanism of $CuInS_2$ nanoparticles. *J. Colloid Interface Sci.* **2012**, *388*, 137-143.

(114) Regulacio, M. D.; Ye, C.; Lim, S. H.; Bosman, M.; Ye, E.; Chen, S.-Y.; Xu, Q.-H. and Han, M.-Y. Colloidal Nanocrystals of Wurtzite-Type Cu_2ZnSnS_4: Facile Noninjection Synthesis and Formation Mechanism. *Chem. Eur. J.* **2012**, *18*, 3127-3131.

Chapter 2: Nanostructured Thermoelectric Materials Fabricated using Cu_2SnS_3 based Nanoparticles as Building Blocks

2.1 Introduction

Copper sulfide thermoelectric materials have recently attracted much attention due to their relatively high *ZT* value along with the earth-abundant nature and low toxicity of their constituent elements. In 2011, it was reported that digenite ($Cu_{1.8}S$) with a second djurleite ($Cu_{1.96}S$) phase exhibited *ZT* = 0.5 at 673 K.[1] In 2013, Suekuni and coworkers found that $Cu_{10.5}Ni_{1.5}Sb_4S_{13}$ tetrahedrite exhibited *ZT* = 0.7 at 665 K.[2] Shortly thereafter, Suekuni and coworkers reported that $Cu_{26}V_2Ge_6S_{32}$ colusite had a *ZT* value of 0.73 at 663 K.[3] At nearly the same time, several copper sulfide thermoelectric materials with a *ZT* value exceeding 1, such as $Cu_{11}MnSb_4S_{13}$ tetrahedrite (*ZT* =1.13 at 575 K),[4] $Cu_{10.5}Ni_{1.0}Zn_{0.5}Sb_4S_{13}$ tetrahedrite (*ZT* = 1.03 at 575 K),[5] and $Cu_{26}Ta_2Sn_{5.5}S_{32}$ colusite (*ZT* ~ 1 at 670 K),[6] had been reported from different groups. With this global trend of development of copper sulfide-based sustainable thermoelectric materials, researchers have revived interest in Cu_2SnS_3 (CTS) which had been well known as a solar cell material.

Recently, Shen et al. have reported that Zn-doped CTS ($Cu_2Sn_{0.9}Zn_{0.1}S_3$) exhibited a *ZT* value of 0.58 at 723 K.[7] Tan et al. have also reported that In-doped CTS ($Cu_2Sn_{0.9}In_{0.1}S_3$) exhibited a *ZT* value of 0.56 at 773 K.[8] Zhao et al. have reported that Co-doped CTS ($Cu_2Sn_{0.8}Co_{0.2}S_3$) exhibited a *ZT* value of 0.85 at 723 K.[9] On the other hand, multi-scale structuring has been regarded as one of the promising approaches to enhance the *ZT* value of a thermoelectric material by enhancing phonon scattering with maintaining good carrier transport properties. For example, Kanatzidis et al. fabricated a PbTe-SrTe thermoelectric material with a hierarchically organized multi-scale defect structure (panoscopic structure), i.e., atomic defects,

nano-endotaxial structures and mesoscale grain boundaries, which exhibited ZT = 2.2 at 915 K.[10] To fabricate panoscopic thermoelectric materials, the bottom-up preparation approach is promising in which chemically synthesized nanoparticles (NPs) are used as building blocks for making the panoscopic materials. This enables us to easily create exotic structures never before possible by introducing atomic defects in NPs (including impurities) during the synthesis, controlling size and shape of the NPs, blending two or more different types of NPs for making a bulk material, and controlling mesoscale defect structures by taking advantage of the pulse electric current sintering (PECS) technique.

With these in mind, in this chapter, we chemically synthesized uniform hole-doped CTS ($Cu_2Sn_{1-x}Zn_xS_3$) NPs and fabricated sustainable thermoelectric materials by sintering the NPs into dense bulk materials by PECS. Then, the structure and composition-property relationships in the $Cu_2Sn_{1-x}Zn_xS_3$ thermoelectric materials were analyzed. To avoid misunderstanding, we emphasize the differences between Cu_2ZnSnS_4 (CZTS) and $Cu_2Sn_{1-x}Zn_xS_3$ (Zn-doped CTS). CZTS has also been well known since early times as a promising quaternary p-type semiconductor material for solar energy conversion and photocatalysts with a bandgap of 1.45 -1.50 eV. In addition, a nanostructured bulk thermoelectric material has been fabricated by using chemically synthesized CZTS NPs.[11]

However, the ZT value of the nanostructured CZTS thermoelectric material was quite low (0.026 at 700 K) predominantly because of its low electrical conductivity. In contrast, the parent structure of Zn-doped CTS is a ternary p-type semiconductor with a bandgap of 0.9–1.3 eV.[12,13] In the case of Zn-doped CTS, Sn is partly substituted with Zn in the desired amounts. Pristine zinc blende (ZB) and wurtzite (WZ) Cu_2SnS_3 NPs were chemically synthesized as well as Zn-doped $Cu_2Sn_{1-x}Zn_xS_3$ NPs by a heat-up method.

The work in this chapter is one part of my Ph.D. research, which has been published in an article. This work was supported by Ms. Naoko Fujimoto and Mr. Atsushi Yamamoto of AIST

for operating and supporting the ZEM-3 and LFA457 measurements. Mr. Takida Hiroshi and Dr. Akatsuka Takeo in Nippon Shokubai Co., Ltd. supported the work of pelletization. The author also thank Koichi Higashimine of JAIST for helping with STEM-HAADF measurements and Dr. Miyata Masanobu of JAIST for helping with the DFT calculation.

2.2 Experiments

2.2.1 Materials

The chemicals have been used for the fabrication of $Cu_2Sn_{1-x}Zn_xS_3$ NPs are shown in Table 2.1. All chemicals were purchased from Sigma-Aldrich and used without any further purification.

Table 2.1. List of the chemicals, their chemical formula or abbreviation, and purity %.

Chemicals	Chemical Formula / Abbreviation	Purity %
Copper(II) nitrate hydrate	$Cu(NO_3)_2 \cdot xH_2O$	99.999
Copper(II) acetate hydrate	$Cu(CO_2CH_3)_2 \cdot xH_2O$ / $Cu(OAc)_2 \cdot xH_2O$	98.0
Tin(II) acetate	$Sn(CH_3CO_2)_2$ / $Sn(OAc)_2$	99.0
Zinc acetylacetonate hydrate	$Zn(C_5H_7O_2)_2 \cdot xH_2O$ / $Zn(acac)_2$	99.995
1-Dodecanethiol	$CH_3(CH_2)_{11}SH$ / DDT	>98
Oleylamine	$C_{18}H_{35}NH_2$ / OAM	70.0
Thiourea	$SC(NH_2)_2$ / TU	99.0
Hexane	$CH_3(CH_2)_4CH_3$	96.0
Methanol	CH_3OH	99.8
Ethanol	C_2H_5OH	99.5
Toluene	$C_6H_5CH_3$	99.0

2.2.2 Fabrication of Cu-Sn-S Nanoparticles

Briefly, 4 mmol of copper(II) nitrate hydrate [$Cu(NO_3)_2$], 2 mmol of tin(II) acetate [$Sn(OAc)_2$], 100 mL of oleylamine (OAM) and 100 mL of 1-dodecanthiol (DDT) were put into a 500-mL three-necked flask equipped with a dry Ar inlet/outlet, trap sphere, condenser, heating mantle, thermometer, and magnetic stirrer. First, the reaction mixture was stirred with Ar bubbling at room temperature for 5 min. Then the temperature was increased to 100 ºC and kept for 10 min with Ar bubbling to remove volatile matter. Subsequently, the reaction temperature was further raised to 260 ºC and kept for 1 h. The synthetic scheme as shown in the Figure 2.1. After the reaction, the NPs were separated from the reaction mixture by centrifugation at 5000 rpm for 3 min. Then, the NPs were washed twice by repeating the following purification cycle: redispersion in hexane, addition of ethanol, centrifugation, and supernatant removal. Finally, the NPs were dried in vacuum. Pristine zincblende (ZB) Cu_2SnS_3 NPs were also synthesized by using copper(II) acetate hydrate [$Cu(OAc)_2$] as a Cu precursor and changing the volume ratio of OAM to DDT was 3:1 keeping the total amount of solvent constant (OAM + DDT = 200 mL). Other synthesis conditions were exactly the same as those for synthesis of WZ Cu_2SnS_3 NPs and used for subsequent characterization.

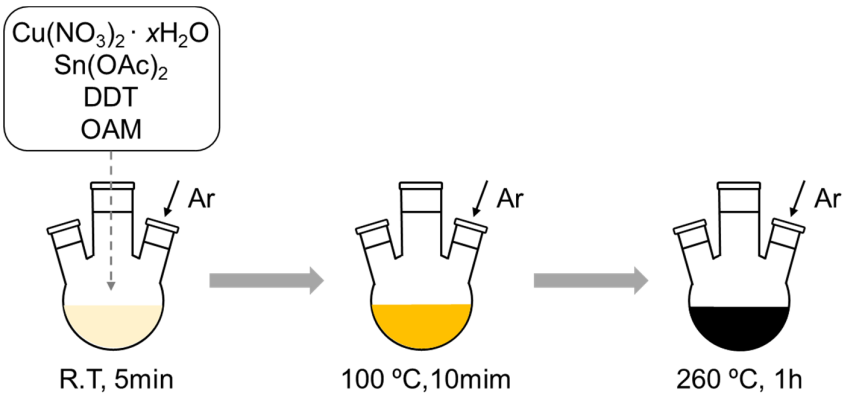

Figure 2.1. Synthetic scheme of Cu-Sn-S NPs system.

2.2.3 Fabrication of $Cu_2Sn_{1-x}Zn_xS_3$ Nanoparticles

Hole-doped $Cu_2Sn_{1-x}Zn_xS_3$ NPs were synthesized in a similar manner as described in section 2.2.2 by varying the input molar ratio of zinc(II) acetylacetonate hydrate [$Zn(acac)_2$] to tin(II) acetate [$Sn(OAc)_2$] and keeping the total amount of those two precursors constant [$Zn(acac)_2$ + $Sn(OAc)_2$ = 2 mmol].

The input amount of chemicals are shown in the Table 2.2. In this study, 6 different types of NPs were synthesized, i.e., ZB Cu_2SnS_3, WZ Cu_2SnS_3, $Cu_2Sn_{0.95}Zn_{0.05}S_3$, $Cu_2Sn_{0.9}Zn_{0.1}S_3$, $Cu_2Sn_{0.85}Zn_{0.15}S_3$, and $Cu_2Sn_{0.8}Zn_{0.2}S_3$ NPs will be referred to as Samples A, B,C, D, E, and F, respectively, hereafter.

Table 2.2. Input amount of chemicals for the $Cu_2Sn_{1-x}Zn_xS_3$ NPs system.

Sample	$Cu(NO_3)_2 \cdot xH_2O$ (mmol)	$Cu(OAc)_2 \cdot xH_2O$ (mmol)	$Zn(acac)_2$ (mmol)	$Sn(OAc)_2$ (mmol)	DDT/OAM (mL)
Sample A	-	4	-	2	50/150
Sample B	4	-	-	2	100/100
Sample C	4	-	0.1	1.9	100/100
Sample D	4	-	0.2	1.8	100/100
Sample E	4	-	0.3	1.7	100/100
Sample F	4	-	0.4	1.6	100/100

2.2.4 Ligand Exchange

It is worthy knowing that we should have great of concern about the organic capping species on the surface because of their roles in directing morphology and protecting the NPs from aggregation and oxidation. Moreover, the organic nature of the remaining capping molecules

on the surface of NPs often causes a significant decrease of electrical conductivity, which has effect on the overall TE efficiency. It is necessary to propose some solutions and modulations to avoid the electrical conductivity decrease caucused by surface ligand.

Because the as synthesized NPs were capped with insulating organic ligands (DDT and OAM), it is necessary to remove those ligands from the surface of NPs before making a pellet. Although the most straightforward way to remove those organic ligands is the thermal treatment of the NPs under inert atmosphere, it leads to the undesirable grain growth of the NPs because high temperature (>450 ºC) and long-time treatment is required. Therefore, ligand exchange of the NPs from DDT/OAM to thiourea (TU) was carried out, because TU sublimates at approximately 170 ºC under reduced pressure and thermally decomposes in the temperature range higher than 230 ºC.[14]

Briefly, 4 g of TU was dissolved in 160 mL of methanol. Then the solution was added into a 100-mL toluene dispersion of the NPs (1.36 g of the NPs was dispersed) followed by sonication for 1 h at room temperature. After the ligand exchange reaction, the TU-capped NPs were separated from the solution by centrifugation at 5000 rpm for 3 min. The TU-capped NPs were washed by the following process: redispersion in hexane/toluene mixture, centrifugation, and supernatant removal. Finally, the resulting TU-capped NPs were redispersed in methanol, and then toluene was added to the dispersion followed by centrifugation at 5000 rpm for 10 min to remove excess TU. Schematic illustration of ligand exchange for $Cu_2Sn_{1-x}Zn_xS_3$ NPs system as shown in Figure 2.2(a).

To know the organic residues on the surface of NPs, the thermogravimetric analyses (TGA, TGA/SDTA851e) was performed. Figure 2.2(b) shows the weight with temperature dependence of Sample D. It suggested that TU thermally decomposes around 170 ºC, while remained DDT/OAM (boiling temperature around 266-288 ºC, 350 ºC) thermally decomposes around 400 ºC. One should note that a small amount of organic residues (6 wt. %) remains in

the sample after ligand exchange. With temperature increase, the organic residues will decrease to less than 1 wt. %.

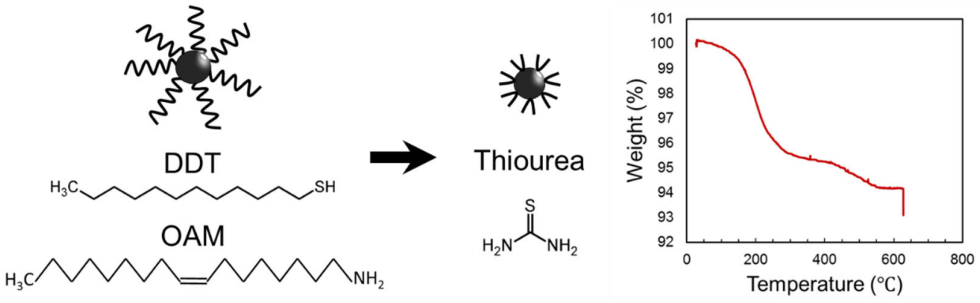

Figure 2.2. (a) Schematic illustration of Ligand exchange for $Cu_2Sn_{1-x}Zn_xS_3$ NPs system, (b) TGA of $Cu_2Sn_{0.85}Zn_{0.15}S_3$ nanoparticles after ligand exchange.

Such less organic residues can not be removed completely even after pelletization. On one hand, the insulate residue helps preventing the material from oxidation in the ambient environment. On the other hand, it usually lead to a reduced electrical conductivity and thermal conductivity. Therefore, intentionally control the amount of residue could be an alternative approach to enhance the *ZT* value in the material, which is worthy investigating. For the first demonstration purpose, the smallest amount of residues, *i.e.,* 1 wt. % which should barely affect the main experimental result.

2.2.5 Pelletization

TU-capped Samples A-F were then pelletized into solid disks with a diameter of 10 mm and a thickness of 2 - 3 mm by using a pulse electric current sintering (PECS) machine (Sinterland LABOX-100) under the following conditions: temperature: 450 ºC, pressure: 30 MPa, and sintering time: 5 min. In this process, a large pulsed electric current is applied to heat the graphite mold and the powder specimen, which is subjected to a modest pressure inside the mold. Schematic illustration of pulse electric current sintering (PECS) technique as shown in

Figure 2.3. Pellets composed of Samples A-F will be referred to as Pellets A-F, respectively, hereafter.

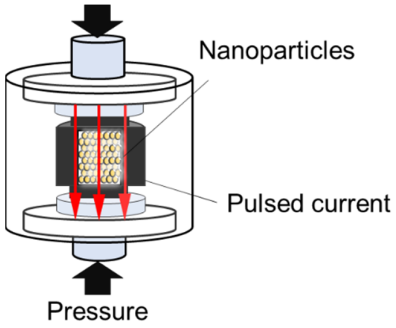

Figure 2.3. Schematic illustration of pulse electric current sintering (PECS) technique.

2.3 Characterization Techniques

As-synthesized Samples A-F were characterized by transmission electron microscopy (TEM, Hitachi H-7650) at 100 kV, X-ray diffraction (XRD, Rigaku MiniFlex600 with Cu Ka), and inductively coupled plasma optical emission spectroscopy (ICP-OES, Shimadzu ICPS-7000). Pellets A-F were characterized by XRD, ICP-OES and a scanning TEM (STEM) equipped with a high-angle annular dark-field (HAADF) detector, and energy-dispersive X-ray spectroscopy (EDS) elemental mapping. STEM-HAADF imaging and EDS elemental mapping were performed on a JEOL JEM-ARM200F microscope operated at 200 kV with a spherical aberration corrector and a nominal resolution of 0.8 A ˚. The specimens for the cross-sectional STEM analyses were prepared by a focused-ion beam (FIB) method (Figure 2.4).

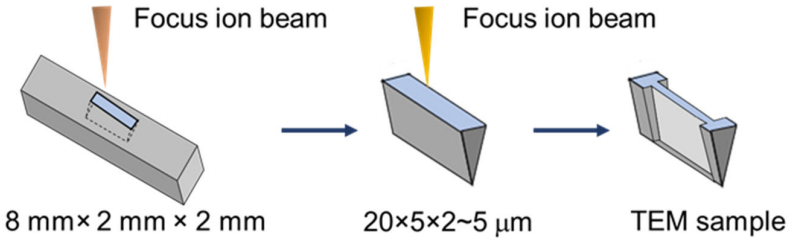

Figure 2.4. Schematic illustration of sample preparation by FIB for STEM measurement.

2.3.1 Thermal Conductivity Measurement

The samples used for thermal conductivity measurements are solid disks with diameter of 10 mm and thickness of 2-3 mm whose surfaces were coated by graphite spray. First, κ was measured for the pellet in the cross-plane direction by laser flash analysis (Netzsch LFA457). In this method, κ ($W \cdot m^{-1} \cdot K^{-1}$) was calculated as $\kappa = dcD$ where d ($kg \cdot m^{-3}$), c ($J \cdot kg^{-1} \cdot K^{-1}$) and D ($m^2 \cdot s^{-1}$) are density, specific heat and thermal diffusivity of the pellet, respectively. The densities of pellets were determined using a gas pycnometer (Shimadzu AccuPyc II 1340). The values of D were directly measured, while the values of c were indirectly derived from a standard sample (Netzsch Pyroceram 9606) under an Ar gas flow of 100 $mL \cdot min^{-1}$ over a temperature range of 300-670 K. The relative uncertainty of κ was estimated to be smaller than 8% based on the uncertainties of d, c and D. Figure 2.5 shows the illustration of setting up for thermal conductivity measurement.

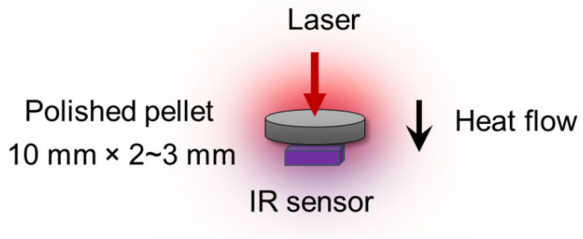

Figure 2.5. Schematic illustration of set up for thermal conductivity measurement.

2.3.2 Seebeck and Electrical Conductivity Measurements

Then, Seebeck coefficient (S) and electrical resistivity (ρ) were measured in the in-plane direction as shown in Figure 2.6 (cutting the pellet into a rectangular bar with dimensions of approximately 2 mm × 2 mm × 8 mm) by temperature-differential and four-probe methods, respectively, under a He atmosphere (Advance Riko ZEM-3). In this method, S ($V \cdot K^{-1}$) is determined by the ratio of electromotive to the temperature difference as shown in the equation $S = \Delta V / \Delta T$. Electrical conductivity σ ($S \cdot m$) is given by the equation $\sigma = 1/\rho$ where ρ is determined

by the electromotive to the current. The relative uncertainty of S and σ were estimated to be 5%. The ZT values were calculated with those uncertainties in mind.

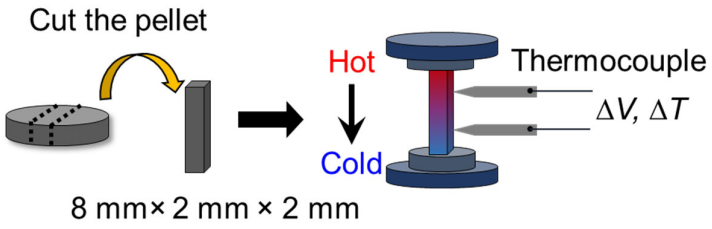

Figure 2.6. A diagram is shown for the sample cutting using for ρ and S measurement.

2.3.3 Hall Measurement

After the thermoelectric measurements, Pellet B, Pellet D and Pellet E were polished to thin blocks approximately 4 mm × 2 mm × 0.5 mm by using sand paper. The electrodes were bonded to the rectangular in-plane specimen using gold paste. Then hall measurement was performed. The Hall voltage V_H was measured at 300 K using a physical properties measurement system (PPMS; Quantum Design) by applying a magnetic field of ±5 T with an AC current. The AC current applied for these three samples was 60mA.

The Hall Effect[15] is due to the nature of the current in a conductor, which is very useful as a mean to measure the carrier density. Current consists of the movement of charger carriers. When a perpendicular magnetic field is present, charge carriers will experience a force, called the Lorentz force. The moving path of charger carriers are curved. Thus, moving charges accumulate on one face of the material, the opposite and equal chargers will expose on the other face. The separation of charge establishes an electric field that opposes the migration of further charge. When the Lorentz force and the electric field force are balanced on the charge carrier, as long as the charge starts flowing, then a steady electric potential is established.

The Hall coefficient R_H was calculated as $R_H = V_H d/BI$, where V_H, d, B and I are the Hall voltage, the thickness of specimen, external magnetic field and current, respectively. Assuming

single carrier transport, carrier concentration n and Hall mobility μ were calculated as $n = 1/|R_H|e$ and $\mu = R_H\sigma$, where e is elementary charge. The configuration for the measurement of Hall voltage and setting up of sample for hall measurement are shown in Figure 2.7.

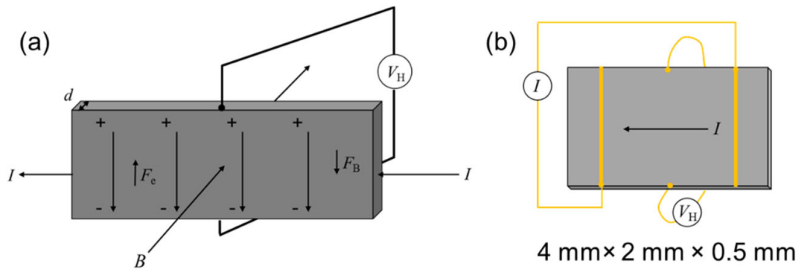

Figure 2.7. (a) A diagram illustrating the configuration for the measurement of the Hall voltage, (b) Setting up of sample for Hall measurement.

2.4 Results and Discussion

2.4.1 Morphology and Crystal Structure

In order to observe the morphology of obtained NPs, after the synthesis and washing process, the samples for TEM were prepared by dropping the suspended particles in hexane onto a carbon coated copper grid and drying in vacuum overnight. Figure 2.8 shows the TEM images of as-synthesized Samples A-F. All samples are relatively uniform in size and shape except for Sample A. Interestingly, Samples B-F have a hexagonal pencil-like morphology. By analyzing the TEM images, it was found that Samples B-F all have nearly the same size and shape. The relationship between sizes and Zn contents is shown in Figure 2.9. The average length and width of the NPs were calculated to be around 40 and 25 nm, respectively.

The reaction mechanism to obtain CTS NPs with WZ or/and ZB phase have been studied by many researchers. In this synthesis scheme, all precursors were added into the solvent at the beginning of the reaction. The mixture is steadily heated to induce thermal decomposition of precursors followed by nucleation and grain growth. Researchers studied that different metallic precursors, sulfur source and solvents could affect CTS nanoparticle synthesis.[16-17] Using

highly reactive sulfur source, strong coordinating solvent and capping agents can produce metastable phase of CTS. In this synthesis, OAM was used as solvent, DDT act as sulfur source as well as capping agent. Simultaneous control of phase and size of CTS NPs was studied by Park et al.[18] He found that WZ CTS phase was produced when DDT used as sulfur sources because of DDT being less reactive has low activation rate of S^{2-} ions and hence the reaction temperature was high (>200 ºC). The higher reaction temperature (260 ºC) in this reaction scheme lead to the activation rate of S^{2-} ions become faster and favor CTS WZ phase.

It was also reported that the reason for forming different phase structures is the initial redox conditions, when the reaction was conducted under a reducing condition, Cu_2S (or $Cu_{31}S_{16}$) seeds were formed, leading to the formation of wurtzite CTS nanocrystals. When the condition were less reducing, the initial CuS (or $Cu_{1.84}S$) seeds resulted in zincblende structure CTS nanocrystals. The reducing condition can be tuned by varying the input amount of DDT and OAM.

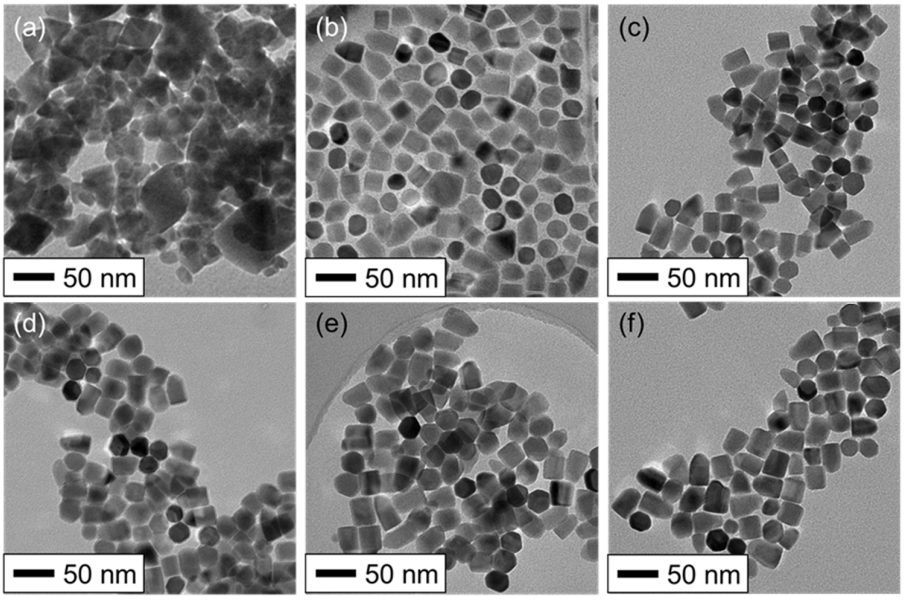

Figure 2.8. TEM images of CTS (a) and (b) and Zn-doped CTS (c) - (f) NPs: (a) Sample A (ZB), (b) Sample B (WZ), (c) Sample C (x = 0.05), (d) Sample D (x = 0.1), (e) Sample E (x = 0.15), and (f) Sample F (x = 0.2).

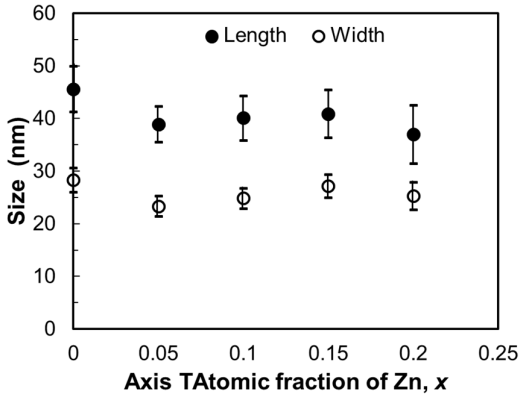

Figure 2.9. The plot of lengths (closed circle) and widths (open circle) of Sample B-F(*x*=0-0.2).

In our control experiments, it was confirmed that input amount of DDT and OAM could affect the phase of nanoparticles as shown in Figure 2.10 and Figure 2.11. When $Cu(OAc)_2 \cdot xH_2O$ was used as copper source in the same synthesis scheme and keep the same input mole ratio of copper and tin precursor (0.2 mmol / 0.1 mmol), when the input amount of OAM and DDT (the total amount is 10 mL) was changed, the ZB CTS phase was obtained when DDT was 3mL.

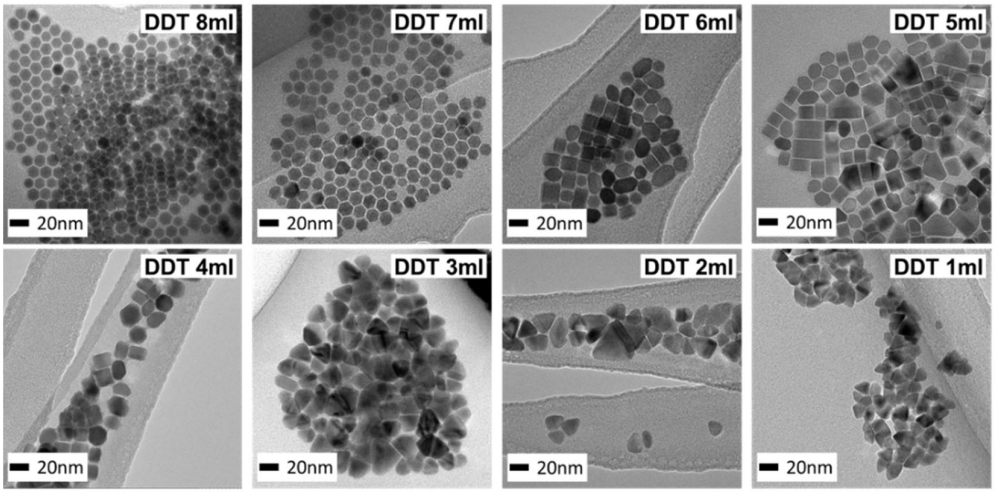

Figure 2.10. TEM images of obtained NPs in the control experiments by varying the input molar ratio of OAM and DDT when $Cu(OAc)_2 \cdot xH_2O$ was used as copper source. The total amount of OAM and DDT was 10mL.

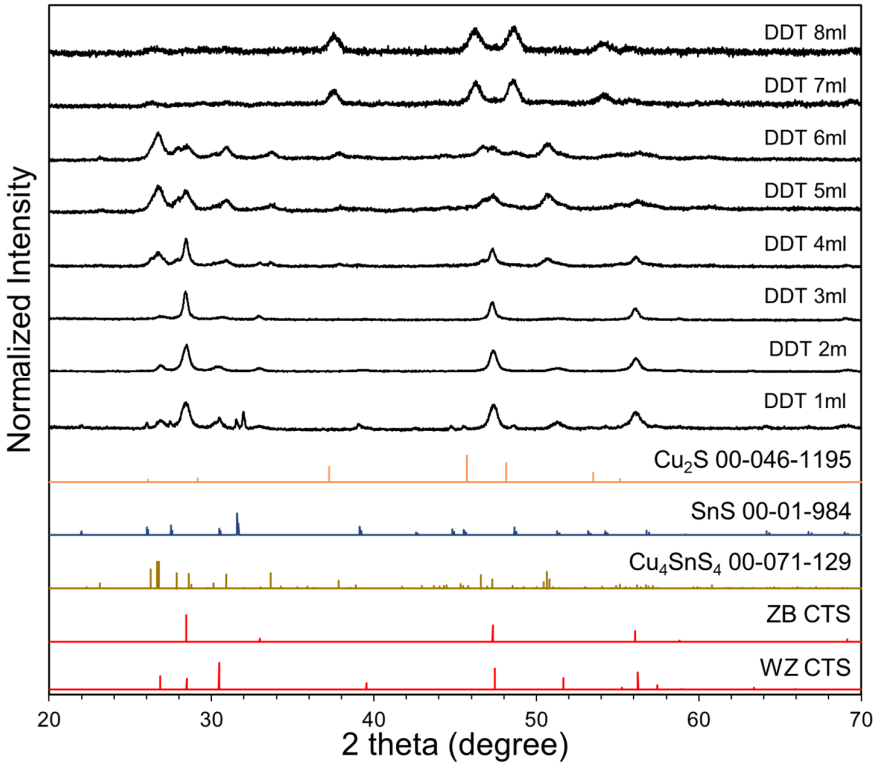

Figure 2.11. XRD patterns of obtained NPs in the control experiments by varying the input molar ratio of OAM and DDT when $Cu(OAc)_2 \cdot xH_2O$ was used as copper source. The total amount of OAM and DDT was 10mL. The reference XRD patterns of WZ and ZB CTS are also shown for comparison.[19]

The crystal structure of all the Samples A-F and Pellets A-F were also characterized. Figure 2.12 shows the XRD patterns of Samples A-F [Fig. 2.12 (a)] and Pellets A-F [Fig. 2.12 (b)]. As shown in Fig. 2.12 (a), the primary crystal phase of Sample A is ZB with small amounts of WZ phase (the reference XRD patterns of WZ and ZB CTS were taken from the Ref.19), while the primary crystal phase of Samples B-F is WZ with small amounts of ZB phase. As shown in Fig. 2.12 (b), the phase transition from WZ to ZB is clearly seen for Pellets B-F. Specifically, Pellets E and F have a phase-pure ZB crystal structure, while Pellets B-D contain small amounts of residual WZ phase. The reason why only Pellets E and F could obtain a phase-pure ZB structure is possibly because the phase transition temperature decreased by increasing the Zn impurity concentration.

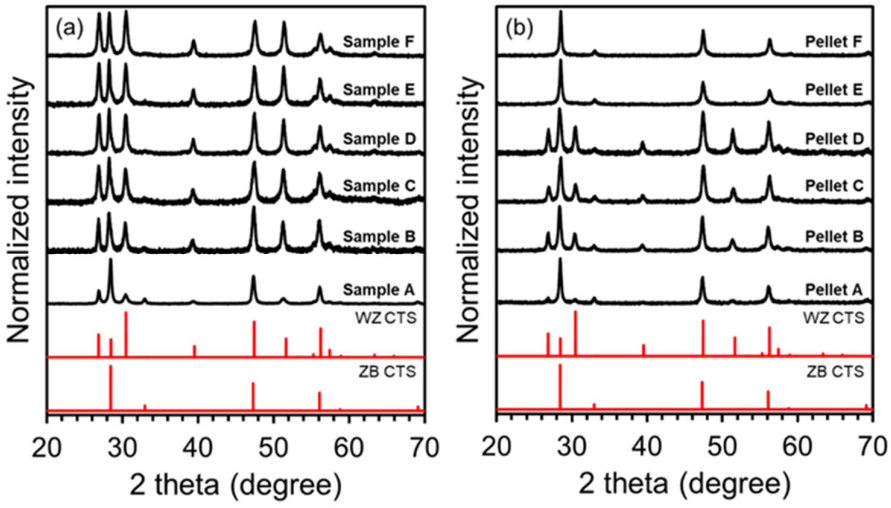

Figure 2.12. XRD patterns of (a) Samples A-F and (b) Pellets A-F. The reference XRD patterns of WZ and ZB CTS are also shown for comparison.[18]

The mean crystalline sizes (D_{xrd}) of Samples A-F and Pellets A-F were estimated using Scherrer's equation as shown in Table 2.3 for the three intense diffraction peaks. As a result, the most intense diffraction peak of the primary phase were chosen for Samples A-F for comparison. The values of D_{xrd} were calculated to be 24.5, 18.3, 16.9, 20.0, 19.6, and 18.3 nm, respectively. On the other hand, the values of D_{xrd} for Pellets A-F were calculated to be 26.8, 21.4, 19.0, 18.2, 24.5, and 27.6 nm, respectively, indicating that the mean crystalline size remains virtually unchanged during sintering for all pellets. The reason why the mean crystalline size of Sample D decreased after the sintering is due to the broadening of the primary peak of the ZB phase caused by the non-negligible amount of WZ residue.

The densities of Pellets A-F were determined to be 4.45, 4.43, 4.57, 4.56, 4.50, and 4.48 g/cm^3, respectively, using a gas pycnometer (Shimadzu AccuPyc II 1340). Because the density of monocrystalline ZB CTS is 4.73 g/cm^3, the relative densities of Pellets A-F were calculated to be 94 ~ 97%. The results are shown in the Table 2.4. These results indicated that PECS technique has ability of rapidly heating the powder compact to high temperatures

and consolidating it to high densities within very short time suppressing grain growth for these samples.

Table 2.3. Summary of mean crystalline size (nm) of NPs and Pellets.

		Peak 1 (2θ = ~ 26.9°)	**Peak 2 (2θ = ~ 28.4°)**	**Peak 3 (2θ = ~ 30.5°)**
Sample A	NPs	24.4	24.5	13.9
	Pellet	24.4	26.8	15.1
Sample B	NPs	24.4	18.6	18.3
	Pellet	23.7	21.4	19.6
Sample C	NPs	18.6	18.6	16.9
	Pellet	19.9	19.0	17.2
Sample D	NPs	20.8	22.0	20.0
	Pellet	21.3	18.2	19.6
Sample E	NPs	20.3	23.8	19.6
	Pellet	N/A	24.5	N/A
Sample F	NPs	18.1	22.5	18.3
	Pellet	N/A	27.6	N/A

Table 2.4. The Density and Relative density of Pellets A-F.

Sample	**Density (g/cm^3)**	**Relative Density (%)**
Pellet A	4.45	94
Pellet B	4.43	94
Pellet C	4.57	97
Pellet D	4.56	96
Pellet E	4.50	95
Pellet F	4.48	95

In order to check the homogeneity, Pellets B and D were choose for the cross-sectional STEM-HAADF and EDS elemental mapping measurement. Their images are shown in Fig. 2.13. The contrast of the STEM-HAADF image is relatively uniform in both cases even though

some dark areas were observed suggesting the successful formation of homogeneous pellets. The EDS elemental mapping images also confirm that the pellets are compositionally uniform.

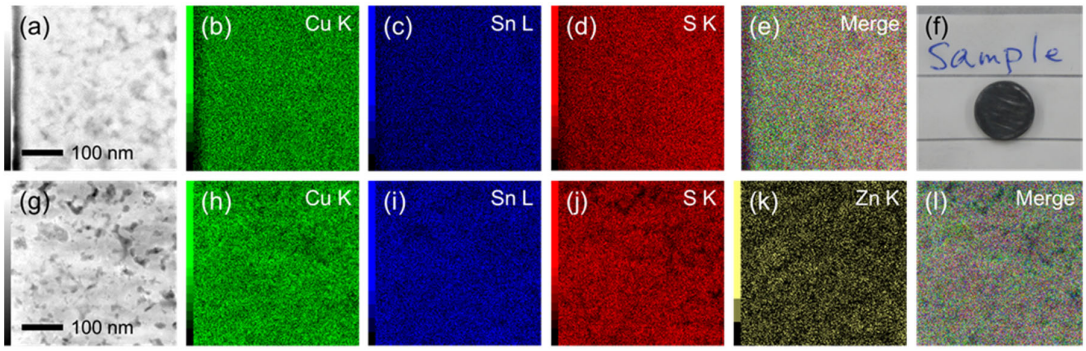

Figure 2.13. Cross-sectional STEM-HAADF and EDS elemental mapping images of (a-e) Pellet B and (g-l) D. (f) A photograph of Pellet B (10 mmϕ ×1.9 mm). (a,g) STEM-HAADF images. (b,h) Cu K edge, (c,i) Sn L edge, (d,j) S K edge, (k) Zn K edge and (e,l) overlay.

2.4.2 Compositional Analysis

To get better understanding of the compositions of samples, inductively coupled plasma optical emission spectroscopy (ICP-OES) measurement was performed on all the Samples A-F and Pellets A-F. The Cu:Sn:Zn atomic ratios of as-synthesized Samples A-F were determined to be 68:32:0, 69:31:0, 67:31:2, 65:31:4, 63:31:6, and 63:29:8, respectively. The values of x were calculated to be 0, 0, 0.06, 0.11, 0.16, and 0.21 for Samples A-F, respectively, which correspond to the input molar ratio of Zn to Sn precursors. This result indicates that Zn was doped stoichiometrically to Cu_2SnS_3 substituting Sn presumably because of its similar ionic radius to those of Sn^{4+} (55 pm, C.N. = 4) and Cu^{+} (60 pm, C.N. = 4).[7, 20] The Cu:Sn:Zn atomic ratios of Pellets A-F were determined to be 69:31:0, 67:33:0, 69:29:2, 65:31:4, 68:27:5, and 66:26:8, respectively. These results shown that the contents of each elements in all the pellets maintained without losing during the sintering. The ICP-OES determined atomic compositions for Samples A-F and Pellets A-F are shown in Table 2.5.

Table 2.5. ICP-OES detrmined atomic compositions for Sample A-F and Pellet A-F.

Sample	ICP-OES		
	Cu (at %)	Sn (at %)	Zn (at %)
Sample A	68	32	0
Pellet A	69	31	0
Sample B	69	31	0
Pellet B	67	33	0
Sample C	67	31	2
Pellet C	69	29	2
Sample D	65	31	4
Pellet D	65	31	4
Sample E	63	31	6
Pellet E	67	27	6
Sample F	63	29	8
Pellet F	66	26	8

As a result, we successfully obtained different phase of CTS NPs and hole-doped CTS NPs with varying Zn contents by using chemical method. The resulting NPs were pelletized for further thermoelectric properties characterization.

2.4.3 Thermoelectric Properties

2.4.3.1 Nanostructuring Effect on the Thermal Conductivities

Finally, the thermoelectric measurements were performed on Pellets A-F. First thermal conductivity (κ) was measured for the pellet in the cross-plane direction by laser flash analysis (Netzsch LFA457). In this method, κ ($W \cdot m^{-1} \cdot K^{-1}$) was calculated as $\kappa = dcD$ where d ($kg \cdot m^{-3}$), c ($J \cdot kg^{-1} \cdot K^{-1}$) and D ($m^2 \cdot s^{-1}$) are density, specific heat and thermal diffusivity of the pellet, respectively. The values of c and D for Pellet A-F are shown in Fig. 2.14. The relative uncertainty of κ was estimated to be smaller than 8% based on the uncertainties of d, c and D.

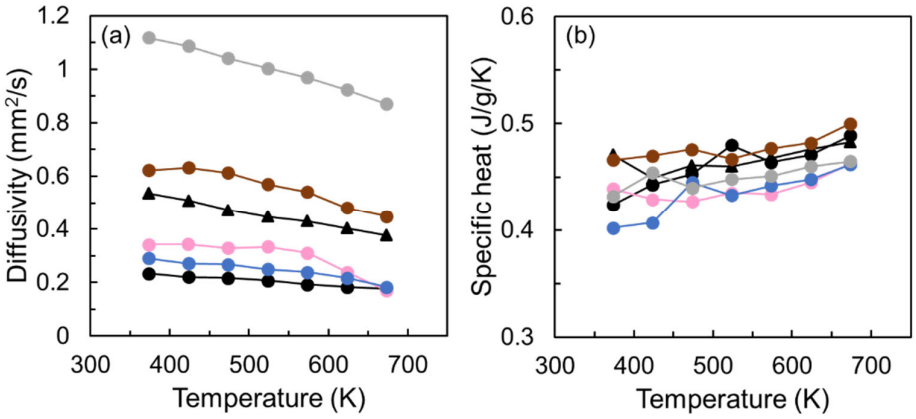

Figure 2.14. (a) Thermal diffusivity D and (b) specific heat c of Pellet A-F. Filled black triangles, filled black circles, filled pink circles, filled blue circles, filled brown circles, and filled gray circles represent Pellet A-F, respectively.

The comparison of thermal diffusivities and specific heat on Pellet A-F are shown in Figure 2.14 (a) and (b), respectively. It was noted that c might be considered independent of any small amount of additional Zn doping in these pellets. As see in Figure 2.14 (a), Pellet A, E, F have higher D than pellet B, this is presumably because Pellet A, E, F have more the highly symmetric cubic structure which leads to the higher heat carrier mobility resulting in higher thermal diffusivity. Pellet B-D have similar thermal diffusivities. The phenomenon in the thermal diffusivity is the same as thermal conductivities that will be discussed later.

As we know, the total thermal conductivity contains lattice thermal conductivity (κ_{lat}) and carrier thermal conductivity (κ_{car}). The carrier thermal conductivity (κ_{car}) was calculated by Wiedemann-Franz's law $\kappa_{car} = L\sigma T$ where L and σ denote the Lorenz number (2.44×10^{-8} $W\cdot\Omega\cdot K^{-2}$) and electrical conductivity, respectively. Then lattice thermal conductivity (κ_{lat}) was calculated as $\kappa_{lat} = \kappa - \kappa_{car}$. The values of pellets are shown in Figure 2.15.

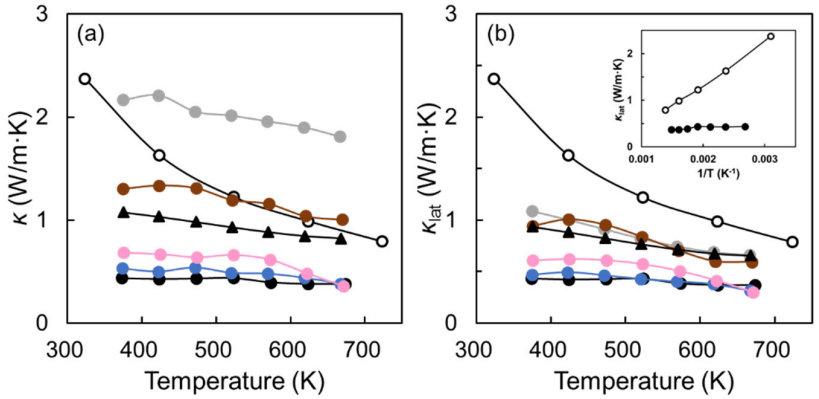

Figure 2.15. (a) Thermal diffusivity κ and (b) lattice thermal conductivity κ_{lat} of Pellet A-F. Filled black triangles, filled black circles, filled pink circles, filled blue circles, filled brown circles, and filled gray circles represent Pellet A-F, respectively. The open circle represents the data of undoped non-nanostructured monoclinic CTS taken from Ref.7. The inset of (b) shows lattice thermal conductivities of Pellet B (filled black circles) and undoped non-nanostructured CTS (open circles) plotted with respect to the reciprocal of temperature.

For comparison, the data of undoped non-nanostructured CTS taken from Ref.7 are shown in Figure 2.15. As seen in Figure 2.15 (a) and (b), Pellet B had lower κ and κ_{lat} values than non-nanostructured CTS. This suggests that the phonon scattering is successfully facilitated by nanostructuring. It is more evident in the inset of Figure 2.15 (b), where κ_{lat} of non-nanostructured CTS exhibits the classical $1/T$ dependence caused by Umklapp scattering, while the characteristic $1/T$ dependence of κ_{lat} completely disappears in the case of Pellet B supporting the fact that the phonon scattering is dominated by defect scattering. In the case of non-nanostructured CTS, it has been reported that a chemically ordered monoclinic phase has larger κ_{lat} than the chemically disordered cubic/tetragonal phase.[7] This might be because the random distribution of metal atoms and vacancies plays an important role in suppressing κ_{lat} possibly by thoroughly disrupting the normal phonon transport. In the present case, Pellets A, E, and F (ZB CTS without the WZ phase) exhibited higher κ_{lat} than Pellets B-D (ZB CTS with the WZ phase). This is presumably because the coexistence of ZB and WZ phases is responsible for the phonon scattering at the interfaces and grain boundaries.

2.4.3.2 Doping Effect on the Electrical Transport Properties

Then, we measured S and σ in both heating and cooling cycles for all the pellets and found that the values coincide in both cycles are shown in Figure 2.16 and Figure 2.17. Therefore, the values only in the heating cycle for all the pellets are shown in Figure 2.19 for further discussion. The power factor (PF) and ZT values were calculated as $PF = \sigma S^2$ and $ZT = \sigma S^2 T/\kappa$, respectively. The ZT values of Pellets A-F with error bars also shown in Figure 2.18.

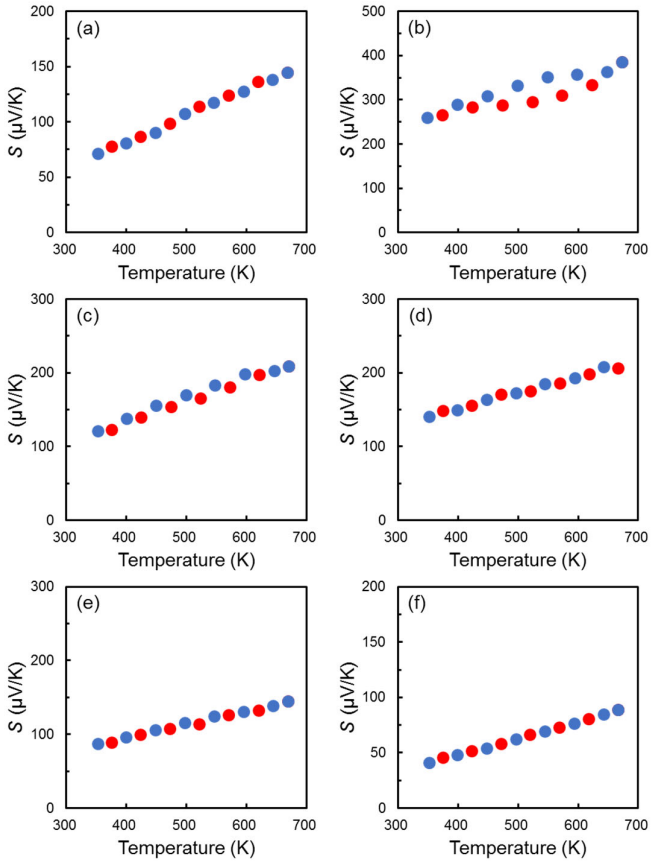

Figure 2.16. Seebeck coefficients of (a) Pellet A, (b) B, (c) C, (d) D, (e) E and (f) F. Red and blue circles represent data measured in heating and cooling cycles, respectively.

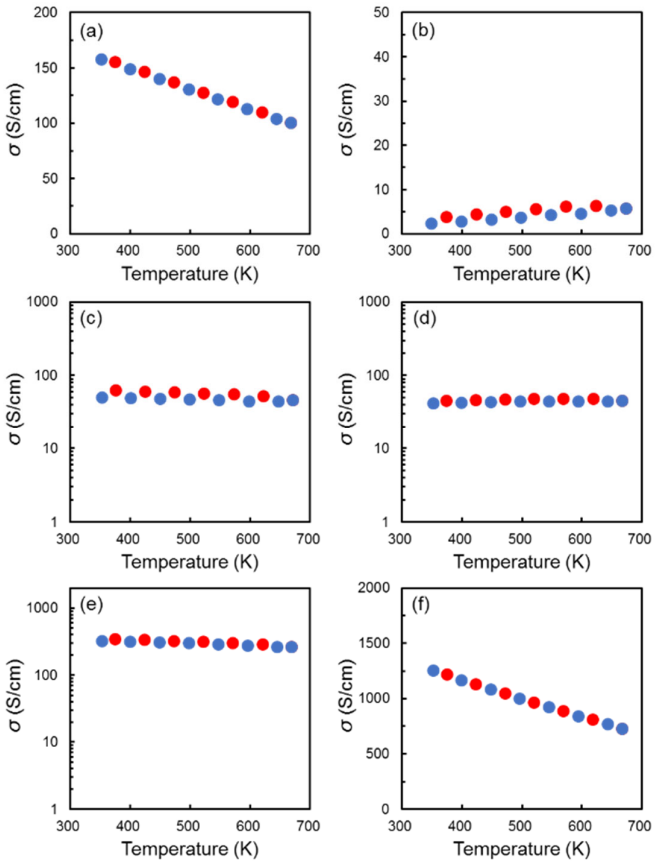

Figure 2.17. (a) Electrical conductivities of (a) Pellet A, (b) B, (c) C, (d) D, (e) E and (f) F. Red and blue circles represent data measured in heating and cooling cycles, respectively.

As seen in Figure 2.19 (a), (b) and (c), Pellet B showed similar values of σ, S and PF as non-nanostructured CTS, while it had lower κ and κ_{lat} than non-nanostructured CTS (Figure 2.15). This suggests that the phonon scattering is successfully facilitated with maintaining good carrier transport properties by nanostructuring. As shown in Figure 2.19 (a), the sign of S is positive in all cases, confirming p-type carrier transport. With increasing Zn concentration, x, in the Zn-doped CTS (Pellet C-F), a systematic increase in σ was observed [Figure 2.19 (b)], while S decreased in an opposite manner. In addition, σ of Pellet B increases with increasing temperature showing a semiconductor behavior, while σ of Pellet C-F remains unchanged or decreases with increasing temperature showing a metallic behavior.

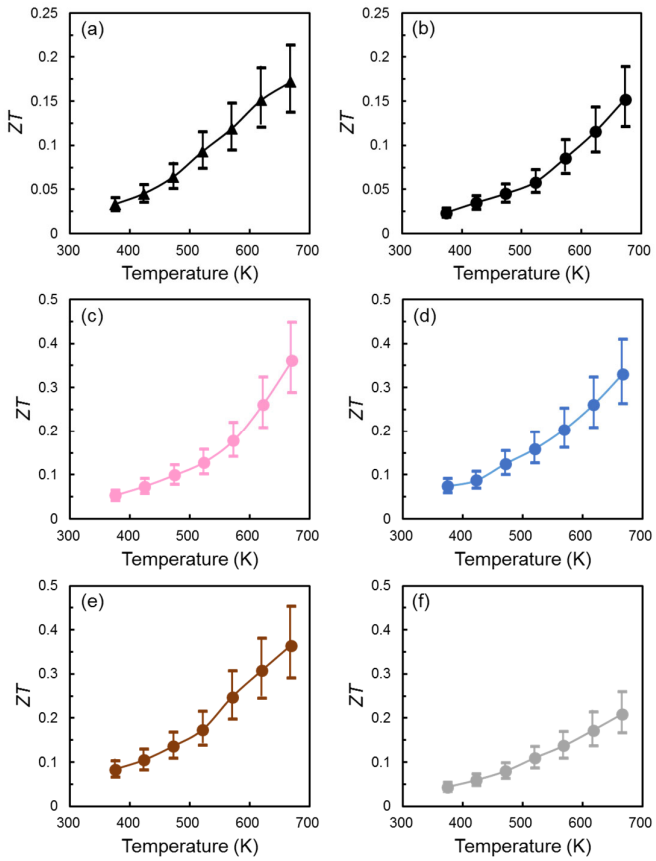

Figure 2.18. The *ZT* values for (a) Pellet A, (b) B, (c) C, (d) D, (e) E and (f) F.

To clarify the effect of Zn-doping on the electronic structure of CTS, the density of states (DOS) of undoped CTS (ZB-phase Cu_2SnS_3) and Zn-doped CTS (ZB phase $Cu_2Sn_{0.9375}Zn_{0.0625}S_3$) was determined using first principles calculations based on density functional theory (DFT) within the generalized gradient approximation (GGA) in the scheme of Perdew-Burke-Ernzerhof (PBE) functional with the consideration of spin-orbit coupling (SOC) as shown in Figure 2.20. In consequence, it has been found that the chemical potential (l) decreases by substituting Sn with Zn leading to hole doping. As a result, σ increases while S decreases.

To look insight of the electrical transport properties, Hall Effect measurement were performed on Pellet B, D and E at 300 K to determine the carrier concentrations and carrier

mobilities. The values of σ, n and μ at room temperature of Pellet B, D and E are shown in Table 2.6.

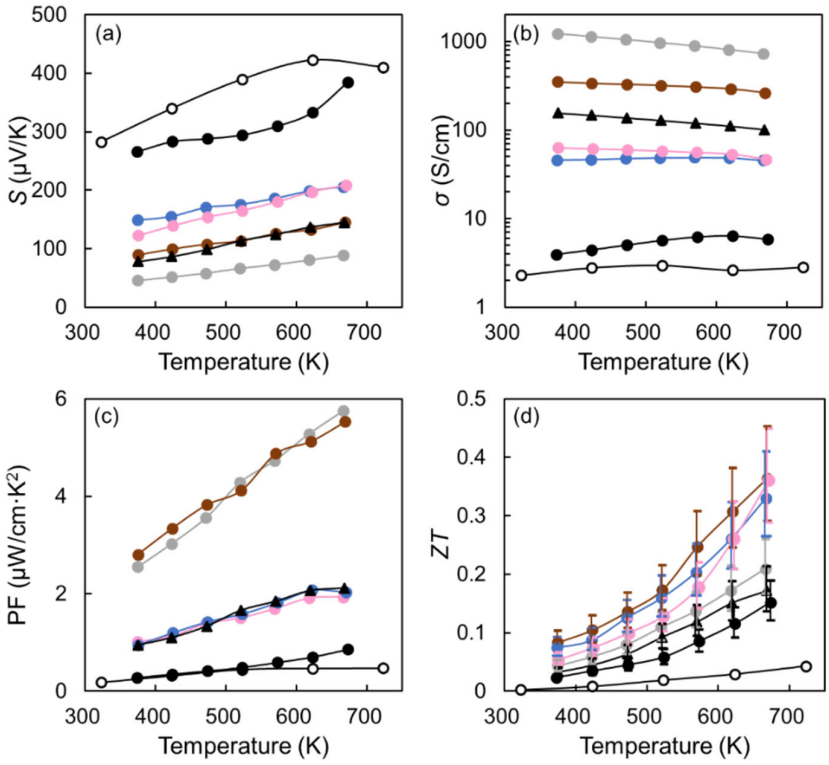

Figure 2.19. (a) Electrical conductivity σ, (b) Seebeck coefficient S, (c) power factor PF, (d) ZT with error bars of Pellets A-F. Filled black triangles, filled black circles, filled pink circles, filled blue circles, filled brown circles, and filled gray circles represent Pellet A-F, respectively. The open circle represents the data of undoped non-nanostructured monoclinic CTS taken from Ref.7. It should be noted that we measured S and σ in both heating and cooling cycles and found that the values coincide in both cycles. Therefore, the values only in the heating cycle are shown here.

Table 2.6. σ, n and μ (at 300K) of Pellet B, Pellet D and Pellet E.

	σ ($S \cdot cm^{-1}$)	n (cm^{-3})	μ ($cm^2 \cdot V^{-1} \cdot s^{-1}$)
Pellet B (x=0)	3.4	6.90×10^{19}	0.31
Pellet D (x=0.1)	45.3	1.96×10^{21}	0.14
Pellet E (x=0.15)	364.8	2.07×10^{21}	1.10

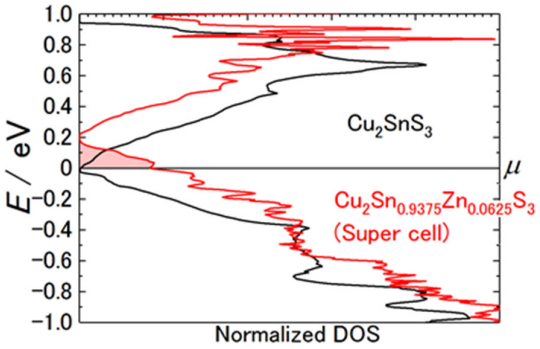

Figure 2.20. DOS of undoped (red curve) and Zn-doped CTS (x = 0.0625).

It can be seen that in Table 2.6, the carrier concentration increased from 6.90×10^{19} cm^{-3} to 2.07×10^{21} cm^{-3} with Zn contents increased from 0 (Pellet B) to 0.15 (Pellet E), confirming that Zn doping can increase the carrier concentration of CTS material.

Interestingly, a sharp increase in σ is clearly observed when x is increased from 0.1 (Pellet D) to 0.15 (Pellet E) as shown in Figure 2.19 (b). This suggests that the electronic transport properties of Zn-doped CTS are influenced not only by the Zn concentration but also by the crystalline structure. As discussed earlier, Pellet E and F have a phase pure ZB crystal structure, while Pellets B-D contain small amounts of residual WZ phase [Figure 2.12 (b)]. In general, the ZB compound is expected to have smaller effective masses, higher carrier mobility, and higher doping efficiency than its WZ counterpart, because of its highly symmetric cubic structure.[21] Therefore, the presence of the WZ phase in the pellet might create an adverse effect on σ. To confirm this hypothesis, the values σ of Pellets A (ZB CTS without the WZ phase) and B (ZB CTS with the WZ phase) were compared. As shown in Figure 2.19 (b), Pellet A showed a metallic behavior with higher σ, while Pellet B exhibited a semiconductor behavior with significantly low σ. This result clearly validates the hypothesis.

Unfortunately, it is unclear which is the main contributing factor for lowering of σ, the existence of interfaces between ZB (high σ) and WZ (low σ) phases or the existence of the WZ phase (low σ) itself, because it was difficult to fabricate a pellet which has a phase-pure WZ

structure. As shown in Figure 2.19 (d), the *ZT* values monotonically increase with temperature in all pellets and the highest *ZT* value of 0.37 at 670 K is achieved in both Pellets C ($Cu_2Sn_{0.95}Zn_{0.05}S_3$) and E ($Cu_2Sn_{0.85}Zn_{0.15}S_3$). In the case of non-nanostructured $Cu_2Sn_{1-x}Zn_xS_3$, the highest *ZT* value is reported to be 0.58 in the $x = 0.10$ sample at 723 K.[7] In this study, we set an upper temperature limit of 670 K for the thermoelectric property measurements to ensure that the pellets will not be chemically altered. Thus, if we compare the *ZT* values of Pellet C or E and non-nanostructured $Cu_2Sn_{1-x}Zn_xS_3$ ($x = 0.10$) at the same temperature, they are comparable.

2.5 Conclusions

In conclusion, the CTS system exhibits modest thermoelectric properties at relatively low temperature range. In theory, introducing nanograins into a CTS-based TE material in a controlled manner enables us to enhance its *ZT* value in comparison to the non-nanostructured counterpart by reducing lattice while maintaining *PF*. In addition, further enhancement of the *ZT* value can be achieved through doping of another element such as Zn in these materials. In this study, both strategies are employed to improve the *ZT* value. In particular, the chemically synthesized $Cu_2Sn_{1-x}Zn_xS_3$ ($x = 0 \sim 0.2$) NPs were pelletized by a pulse electric current sintering method. The highest *ZT* value of 0.37 at 670 K is achieved in both $Cu_2Sn_{0.95}Zn_{0.05}S_3$ and $Cu_2Sn_{0.85}Zn_{0.15}S_3$ nanostructured materials. However, this value was comparable to the *ZT* value at the same temperature of the $Cu_2Sn_{0.9}Zn_{0.1}S_3$ nonnanostructured material[7] presumably because the advantages and disadvantages of nanostructuring are balanced out in this case. Based on this, the further improvement of the *ZT* value by optimizing the size and shape of the NPs, blending two or more different types of NPs [e.g., ZB phase Zn-doped CTS and mixed-phase (ZB + WZ) Zn-doped CTS] for making a bulk material, and controlling mesoscale structures by tuning sintering conditions can be the future work.

References

(1) Ge, Z.-H.; Zhang, B.-P.; Chen, Y.-X.; Yu, Z.-X.; Liu, Y. and Li, J.-F. Synthesis and transport property of $Cu_{1.8}S$ as a promising thermoelectric compound. *Chem. Commun.* **2011,** *47*, 12697.

(2) Suekuni, K.; Tsuruta, K.; Kunii, M.; Nishiate, H.; Nishibori, E.; Maki, S.; Ohta, M.; Yamamoto, A. and Koyano, M. High-performance thermoelectric mineral $Cu_{12-x}Ni_xSb_4S_{13}$ tetrahedrite. *J. Appl. Phys.* **2013,** *113*, 043712.

(3) Suekuni, K.; Kim, F. S.; Nishiate, H.; Ohta, M.; Tanaka, H. I. and Takabatake, T. High-performance thermoelectric minerals: Colusites $Cu_{26}V_2M_6S_{32}$ (M = Ge, Sn). *Appl. Phys. Lett.* **2014**,*105*, 132107.

(4) Heo, J.; Laurita, G.; Muir, S.; Subramanian, M. A. and Keszler, D. A. Enhanced Thermoelectric Performance of Synthetic Tetrahedrites. *Chem. Mater.* **2014**, *26* (6), 2047-2051.

(5) Lu, X.; Morelli, D. T.; Xia, Y. and Ozolins, V. Increasing the Thermoelectric Figure of Merit of Tetrahedrites by Co-Doping with Nickel and Zinc. *Chem. Mater.* **2015**, *27* (2), 408-413.

(6) Bouyrie, Y.; Ohta, M.; Suekuni, K.; Kikuchi, Y.; Jood, P.; Yamamoto, A. and Takabatake, T. Enhancement in the thermoelectric performance of colusites $Cu_{26}A_2E_6S_{32}$ (A = Nb, Ta; E = Sn, Ge) using E-site non-stoichiometry. *J. Mater. Chem. C*. **2017**, *5*, 4174-4184.

(7) Shen, Y.; Li, C.; Huang, R.; Tian, R.; Ye, Y.; Pan, L.; Koumoto, K.; Zhang, R.; Wan, C. and Wang, Y. Eco-friendly *p*-type Cu_2SnS_3 thermoelectric material: crystal structure and transport properties. *Sci. Rep.* **2016**, ***6***, 32501.

(8) Tan, Q.; Sun, W.; Li, Z. and Li, J.-F. Enhanced thermoelectric properties of earth-abundant Cu_2SnS_3 via In doping effect. *J. Alloys Compd*. **2016**, *672*, 558.

(9) Zhao, H.; Xu, X.; Li, C.; Zhang, R.; Huang, R.; Lv, Y.; Li, D.; Hu, X.; Pan, L. and Wang, Y. Cobalt-doping in Cu_2SnS_3: enhanced thermoelectric performance by synergy of phase transition and band structure modification. *J. Mater. Chem. A.* **2017**, *5*, 23267.

(10) Biswas, K.; He, J.; Blum, I. D.; Wu, C.-I.; Hogan, T. P.; Seidman, D. N.; Dravid, V. P.; Kanatzidis, M. G. High-Performance Bulk Thermoelectrics with All-Scale Hierarchical Architectures. *Nature*. **2012**, *489*, 414-418.

(11) Yang, H.; Jauregui, L. A.; Zhang, G.; Chen, Y. P. and Wu, Y. Nontoxic and Abundant Copper Zinc Tin Sulfide Nanocrystals for Potential High-Temperature Thermoelectric Energy Harvesting. *Nano Lett.* **2012**, *12* (2), 540-545.

(12) Fernandes, P. A.; Salomé, P. M. P. and Cunha, A. F. D. A study of ternary Cu_2SnS_3 and Cu_3SnS_4 thin films prepared by sulfurizing stacked metal precursors. *J. Phys. D: Appl. Phys.* **2010**, *43*, 215403.

(13) Zhai, Y.-T.; Chen, S.; Yang, J.-H.; Xiang, H.-J.; Gong, X.-G.; Walsh, A.; Kang, J. and Wei, S.-H. Structural diversity and electronic properties of Cu_2SnX_3 (X=S, Se): A first-principles investigation. *Phys. Rev. B.* **2011**, *84*, 075213.

(14) Wang, S.; Gao, Q. and Wang, J. Thermodynamic Analysis of Decomposition of Thiourea and Thiourea Oxides. *J. Phys. Chem. B.* **2005**, *109*, 17281.

(15) Hall, E. H. On a New Action of the Magnet on Electric Currents. *Am. J. Math*. **1879**, *2* (3), 287-92.

(16) Lin, X.; Steigert, A.; Steiner, M. C. L.; Ennaoui, A. One step solution based synthesis and characterization ok kuramtie Cu_3SnS_4 nanocrystals, *RSC Adv*. **2012**, *2*, 9798-9800.

(17) Deng, M.; Shen, S.; Zhang, Y.; Xu, H.; Wang, Q. A generalized strategy for controlled synthesis of ternary metal sulfide nanocrystals. *New J. Chem.* **2014**, 38, 77-83.

(18) Park, Y.; Jin, H.; Park, J.; Kim, S. Simultaneous phase and size control in the synthesis of Cu_2SnS_3 and Cu_2ZnSnS_4 nanocrystals. *CrystEngComm*. **2014**, *16*, 8642-8645.

(19) Liang, Q. Phase-Controlled Synthesis of Cu_2SnS_3 Nanocrystals: The Effect of Redox Conditions on the Initial Binary $Cu_{2-x}S$ Nucleation. *Eur. J. Inorg. Chem*. **2016**, *2016*, 3634.

(20) Shannon, R. D. Revised effective ionic radii and systematic studies of interatomic distances in halides and chalcogenides. *Acta Crystallogr., Sect. A: Cryst. Phys., Diffr., Theor. Gen. Crystallogr.* **1976**, *32*, 751.

(21) Dalpian, G. M. and Wei, S.-H. Hole-Mediated Stabilization of Cubic GaN. *Phys. Rev. Lett.* **2004**, ***93***, 216401.

Chapter 3: Structure-Property Relations in Thermoelectric Nanobulk Materials Fabricated from Cu_2SnS_3 Nanoparticles

3.1 Introduction

With the global trend of development of copper sulfide-based sustainable thermoelectric (TE) materials,[1-10] researchers have revived interest in Cu_2SnS_3 (CTS), which had been well known as a solar cell material[11-15] along with the earth-abundant nature and low toxicity of their constituent elements. Moreover, CTS system exhibits modest TE properties at relatively low temperature range (< 200°C).[16] The low *ZT* (< 0.1) value of bulk CTS encourages researchers to devote to improve the TE properties of Cu_2SnS_3 based materials. For example, Zhao et al. reported a *ZT* of ~0.75 has been achieved in the Fe doped sample $Cu_2Sn_{0.85}Fe_{0.15}S_3$ at 723 K.[17] Xu et al. reported a relatively high *ZT* up to 0.56 in the $Cu_2Sn_{0.9}Ni_{0.1}S_3$ sample at 723 K.[18] Zhang et al. investigated the Mn doped CTS , a high *ZT* ~0.68 at 723 K was obtained.[19]

The challenges associated with increasing the overall *ZT* value can be observed in the figure of merit equation where σ must be maintained while κ is suppressed. Doping have been proved to be an effective method to improve the electrical conductivity. Multi-scale structuring has been regarded as one of the promising approaches to enhance the *ZT* value of a TE material, due to κ can be dramatically reduced through enhanced phonon scattering at grain boundaries because of the longer mean free path of phonons than that of mean grain size.[20]

With this in mind, in the previous chapter, we chemically synthesized uniform hole-doped CTS ($Cu_2Sn_{1-x}Zn_xS_3$) NPs and fabricated sustainable thermoelectric materials by sintering the NPs into dense bulk materials by PECS. Then, the structure and composition-property relationships in the $Cu_2Sn_{1-x}Zn_xS_3$ TE materials were analyzed. It was found that nanostructuring and Zn doping effect strategies could be successfully introduced to improve

the *ZT* values of CTS based materials. Furthermore, it is necessary to investigate the impact of grain size of CTS material on the final TE performance. Moreover, the impacts of grain size on TE properties of CTS have not been studied before, which encourage us to look insight in the relationship between structure and property of CTS material. This fundamental investigation will support the future application of this material.

In this chapter, three different sizes of CTS particles were synthesized by chemical methods as building blocks to form a bulk material controlling the nanoscale structure. Nanoscale and/or mesoscale structures could be controlled by changing the sintering conditions and the size and shape of particles that act as building blocks. The mean crystalline sizes of particles were varied from ~20 nm to ~60 nm without changes of crystal structure of material. Thereafter, the resulting particles were further pelletized into a nanobulk material by a pulse electric current sintering method. Finally, TE properties of the pelletized materials will be discussed in terms of composition and structure.

Many people supported the work in this chapter. I must say thanks to them. Firstly, Ms. Naoko Fujimoto of AIST supported the work for operating the ZEM-3 and LFA457 and Mr. Atsushi Yamamoto of AIST for supporting these measurements. Mr. Takida Hiroshi and Mr. Akatsuka Takeo in Nippon Shokubai Co., Ltd. also supported the work of pelletization. The author also thank Mr. Koichi Higashimine of JAIST for helping with STEM-HAADF measurements.

3.2 Experiments

3.2.1 Materials

The chemicals have been used for the fabrication of Cu-Sn-S NPs are shown in Table 3.1. All the chemicals were used without further purification.

Table 3.1. List of the chemicals, their chemical formula or abbreviation, and purity %.

Chemicals	Chemical Formula / Abbreviation	Purity %
Copper (II) nitrate hydrate	$Cu(NO_3)_2 \cdot xH_2O$	99.999
Copper (II) chloride	$CuCl_2$	99.9
Copper (I) chloride	CuCl	99.0
Tin (II) acetate	$Sn(CH_3CO_2)_2$ / $Sn(OAc)_2$	99.0
Tetraethylene glycol	$HO(CH_2CH_2O)_3CH_2CH_2OH$ / TEG	99.0
1-Dodecanethiol	$CH_3(CH_2)_{11}SH$ / DDT	>98
Oleylamine	$C_{18}H_{35}NH_2$ / OAM	70.0
1-Octadecene	$CH_3(CH_2)_{15}CH=CH_2$ / ODE	90.0
Thiourea	$SC(NH_2)_2$ / TU	99.0
Hexane	$CH_3(CH_2)_4CH_3$	96.0
Methanol	CH_3OH	99.8
Ethanol	C_2H_5OH	99.5
Toluene	$C_6H_5CH_3$	99.0

3.2.2 Synthesis of Small Size of Cu-Sn-S Nanoparticles

One pot chemical method was used to fabricate small size of NPs in this study. Compared to the synthesis scheme in section 2.2.2. The solvent Oleylamine (OAM) was replaced by tetraethylene glycol (TEG). Briefly, 4 mmol of copper(II) nitrate hydrate [$Cu(NO_3)_2$], 2 mmol of tin(II) acetate [$Sn(OAc)_2$], 100 mL of TEG and 80 mL of 1-dodecanthiol (DDT) were put into a 500-mL three-necked flask equipped with a dry Ar inlet/outlet, trap sphere, condenser, heating mantle, thermometer, and magnetic stirrer. First, the reaction mixture was stirred with Ar bubbling at room temperature for 5 min. Then the temperature was increased to 100 ºC and kept for 10 min with Ar bubbling to remove volatile matter. Subsequently, the reaction temperature was further raised to 260 ºC and kept for 1 h. After the reaction, the NPs were separated from the reaction mixture by centrifugation at 5000 rpm for 3 min. Then, the NPs were washed twice by repeating the following purification cycle: redispersion in hexane,

addition of ethanol, centrifugation, and supernatant removal. Finally, the NPs were dried in vacuum. The obtained NPs were used for subsequent characterization. The reaction scheme is shown in Figure 3.1.

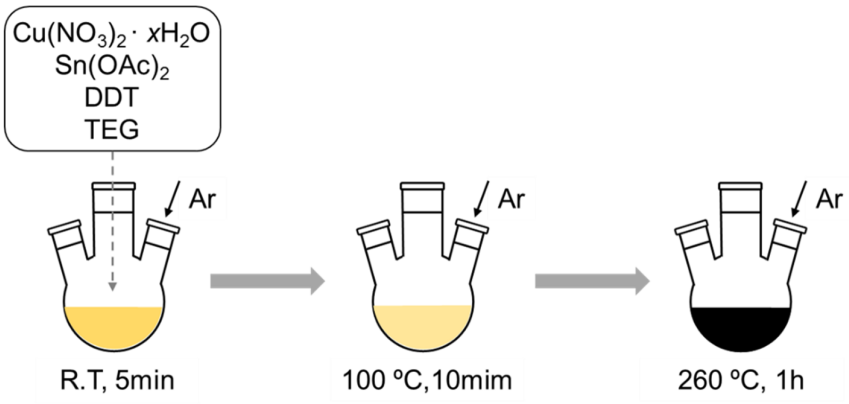

Figure 3.1. Synthetic scheme of small size Cu-Sn-S NPs system.

The input amount of chemicals are shown in the Table 3.2. In this study, the resulting NPs will be referred as Sample S, hereafter.

Table 3.2. Input amount of chemicals for the small size of Cu-Sn-S NPs system.

Sample	$Cu(NO_3)_2 \cdot xH_2O$ (mmol)	$Sn(OAc)_2$ (mmol)	DDT (mL)	TEG (mL)
Sample S	4	2	80	100

3.2.3 Synthesis of Middle Size of Cu-Sn-S Nanoparticles

Hot injection method was introduced to tune the size of NPs. The reaction scheme is shown in Figure 3.2. Briefly, 0.4 mmol of copper chloride ($CuCl_2$), 0.2 mmol of tin(II) acetate [$Sn(OAc)_2$], 6 mL of 1-octadecene (ODE) were put into a 50-mL three-necked flask equipped with a dry Ar inlet/outlet, trap sphere, condenser, heating mantle, thermometer, and magnetic stirrer. First, the reaction mixture was stirred with Ar bubbling at room temperature for 5 min. Then the temperature was increased to 100 ºC and kept for 30 min with Ar bubbling to remove

volatile matter. Subsequently, 3 mL of 1-dodecanthiol (DDT) were rapidly injected into the hot solution and the reaction temperature was further raised to 260 ºC and kept for 1 h. After the reaction, the NPs were separated from the reaction mixture by centrifugation at 5000 rpm for 3 min. Then, the NPs were washed twice by repeating the following purification cycle: redispersion in hexane, centrifugation, and supernatant removal. Finally, the NPs were dried in vacuum. The obtained NPs were used for subsequent characterization.

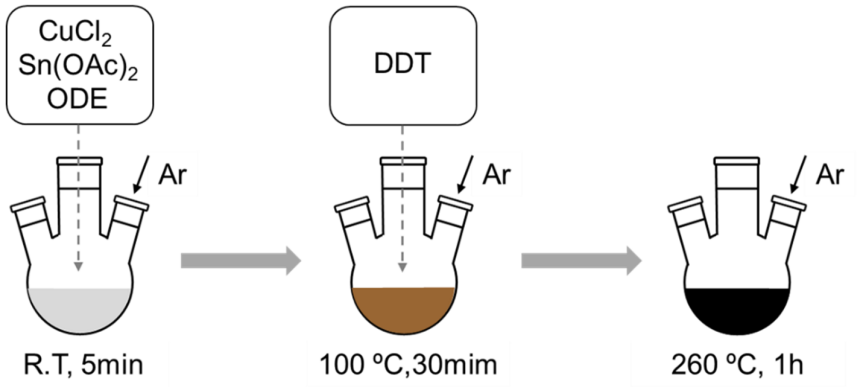

Figure 3.2. Synthetic scheme of middle size Cu-Sn-S NPs system.

The input amount of chemicals are shown in the Table 3.3. In this study, the obtained NPs will be referred as Sample M, hereafter.

Table 3.3. Input amount of chemicals for the middle size of Cu-Sn-S NPs system.

Sample	$CuCl_2$ (mmol)	$Sn(OAc)_2$ (mmol)	DDT (mL)	ODE (mL)
Sample M	0.4	0.2	3	6

3.2.4 Synthesis of Large Size of Cu-Sn-S Particles

Hot injection method was also chosen for tuning the size of particles in this research as shown in Figure 3.3. Briefly, 0.4 mmol of copper chloride (CuCl), 0.2 mmol of tin(II) acetate

[$Sn(OAc)_2$], 6 mL of 1-octadecene (ODE) were put into a 50-mL three-necked flask equipped with a dry Ar inlet/outlet, trap sphere, condenser, heating mantle, thermometer, and magnetic stirrer. First, the reaction mixture was stirred with Ar bubbling at room temperature for 5 min. Then the temperature was increased to 100 ºC and kept for 30 min with Ar bubbling to remove volatile matter. Subsequently, 3 mL of 1-dodecanthiol (DDT) were rapidly injected into the hot solution and the reaction temperature was further raised to 260 ºC and kept for 5 h. After the reaction, the particles were separated from the reaction mixture by centrifugation at 5000 rpm for 3 min. Then, the particles were washed twice by repeating the following purification cycle: redispersion in hexane, centrifugation, and supernatant removal. Finally, the particles were dried in vacuum. The obtained particles were used for subsequent characterization.

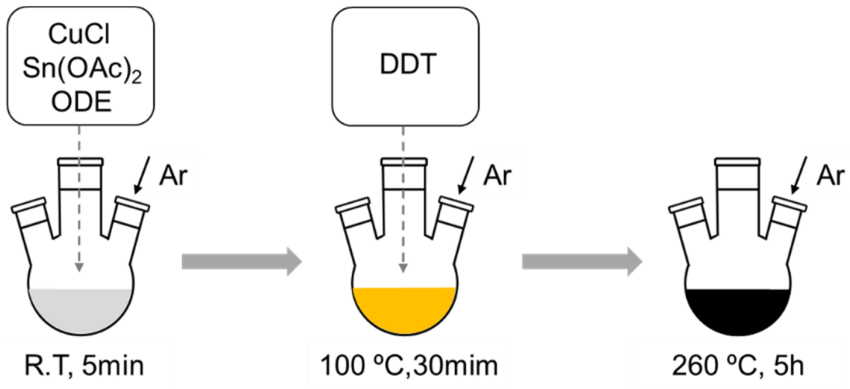

Figure 3.3. Synthetic scheme of large size Cu-Sn-S particles system.

The input amount of chemicals are shown in the Table 3.4. In this study, the obtained particles will be referred as Sample UL, hereafter.

Table 3.4. Input amount of chemicals for the large size of Cu-Sn-S NPs system.

Sample	**CuCl (mmol)**	**$Sn(OAc)_2$ (mmol)**	**DDT (mL)**	**ODE (mL)**
Sample UL	0.4	0.2	3	6

3.2.5 Ligand Exchange and Pelletization

The ligand exchange and palletization process for these three kinds' sizes of particles are the same as section 2.2.4 and section 2.2.5. After ligand exchange, the TU-capped Sample S, Sample M and Sample UL were then pelletized into solid disks. The diameters and thicknesses for these three pellets are around 10 mm and 2-3 mm, respectively. The sintering conditions of PECS machine for Sample M and Sample UL are: temperature: 450 ºC, pressure: 30 MPa, and sintering time: 5 min. However, the sintering temperature decreased to 400 ºC without changing other conditions for Sample S.

Pellets composed of Sample S, Sample M and Sample UL will be referred as Pellet S, Pellet M and Pellet UL respectively, hereafter.

3.3 Characterization Techniques

3.3.1 Structural Characterization

As-synthesized Sample S, Sample M and Sample UL were characterized by transmission electron microscopy (TEM, Hitachi H-7650), X-ray diffraction (XRD, Rigaku MiniFlex600 with Cu Ka) and scanning electron microscopy with energy dispersive spectroscopy (SEM-EDS, Miniscope TM3030Plus). Pellet S, Pellet M and Pellet UL were characterized by XRD, SEM-EDS and a scanning TEM (STEM) equipped with a high-angle annular dark-field (HAADF) detector and energy dispersive X-ray spectroscopy (EDS) elemental mapping. STEM-HAADF imaging and EDS elemental mapping were performed on a JEOL JEM-ARM200F microscope operated at 200 kV with a spherical aberration corrector and a nominal resolution of 0.8 A˚. The specimens for the cross-sectional STEM analyses were prepared by a focused-ion beam (FIB) method.

3.3.2 Thermoelectric Properties Measurements

The pellets used for the measurements are solid disks with diameter of 10 mm and thickness of 2-3 mm whose surfaces were coated by graphite spray. First, κ was measured for the pellet in the cross-plane direction by laser flash analysis (Netzsch LFA457). In this method, κ ($W \cdot m^{-1} \cdot K^{-1}$) was calculated as $\kappa = dcD$ where d ($kg \cdot m^{-3}$), c ($J \cdot kg^{-1} \cdot K^{-1}$) and D ($m^2 \cdot s^{-1}$) are density, specific heat and thermal diffusivity of the pellet, respectively. The densities of pellets were determined using a gas pycnometer (Shimadzu AccuPyc II 1340).

After thermal conductivity measurement, the solid disks were cut to bars approximately 2 mm × 2 mm × 8 mm. Then S and σ were measured in the inplane direction by ZEM-3 (ULVAC-Riko, Japan). Carrier thermal conductivity (κ_{car}) was calculated by Wiedemann-Franz's law $\kappa_{car} = L\sigma T$, where L denotes the Lorenz number (2.44×10^{-8} $W \cdot \Omega \cdot K^{-2}$). Then κ_{lat} was calculated as $\kappa_{lat} = \kappa - \kappa_{car}$. PF and ZT value were calculated as $PF = \sigma S^2$ and $ZT = \sigma S^2 T/\kappa$, respectively. The relative uncertainty of κ was estimated to be smaller than 8% based on the uncertainties of d, c and D. The relative uncertainty of S and σ were estimated to be 5%. The ZT values were calculated with those uncertainties in mind.

3.3.3 Hall Measurement

After the thermoelectric measurements, all the three pellets were polished to thin blocks approximately 4 mm × 2 mm × 0.5 mm by using sand paper. The electrodes were bonded to the rectangular in-plane specimen using gold paste. Then hall measurement performed. The Hall voltage V_H was measured at 300 K using a physical properties measurement system (PPMS; Quantum Design) by applying a magnetic field of ±5 T with an AC current. The AC current applied for these three samples were 1mA, 10mA and 10mA, respectively.

The Hall coefficient R_H was calculated as $R_H = V_H d/BI$, where V_H, d, B and I are the Hall voltage, the thickness of specimen, external magnetic field and current, respectively. Assuming single carrier transport, carrier concentration n and Hall mobility μ were calculated as $n = 1/|R_H|e$ and $\mu = R_H\sigma$, where e is elementary charge.

3.4 Results and Discussion

3.4.1 Morphology and Crystal Structure

Figure 3.4 shows the TEM images of as synthesized Sample S, Sample M and Sample UL nanoparticles. Samples S, M nanoparticles are uniform in size with a hexagonal pencil-like morphology (some nanoparticles are standing up and others are lying down on the TEM grid). The average length and width of Sample S were calculated to be 17 ± 1.5 nm and 11 ± 2 nm, respectively. The average length and width of Sample M were also calculated to be 28 ± 4 nm and 19 ± 2 nm, respectively. It is clearly to see that the average length and width of Sample UL are larger than 100 nm, but the size and shape of particles are uniform. The relationship between sizes and samples as shown in Figure 3.4 (d). These results indicated that we successfully obtained different size of particles.

The reasons why we could obtain different sizes of particles is due to the advantage of chemical method. As we mentioned before, compared to the synthesis reaction of Sample B in section 2.2.2, the solvent of OAM was changed to TEG for synthesizing Sample S. It is well known that the TEG has strong reducing property. In the reaction of Sample S, the strong reducing environment in the solution could lead to the rapid nucleation rate followed by slow growth of particles. Moreover, the incompatibility between TEG and DDT could result in the nucleation occurred near the interface under vigorous stirring. As a result, smaller NPs could be obtained by changing OAM to TEG.

However, it is difficult to tune the size and phase by using one pot chemical method at the same time. Hot injection method is usually preferred for nanoparticle synthesis due to its greater controlling over size, composition and phase.[22] Kept this in mind, this method was proceed to tune the size of NPs. To synthesize CTS compound by using this method, copper and tin source were mixed into ODE solvent at the beginning and sulfur source (DDT) was injected at certain time and temperature (100 ºC). The reaction mechanism has been studied in

depth by many researchers.[23-24] In this reaction, the first step involved the nucleation of Cu_xS nanoparticles, followed by the diffusion of Sn^{4+} into Cu_xS nanoparticles to form CTS nanoparticles. The reactivity of metal precursor has influence on the formation of CTS particles. In the reaction of Sample M, $CuCl_2$ used as copper precursor, Cu^{2+} is readily reduced to Cu^+ by DDT due to its low reduction potential of +0.159 V.[25-27] DDT easily chelates Cu^+ to form stable Cu^+-DDT complexes, while Sn^{2+} can be slowly oxidized to Sn^{4+} by Cu^{2+} ion. Thus, the nucleation rate of Cu_xS is slower than the reaction of Sample UL that use CuCl as copper source, while the diffusion rate of Sn^{4+} is faster. It has been studied that the diffusion of Sn^{4+} into Cu_xS seeds that also results in the growth of Cu_xS/CTS nanoparticles.[28] Meanwhile, longer reaction time (5h) was proceed in the synthesis of Sample UL that resulted in larger CTS particles.

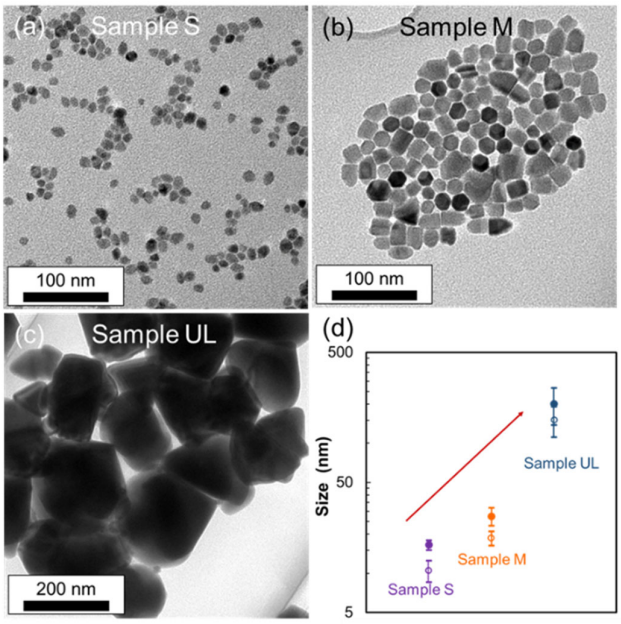

Figure 3.4. TEM images of (a) Sample S, (b) Sample M, (c) Sample UL particles, (d) The plot of lengths (closed circle) and widths (open circle) of particles. The purple color, orange color and dark blue color represent Sample S, Sample M and Sample UL, respectively.

The crystal structures of Samples S, Sample M, Sample UL, Pellet S, Pellet M and Pellet UL were also characterized and have been shown in Figure 3.5 (a) and (b). As shown in Figure 3.5

(a), it is obvious to see that the primary crystal phase of Samples S, Sample M and Sample UL are mixture phase of ZB and WZ phase (the reference XRD patterns of WZ and ZB CTS were taken from Ref.29. The primary crystal phase of Pellet UL is ZB with residue WZ phase while the primary phase of Pellet S and Pellet M have nearly pure ZB phase as shown in Figure 3.5 (b). Specifically, the phase transition from WZ to ZB is clearly seen for Pellet S and M. The reason why only Pellet S and M could obtain a phase-pure ZB structure is possibly due to the high surface energy of small size of NPs acts as building blocks in Pellet S and M. It is well known that WZ is metastable phase, while ZB structure has high symmetry which is more stable. Pellet S and Pellet M has high possibly tune to ZB structure under the sintering conditions with high sintering temperature and pressure.

The mean crystalline sizes (D_{xrd}) of Samples S, Sample M, Sample UL, Pellet S, Pellet M and Pellet UL were estimated using Scherrer's equation as shown in Table 3.5 for the first three intense diffraction peaks. As a result, the most intense diffraction peak of the primary phase were chosen for comparison. The values of D_{xrd} of Sample S, Sample M and Sample UL were determined to be 8.2, 18.1 and 37.7 nm, respectively. On the other hand, the values of D_{xrd} for Pellet S, Pellet M and Pellet UL were calculated to be 28.6, 39.3 and 47.2 nm, respectively. These results indicating that the mean crystalline sizes increased in all the Pellets.

The reason why the mean crystalline sizes increased a lot in Pellet S and Pellet M is due to the bigger specific surface area and higher surface energy of small NPs that act as build block lead to them easily aggregated to each other. When look backward the sintering conditions, it was found that the sintering conditions for Sample S and M were the same except the sintering temperature is lower than Sample UL. Even though the lower sintering temperatures (400 ºC) were used for Sample S and Sample M, the mean crystalline size still increased around 20 nm in Pellet S and Pellet M; it suggested that the current sintering condition could not maintain the mean crystalline size for Sample S and Sample M. It means that the current sintering conditions

are not the optimized. In order to maintain mean crystalline sizes after sintering for Pellet S and Pellet M, it is better to decrease the sintering temperature or/and reduce the sintering time.

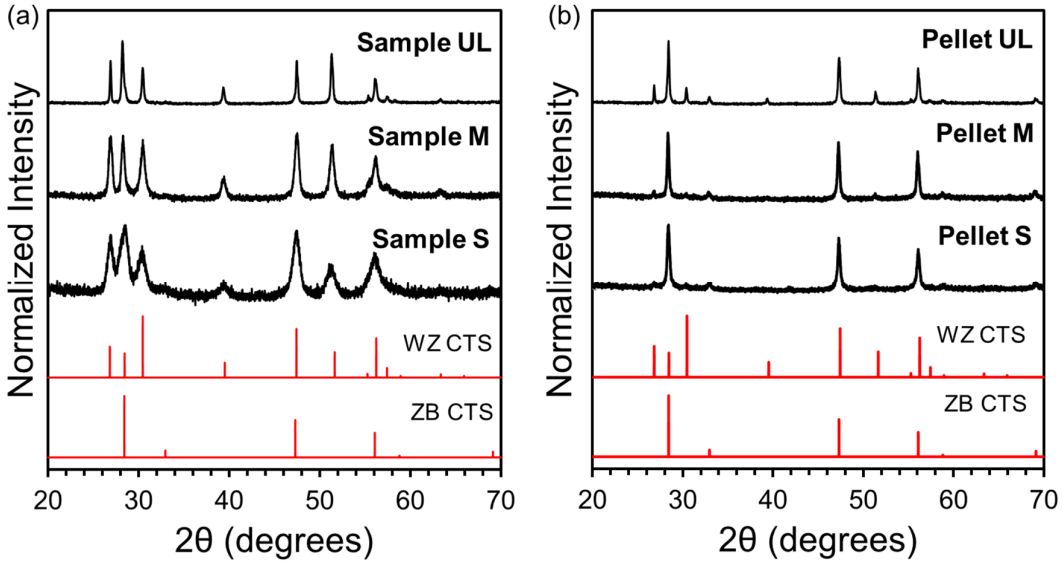

Figure 3.5. XRD patterns of (a) Samples S, Sample M and Sample UL and (b) Pellet S, Pellet M and Pellet UL. The reference XRD patterns of WZ and ZB CTS are also shown for comparison.[29]

Table 3.5. Summary of mean crystalline size (nm) of Particles and Pellets.

Sample		**Peak 1** ($2\theta = \sim 26.9^{o}$)	**Peak 2** ($2\theta = \sim 28.4^{o}$)	**Peak 3** ($2\theta = \sim 30.5^{o}$)
Sample S	NPs	13.4	8.2	9.2
	Pellet	N/A	28.6	N/A
Sample M	NPs	19.7	18.1	14.0
	Pellet	N/A	39.3	N/A
Sample UL	Particles	58.1	37.7	40.1
	Pellet	66.4	47.2	50.6

The densities of Pellets were determined to be 4.35, 4.47 and 4.62 g/cm^3, respectively, using a gas pycnometer (Shimadzu AccuPyc II 1340). Because the density of monocrystalline ZB CTS is 4.73 g/cm^3, the relative densities of all the Pellets were calculated to be 92 ~ 97%. The results are shown in the Table 3.6 indicating that we obtained high-density pellets.

Table 3.6. The Density and Relative density of Pellet S, Pellet M and Pellet UL.

Sample	Density (g/cm^3)	Relative Density (%)
Sample S	4.35	92
Sample M	4.47	94
Sample UL	4.62	97

3.4.2 STEM-HAADF and Compositional Analysis of Pellets

In order to check the homogeneity, all the pellets were choose for cross-sectional STEM-HAADF and EDS elemental mapping measurement. The images are shown in Figure 3.6. The contrast of the STEM-HAADF image is relatively uniform in all cases even though some dark areas were observed, which suggested the formation of homogeneous pellets was successful. The EDS elemental mapping images also confirm that the pellets are compositionally uniform. However, it is obvious to see that some big dark areas observed in the Figure 3.6 (a) due to the porosity generated in Pellet S during the sintering that might affect the electronic transport. The porosity in the pellets need to be further reduced by fine-tuning of the sintering conditions. Therefore, it is a big challenge for optimizing the sintering conditions to prevent grain growth while reducing porosity in pellet.

The compositions of pellets were also measured by using scanning electron microscopy with energy dispersive spectroscopy (SEM-EDS). The results are shown in Table 3.7. The average Cu:Sn:S atomic ratios of Pellet S, Pellet M and Pellet UL were determined to be 38:17:45, 37:17:46 and 39:16:45, respectively. Based on the results, the ratios of Sn and Cu for Pellet S, Pellet M and Pellet UL were determined to be 0.447, 0.459 and 0.410 respectively. Compared to the theory ratio of Sn to Cu in Cu_2SnS_3 (0.5), which shown Sn poor in these pellets. The composition difference might have effect on the final TE properties.

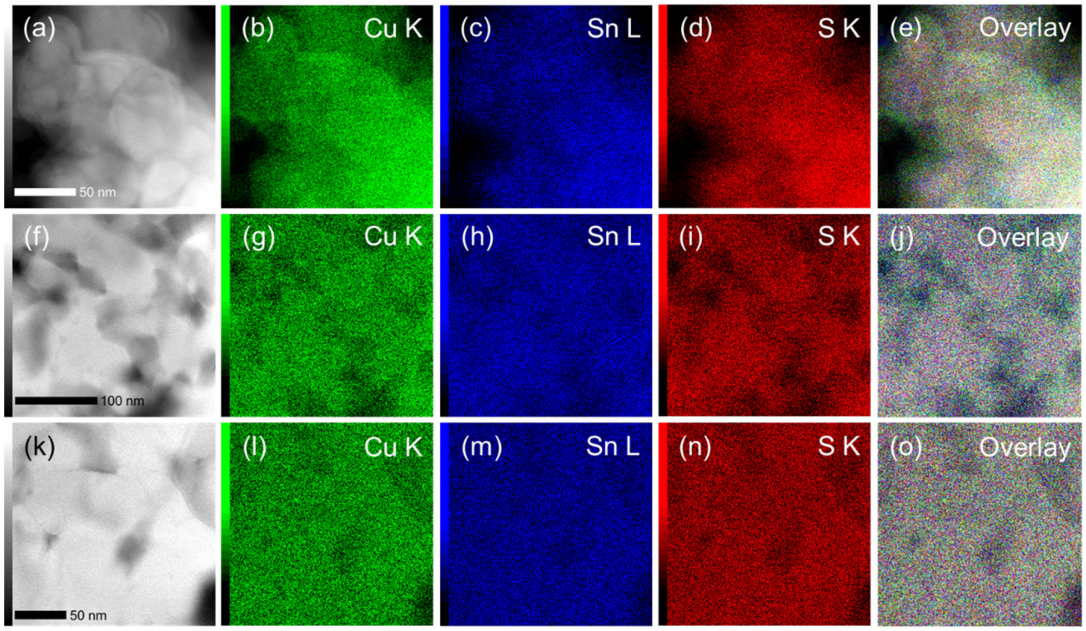

Figure 3.6. Cross-sectional STEM-HAADF and EDS elemental mapping images of (a-e) Pellet S, (f-i) Pellet M, (k-o) Pellet UL. (a, f, k) STEM-HAADF images. (b, g, l) Cu K edge, (c, h, m) Sn L edge, (d, i, n) S K edge, (e, j, o) overlay.

Table 3.7. The measured SEM-EDS compositions of Pellet S, M and UL.

	SEM-EDS		
	Cu (at %)	**Sn (at%)**	**S (at%)**
Pellet S	38	17	45
Pellet M	37	17	46
Pellet UL	39	16	45

3.4.3 Grain Size Effect on Thermal Conductivity

To get better understanding of the relationship between grain size and thermal conductivity, the thermal conductivities of Pellet S, Pellet M and Pellet UL have been measured. Firstly, the total thermal conductivities were measured and then the lattice thermal conductivities (κ_{lat}) were calculated as $\kappa_{lat} = \kappa - \kappa_{car}$. The carrier thermal conductivity (κ_{car}) was calculated by

Wiedemann-Franz's law $\kappa_{car} = L\sigma T$ where L and σ denote the electrical conductivity and the Lorenz number (2.44×10^{-8} $W\cdot\Omega\cdot K^{-2}$), respectively. Figure 3.7 shows the total thermal conductivities κ and lattice thermal conductivities κ_{lat} of Pellet S, Pellet M and Pellet UL. For comparison, the data of thermal conductivity and lattice thermal conductivity of non-nanostructured monoclinic CTS were taken from Ref. 16 as shown in Figure 3.7. It is obvious to see that all the pellets in this study have lower lattice thermal conductivities than the non-nanostructured monoclinic CTS. It suggests that the phonon scattering is successfully facilitated by nanostructuring.

Pellet M and Pellet UL shown higher κ_{lat} than Pellet S that is due to their larger grain sizes, as shown in Table 3.5. The average grain sizes for Pellet S, Pellet M and Pellet UL were calculated to be 28.6, 39.3 and 47.2 nm, respectively. Meanwhile, the average grain sizes of Pellet S is less than 30 nm and it has the lowest κ_{lat} near to theoretical minimum (0.3 $W\cdot m^{-1}\cdot K^{-1}$) for Cu-Sn-S systems at high temperatures.[30] It indicates that when the average grain size reduced to around 30 nm could strongly enhance phonon scattering at grain boundaries in CTS material result in low κ_{lat}. Moreover, the average grain sizes in Pellet M and Pellet UL are 39.3 nm and 47.2 nm, respectively. Both of them have larger κ_{lat} than Pellet S. It indicates that if the grain size is smaller, the κ_{lat} could be suppressed enough by phonon scattering at grain boundaries. Moreover, the nanograin boundaries exist in these pellets lead to enhanced phonon scattering result in low lattice thermal conductivities, which are still less than the non-nanostructured CTS material.

To get better understanding of the thermal transport behaviors, the inset of Figure 3.7 (b), where κ_{lat} of Pellet M, Pellet UL and non-nanostructured CTS exhibit the classical $1/T$ dependence, which caused by Umklapp scattering. While the characteristic $1/T$ dependence of κ_{lat} completely disappears in the case of Pellet S supporting the fact that the phonon scattering is dominated by defect scattering. This might be because the random distribution of vacancies

plays an important role in suppressing κ_{lat} possibly by thoroughly disrupting the normal phonon transport. The result is consistent with the STEM-HAADF observation of Pellet S.

In total, the grain size has huge effect on the thermal conductivity of CTS material. The lattice thermal conductivities decrease with grain size decrease, when the grainsize decrease to around 30nm, the lattice thermal conductivities could be strongly suppressed.

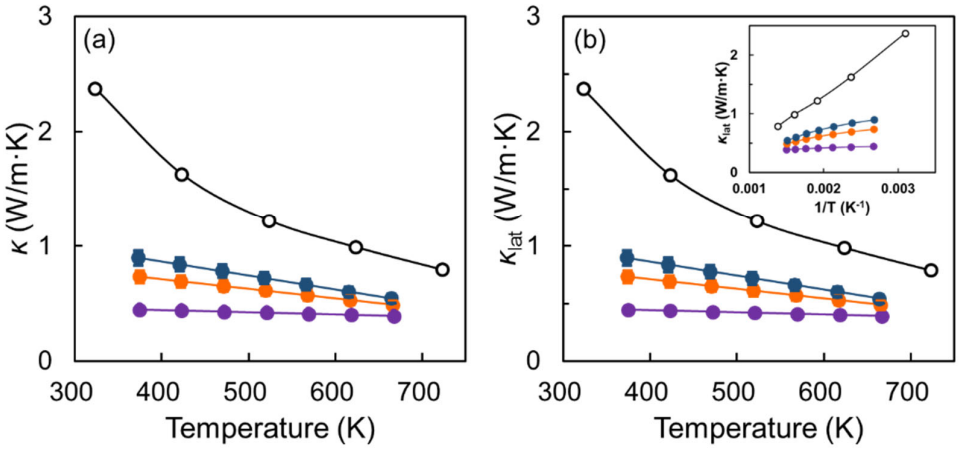

Figure 3.7. (a) Thermal diffusivity κ and (b) lattice thermal conductivity κ_{lat} of Pellet S, Pellet M and Pellet UL. Filled purple circles, filled orange circles and filled dark blue circles represent Pellet S, Pellet M and Pellet UL, respectively. The open circle represents the data of non-nanostructured monoclinic CTS taken from Ref.16. The inset of (b) shows lattice thermal conductivities of Pellet S, M, UL (filled purple, orange, dark blue circles) and non-nanostructured CTS (open circles) plotted with respect to the reciprocal of temperature.

3.4.4 Grain Size Effect on Electrical Transport Properties

In order to know well with the relationship between the structure and TE properties. S and σ in both heating and cooling cycles for all the pellets were measured. It was found that the values coincide in both cycles as shown in Figure 3.8. Therefore, the values only in the heating cycle for all the pellets are shown in Figure 3.9 for further discussion. The power factor (PF) and ZT value were calculated as $PF = \sigma S^2$ and $ZT = \sigma S^2 T/\kappa$, respectively.

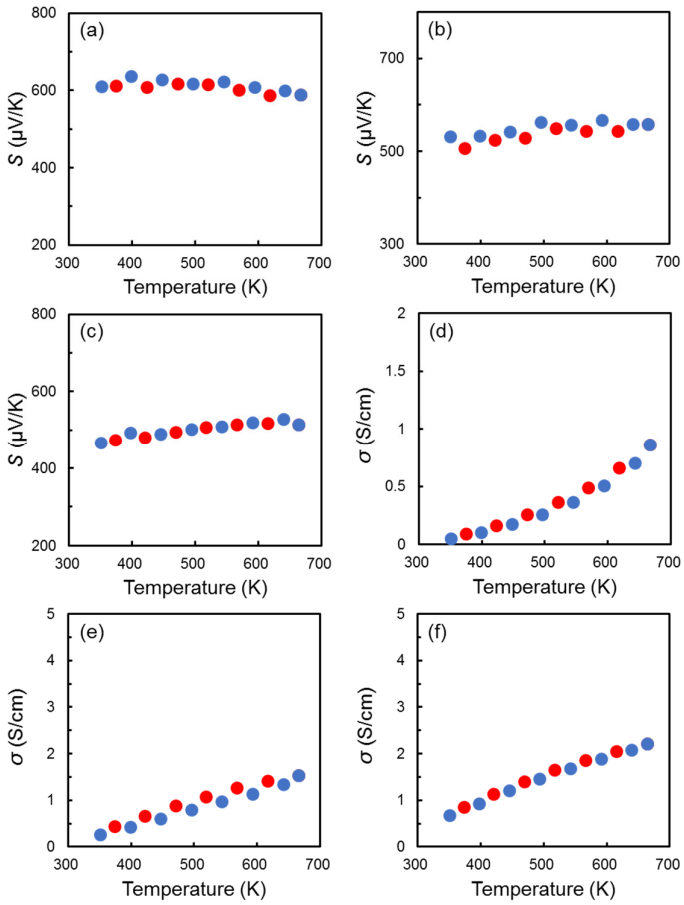

Figure 3.8. Seebeck coefficients of (a) Pellet S, (b) Pellet M, (c) Pellet UL. Electrical conductivities of (d) Pellet S, (e) Pellet M, (f) Pellet UL. Red and blue circles represent data measured in heating and cooling cycles, respectively.

As seen in Figure 3.9 (a), (b) and (c), the values of σ, S and PF of Pellet S, Pellet M and Pellet UL shown size dependence. The sign of S is positive in all cases, confirming p-type carrier transport in all pellets. With increasing grain size in pellets, a systematic increase in σ was observed [Figure 3.9 (b)], while S decreased in an opposite manner [Figure 3.9 (a)]. In addition, the values of σ for all pellets increase with increasing temperature indicating semiconductor behaviors. Interestingly, an increase in σ is clearly observed when the grain size is increased from 28.6 nm (Pellet S) to 47.2 nm (Pellet UL) as shown in Figure 3.9 (b). It seems like that the electronic transport properties of CTS were influenced by grain size. The small grain

boundaries not only has effect on reduction in the thermal transport but also has influence on deterioration in electron conduction. However, it is difficult to clarify the exact reason.

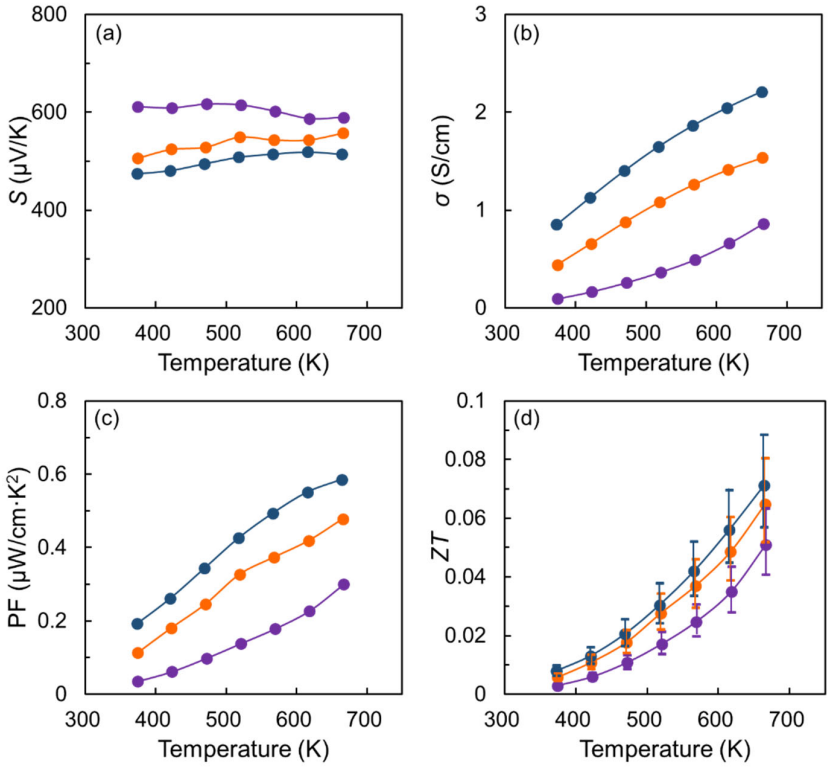

Figure 3.9. (a) Electrical conductivity σ, (b) Seebeck coefficient S, (c) power factor PF, (d) ZT with error bars of Pellet S, Pellet M and Pellet UL. Filled purple circles, filled orange circles and filled dark blue circles represent Pellet S, Pellet M and Pellet UL, respectively. It should be noted that we measured S and σ in both heating and cooling cycles and found that the values coincide in both cycles. Therefore, the values only in the heating cycle are shown here.

As discussed earlier, Pellets S and M have nearly phase pure ZB crystal structure, while Pellet UL contain small amounts of residual WZ phase [Figure 3.5 (b)]. In general, the ZB compound is expected to have smaller effective masses and higher carrier mobility than its WZ counterpart because of its highly symmetric cubic structure.[16] Therefore, the presence of the WZ phase in the pellet was expected to create an adverse effect on σ. However, the value σ of Pellet UL (ZB CTS with the WZ phase) is higher than that of Pellet S and M (nearly pure ZB phase). Thus, the crystal structure effect might not be the main reason to effect the electrical transport in the

presence of the contradiction. In addition, based on the composition analysis, these three pellets all shown Sn poor as discussed in section 3.4.2.

To look insight of the electrical transport properties, Hall Effect measurement were performed on Pellet S, M and UL at room temperature.

Table 3.8. *S, σ, n* and *μ* (at room temperature) of Pellet S, Pellet M and Pellet UL.

	S **(μV·K^{-1})**	***σ*** **(S·cm^{-1})**	***n*** **(cm^{-3})**	***μ*** **(cm^2·V^{-1}·s^{-1})**
Pellet S	602.9	0.1	1.76×10^{19}	0.03
Pellet M	499.4	0.3	2.02×10^{19}	0.09
Pellet UL	451.5	0.6	8.27×10^{18}	0.45

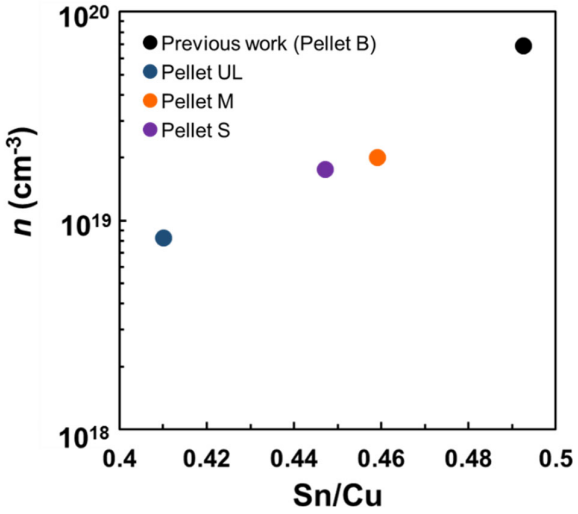

Figure 3.10. The relationship between carrier concentration and Sn/Cu compositional ratio of pellets. Filled purple circle, filled orange circle and filled dark blue circle represent Pellet S, Pellet M and Pellet UL, respectively. It should be noted that we took the data of Pellet B (filled black circle) in chapter 2 for comparison.

The values of *S*, *σ*, *n* and *μ* at room temperature of Pellet S, M and UL were shown in Table 3.8. In the case of Pellet UL, the value of *n* is less than both Pellet S and Pellet M. As we discussed in section 3.4.2, a higher degree of Sn vacancy was found in Pellet UL compared to

the other two pellets, which might be the main reason why Pellet UL has the lowest n. The plot of relationship between carrier concentration and the ratio of Sn/Cu is shown in Figure 3.10. The data of Pellet B in chapter 2 was taken for comparison. It can be seen that the ratio of Sn/Cu more close to the theory composition 0.5, the carrier concentration is higher. The ratio of Sn/Cu in Pellet UL is the lowest that lead to a lowest carrier concentration. These results suggested that the composition has big effect on the carrier concentration. However, Pellet UL shown the highest value of σ at room temperature, which might due to the highest carrier mobility as shown in Table 3.8.

As discussed earlier, the grain sizes of Pellet S and Pellet M are smaller than Pellet UL, thus the area of grain interface are expected to be larger, which might have an impact on the carrier transportation that strongly scatter carriers resulting in low carrier mobility. Moreover, the density of Pellet UL is higher than that of Pellet S and Pellet M as shown in Table 3.6, suggesting a lower porosity in Pellet UL, which is one of major sources of electron scattering. Keep this in mind, the lower porosity and the smaller grain interface can be the reasons of why the carrier mobility μ of Pellet S and Pellet M is lower than that of Pellet UL.

Unfortunately, it is difficult to clarify the main contributing factor for lowering of σ among the grain size effect, the crystal structure difference and the composition difference. Because it was difficult to precisely control over the grain size, structure and composition in pellet simultaneously under the current synthesis and sintering conditions. It is also highly possible that they work together to have a huge impact on the final performance. It was suggested that further optimization is required in the current synthesis and sintering conditions for all pellets. For example, increase the input amount of Sn precursor in the chemical synthesis of all pellets, optimize the sintering conditions of PECS for Pellet S and Pellet M to reduce the porosity and meanwhile maintain the grain size. Either step poses a huge challenge for future work.

Lastly, we present the calculated values of *PF* and *ZT* for all pellets in Figure 3.9(c) and (d).

The *ZT* values monotonically increase with temperature in all pellets and the highest *ZT* value of 0.07 at 670 K is achieved in Pellet UL as shown in Figure 3.9 (d). In the case of non-nanostructured CTS, the *ZT* value was reported to be 0.04. at 723 K.[16] In this study, we set an upper temperature limit of 670 K for the thermoelectric property measurements to ensure that the pellets will not be chemically altered. Thus, if we compare the *ZT* values of Pellet UL and non-nanostructured CTS at the same temperature, our pellet still shows better TE performance.

3.5 Conclusions

In conclusion, different sizes of CTS particles have been synthesized by using hot injection and one pot chemical method. XRD analysis for the as synthesized samples shows that the particles exhibit mixture of wurtzite and zincblend phases, proving that the size of CTS particles can be effectively controlled without changing the crystal structure by chemical methods. The resulting nanoparticles were pelletized by a PECS method. The sintering conditions used in this study for pellets preparation allows for the nanograins retained in the TE materials even though they need further optimization. Moreover, three kinds of grain size (28.6 nm, 39.3 nm, 47.2 nm) have been controllable fabricated in CTS pellets. Finally, the TE properties were measured for each sample and the relationship between grain size and TE performance was investigated. It shown that the lattice thermal conductivity could be effectively reduced compared to the non-nanostructured CTS material when the grain size in the pellet low to around 30 nm that resulted in enhanced phonon scattering at grain boundaries. In addition, it was found that the composition played an important role on the carrier concentration. Even though the main impact factor on the electrical transport property in these pellets is still unclear, the results in this study still provide information that how particles and pellets can be prepared to create TE materials with tunable grain sizes.

References

(1) Sun, S.-D.; Li, P.-G.; Liang, S.-H. and Yang, Z.-M. Diversified copper sulfide ($Cu_{2-x}S$) micro-/nanostructures: a comprehensive review on synthesis, modifications and applications. *Nanoscale*. **2017**, *9*, 11357-11404.

(2) Ge, Z.-H.; Zhang, B.-P.; Chen, Y.-X.; Yu, Z.-X.; Liu, Y.; Li, J.-F. Synthesis and transport property of $Cu_{1.8}S$ as a promising thermoelectric compound. *Chem. Commun.* **2011**, *47*, 12697.

(3) He, Y.; Day, T.; Zhang, T.; Liu, H.; Shi, X.; Chen, L.; Snyder, G. J. High thermoelectric performance in non-toxic earth-abundant copper sulfide. *Adv. Mater.* **2014**, *26*, 3974-3978.

(4) Ge, Z.-H.; Liu, X.; Feng, D.; Lin, J.; He, J. High-Performance Thermoelectricity in Nanostructured Earth-Abundant Copper Sulfides Bulk Materials. *Adv. Energy Mater.* **2016**, *6*, 1600607.

(5) Zhao, L.; Wang, X.; Fei, F. Y.; Wang, J.; Cheng, Z.; Dou, S.; Wang, J.; Snyder, G. J. High thermoelectric and mechanical performance in highly dense $Cu_{2-x}S$ bulks prepared by a melt-solidification technique. *J. Mater. Chem. A*. **2015**, *3*, 9432-9437.

(6) Mansour, B. A.; Soud, A. M. A. E.; Tahoon, K. H. Evaluation of Some Physical Quantities in the Two-Phase Region in Copper Sulphides. *Phys. Status Solidi A.* **1992**, *132*, 59-65.

(7) Chakrabarti, D. J.; Laughlin, D. E. The Cu-S (Copper-Sulfur) system. *Bull. Alloy Phase Diagrams.* **1983**, *4*, 254-271.

(8) Dennler, G.; Chmielowski, R.; Jacob, S.; F. Capet, F.; Roussel, P.; Zastrow, S.; Nielsch, K.; Opahle, I.; Madsen, G. K. H. Are Binary Copper Sulfides/Selenides Really New and Promising Thermoelectric Materials? *Adv. Energy Mater.* **2014**, *4*, 1301581.

(9) Hermite, E.; Cooper, C. F.; GB patent 2835, 1901.

(10) Sterzel, H. J.; patent WO 2006/089938 A1, 2006.

(11) Guan, P.-W.; Shang, S.-L.; Lindwall, G.; Anderson, T.; Liu, Z.-K. Phase stability of the Cu-Sn-S system and optimal growth conditions for earth-abundant Cu_2SnS_3 solar materials. *Sol. Energy*. **2017**, *155*, 745–757.

(12) Umehara, M.; Takeda, Y.; Tajima, S.; Motohiro, T.; Sakai, T. and Maekawa, R. Improvement of red light response of $Cu_2Sn_{1-x}Ge_xS_3$ solar cells by optimization of CdS buffer layers. *J. Appl. Phys.* **2015**, *118*, 154502.

(13) Ghorpade, U. V.; Suryawanshi, M.P.; Shin, S. W.; Kim, I.; Ahn, S. K.; Yun, J. H.; Jeong, C.; Kolekar, S. S. and Kim, J. H. Colloidal Wurtzite Cu_2SnS_3 (CTS) Nanocrystals and Their Applications in Solar Cells. *Chem. Mater*. **2016**, *28*, 3308-3317.

(14) Fiechter, S.; Martinez, M.; Schmidt, G.; Henrion, W.; Tomm, Y. Phase relations and optical properties of semiconducting ternary sulfides in the system Cu-Sn-S. *J. Phys. Chem. Solids*. **2003**, *64*, 1859-1862.

(15) Wu, J.; Gao, C.-H.; Han, L.; Shen, S.-S.; Jia, M.; Wang, L.; Jiang, L.-X.; Liu, F.-Y. The effect of different Cu/Sn ratios on the properties of monoclinic Cu_2SnS_3 thin flms and solar cells fabricated by the sol-gel method. *J. Mater. Sci.: Mater. Electron.* **2019**, *30*, 4378-4384.

(16) Shen, Y.; Li, C.; Huang, R.; Tian, R.; Ye, Y.; Pan, L.; Koumoto, K.; Zhang, R.; Wan, C. and Wang, Y. Eco-friendly *p*-type Cu_2SnS_3 thermoelectric material: crystal structure and transport properties. *Sci. Rep.* **2016**, ***6***, 32501.

(17) Zhao, L.; Pan, L.; Hu, X. H.; Lu, C. H. and Wang, Y. Magnetic iron doping in Cu_2SnS_3 ceramics for enhanced thermoelectric transport properties. *J. Appl. Phys.* **2019**,*125*, 095107.

(18) Xu, X.-X.; Zhao, H.-W.; Hu, X.-H.; Pan, L.; Chen, C. C.; Li, D.X.; Wang. Y. Synergistic role of Ni-doping in electrical and phonon transport properties of $Cu_2Sn_{1-x}Ni_xS_3$. *J. Alloys Compd*. **2017**, *728*, 701-708.

(19) Zhang, Z.; Zhao, H.-W.; Wang. Y.-F.; Hu, X.-H.; Lyu, Y.; Chen, C. C.; Pan, L.; Lu, C.-H. Role of crystal transformation on the enhanced thermoelectric performance in Mn-doped Cu_2SnS_3. *J. Alloys Compd*. **2019**, *780*, 618-625.

(20) Biswas, K.; He, J.; Blum, I. D.; Wu, C.-I.; Hogan, T. P.; Seidman, D. N.; Dravid, V. P.; Kanatzidis, M. G. High-Performance Bulk Thermoelectrics with All-Scale Hierarchical Architectures. *Nature.* **2012**, *489*, 414-418.

(21) Talapin, D.V.; Rogach, A.L.; Haase, M.; Weller, H. Evolution of an ensemble of nanoparticles in a colloidal solution: theoretical study. *J. Phys. Chem. B.* **2001**, *105*, 12278-12285.

(22) Kruszynska, M.; Parisia, J.; Kolny-Olesiaka, J. Synthesis and shape control of copper tin sulphide nanocrystals and formation of gold-copper tin sulphide hybrid nanostructures. *Z. Naturforsch.* **2014**, *69*a, 446-450.

(23) Yi, L.; Wang, D.; Gao, M. Synthesis of Cu_3SnS_4 nanocrystals and nanosheets by using $Cu_{31}S_{16}$ as seeds. *Chem. Eng. Commun.* **2012**, *14*, 401-404.

(24) Bard, A. J.; Parsons, R.; Jordan, J. *Standard Potentials in Aqueous Solution*; Taylor & Francis: New York, **1985**.

(25) Liu, Y.; Yao, D.; Shen, L.; Zhang, H.; Zhang, X.; Yang, B. Alkylthiol-Enabled Se Powder Dissolution in Oleylamine at Room Temperature for the Phosphine-Free Synthesis of Copper-Based Quaternary Selenide Nanocrystals. *J. Am. Chem. Soc.* **2012**, *134*, 7207.

(26) Bouroushian, M. *Electrochemistry of Metal Chalcogenides*; Springer: Berlin, Germany, **2010**.

(27) Tan, J. M. R.; Lee, Y. H.; Pedireddy, S.; Baikie, T.; Ling, X. Y. and Wong, L. H. Understanding the Synthetic Pathway of a Single-Phase Quarternary Semiconductor Using Surface-Enhanced Raman Scattering: A Case of Wurtzite Cu_2ZnSnS_4 Nanoparticles. *J. Am. Chem. Soc.* **2014**, *136*, 6684-6692.

(28) Liang, Q. Phase-Controlled Synthesis of Cu_2SnS_3 Nanocrystals: The Effect of Redox Conditions on the Initial Binary $Cu_{2-x}S$ Nucleation. *Eur. J. Inorg. Chem*. **2016**, *2016*, 3634.

(29) Xi, L.; Zhang, Y. B.; Shi, X. Y.; Yang, J.; Shi, X.; Chen, L. D. and W. Zhang. Chemical bonding, conductive network, and thermoelectric performance of the ternary semiconductors Cu_2SnX_3 (X= Se, S) from first principles. *Phys. Rev. B.* **2012**. *86*, 155201.

Chapter 4: Enhancement of the Thermoelectric Figure of Merit in Blended $Cu_2Sn_{1-x}Zn_xS_3$ Nanobulk Materials

4.1 Introduction

For energy harvesting applications, it has been a major challenge to enhance the *ZT* value of thermoelectric materials composed of earth abundant and low-toxic elements. Copper tin sulfide thermoelectric materials consist of eco-friendly and abundant elements and thus they have recently attracted much attention.[1-12] For example, Shen et al. have reported that Zn-doped CTS ($Cu_2Sn_{0.9}Zn_{0.1}S_3$) exhibited *ZT* = 0.58 at 723K.[7] Tan et al. have also reported In-doped CTS ($Cu_2Sn_{0.9}In_{0.1}S_3$) exhibited *ZT* = 0.56 at 773 K.[13] Zhao et al. have reported Co-doped CTS ($Cu_2Sn_{0.8}Co_{0.2}S_3$) exhibited *ZT* = 0.85 at 723 K.[14] Recently, we also reported that the *ZT* value of around 0.4 at 670K was achieved in a $Cu_2Sn_{1-x}Zn_xS_3$ nanostructured material created by pelletizing chemically synthesized $Cu_2Sn_{1-x}Zn_xS_3$ nanoparticles using a pulse electric current sintering (PECS) method.[15] This *ZT* value is 10 times higher than that of a non-nanostructured Cu_2SnS_3 bulk crystal thanks to effective phonon scattering by nanograins and the increase in hole carrier density by Zn doping.

In previous study, the nanostructuring effect, Zn doping effect and grain size effect have been systematically investigated, which could support the information for us to further improve the TE performance of CTS material. Based on the work in chapter 2, it also was found that the pellet of $Cu_2Sn_{0.85}Zn_{0.15}S_3$ exhibited metallic behavior with high electrical as well as thermal conductivities and its *ZT* value was 0.37 at 670 K, while the pellet of $Cu_2Sn_{0.9}Zn_{0.1}S_3$ exhibited semiconductor behavior with low electrical and thermal conductivities and its *ZT* value was 0.33 at 670 K. To enhance the *ZT* value, it has been reported that composite thermoelectric materials with nanoinclusions (or nanoprecipitates) are promising because they exhibit significantly reduced lattice thermal conductivity (κ_{lat}) while maintaining their electrical

transport properties. Na doped PbTe-PbS thermoelectric materials succeeded in effectively reducing κ_{lat}, while modifying the electronic structure to enhance thermoelectric power factor, because the Na-doped PbTe-PbS system is not only nanostructured but also exhibits PbS nanoprecipitates embedded throughout the PbTe matrix. As a result, 2 mol% Na-doped PbTe-PbS 12 mol% showed a maximum *ZT* value of 1.8 at 800 K.[16] Shortly afterwards, it was reported that 2 mol% Na-doped PbTe-SrTe 4 mol% exhibited a maximum *ZT* value of 2.2 at 915 K.[17] Meanwhile, PbS thermoelectric materials with 1.0 mol% Bi_2S_3 nanoinclusions and doped with 1.0 mol% $PbCl_2$ showed an enhanced *ZT* value of 1.1 at 923 K.[18] The inclusion of a small amount of the CaSe, SrSe and BaSe nanoprecipitates into a PbSe host material caused a reduction of κ_{lat} without significantly deteriorating the charge transport properties, and thus a high *ZT* value of 1.3 (at 923 K) was achieved.[19] It is also reported that n-type $PbTe_{1-x}I_{x-y}MgTe$ systems also exhibited a maximum *ZT* of 1.2 at 700 K.[20] There are a number of examples of successful enhancement of *ZT* value through the nanoinclusion approach including a ZnO nanobulk material with $ZnAl_2O_4$ nanoprecipitates,[21] $AgSb_{1-x}Sn_xTe_2$ with Ag_2Te nanoprecipitates,[22] SiGe with silicide ($FeSi_2$ or Mg_2Si) nanoinclusions,[23] and $Bi_2(Te,Se)_3$ with CuI nanoprecipitates.[24]

With this in mind, in this study, we fabricated blended $Cu_2Sn_{1-x}Zn_xS_3$ nanobulk materials by sintering a mixture of chemically synthesized $Cu_2Sn_{0.85}Zn_{0.15}S_3$ (high σ and high κ) and $Cu_2Sn_{0.9}Zn_{0.1}S_3$ (low σ and low κ) nanoparticles into dense bulk materials by PECS technique to further improve the *ZT* value of $Cu_2Sn_{1-x}Zn_xS_3$ nanobulk materials using $Cu_2Sn_{0.85}Zn_{0.15}S_3$ as a host material and $Cu_2Sn_{0.9}Zn_{0.1}S_3$ as nanoinclusions. By blending these two heterogeneous (but nearly identical) nanoparticles in a weight fraction of 9:1 for making a nanobulk material, the pellet showed *ZT* = 0.64 at 670 K, which is 1.7 and 1.9 times higher than the *ZT* values of the pristine $Cu_2Sn_{0.85}Zn_{0.15}S_3$ and $Cu_2Sn_{0.9}Zn_{0.1}S_3$ nanobulk materials, respectively.

The work in this chapter is one part of my Ph.D. research, which also has been published in an article. Ms. Naoko Fujimoto and Mr. Atsushi Yamamoto of AIST supported this work for operating and supporting the ZEM-3 and LFA457 measurements. This work also supported by researcher Mr. Takida Hiroshi and Mr. Akatsuka Takeo of Nippon Shokubai Co., Ltd for the pelletization. The author also thank Koichi Higashimine of JAIST for helping with STEM and SAED measurements and Prof. Mikio Koyano of JAIST for valuable discussion.

4.2 Experiments

4.2.1 Materials

The chemicals used for the fabrication of $Cu_2Sn_{1-x}Zn_xS_3$ samples is shown in Table 4.1. All the chemicals have been used as received without further purification.

Table 4.1. List of the chemicals, their chemical formula or abbreviation, and purity %.

Chemicals	Chemical Formula / Abbreviation	Purity %
Copper (II) nitrate hydrate	$Cu(NO_3)_2 \cdot xH_2O$	99.999
Tin (II) acetate	$Sn(CH_3CO_2)_2$ / $Sn(OAc)_2$	99.0
Zinc acetylacetonate hydrate	$Zn(C_5H_7O_2)_2 \cdot xH_2O$ / $Zn(acac)_2$	99.995
1-Dodecanethiol	$CH_3(CH_2)_{11}SH$ / DDT	>98
Oleylamine	$C_{18}H_{35}NH_2$ / OAM	70.0
Thiourea	$SC(NH_2)_2$ /TU	99.0
Hexane	$CH_3(CH_2)_4CH_3$	96.0
Methanol	CH_3OH	99.8
Ethanol	C_2H_5OH	99.5
Toluene	$C_6H_5CH_3$	99.0

4.2.2 Fabrication of $Cu_2Sn_{0.9}Zn_{0.1}S_3$ and $Cu_2Sn_{0.85}Zn_{0.15}S_3$ Nanoparticles

Hole-doped $Cu_2Sn_{0.9}Zn_{0.1}S_3$ and $Cu_2Sn_{0.85}Zn_{0.15}S_3$ NPs were synthesized in a similar manner as described in section 2.2 of chapter 2 by varying the input molar ratio of zinc(II)

acetylacetonate hydrate [$Zn(acac)_2$] to tin(II) acetate [$Sn(OAc)_2$] keeping the total amount of those two precursors constant [$Zn(acac)_2 + Sn(OAc)_2 = 2$ mmol]. The methods of synthesis, purification and ligand exchange were all the same as previously described in section 2.2.

4.2.3 Preparation of Blended Materials

Three kinds of blended materials were fabricated as described in the following text.

4.2.3.1 Mixing After the Ligand Exchange

The first kind of blended material. (1) After the ligand exchange, TU-capped $Cu_2Sn_{0.85}Zn_{0.15}S_3$ (hereafter referred to as Zn15-CTS) and TU-capped $Cu_2Sn_{0.9}Zn_{0.1}S_3$ (hereafter referred to as Zn10-CTS) nanoparticles were dispersed in methanol separately. Then, both nanoparticle dispersions were mixed in such a way that the weight ratio of Zn15-CTS to Zn10-CTS in blended nanoparticles was 9:1. After centrifugation, the resulting nanoparticles were dried in vacuum. The blended nanoparticles were then pelletized into a solid disk with a diameter of 10 mm and a thickness of 2-3 mm using a PECS machine under the following conditions: atmosphere, vacuum; temperature, 450 °C; pressure, 30 MPa; and sintering time, 5 min. The pellet is referred to as Pellet_9:1_ALE (ALE stands for "after the ligand exchange"). The general scheme for blending materials after the ligand exchange as shown in Figure 4.1.

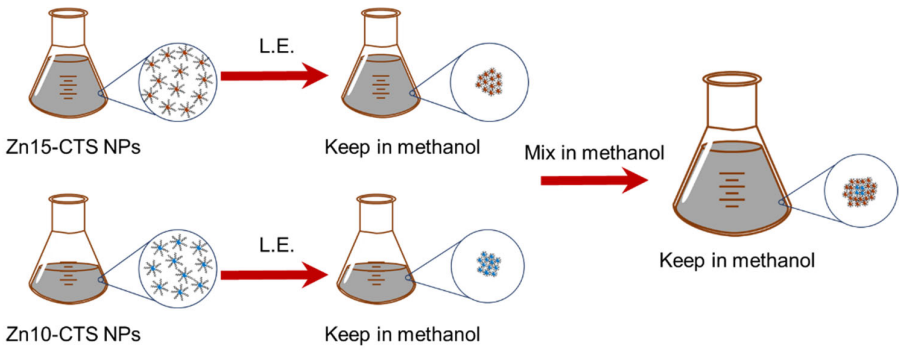

Figure 4.1. General synthetic scheme for blended materials after ligand exchange. ("L.E." denote ligand exchange).

The second kind of blended material. (2) After the ligand exchange, TU-capped Zn15-CTS and Zn10-CTS nanoparticles were dispersed in methanol separately. Then, both nanoparticle dispersions were mixed in such a way that the weight ratio of Zn15-CTS to Zn10-CTS in blended nanoparticles was 5:5. The blended nanoparticles were then pelletized into a solid disk with a diameter of 10 mm and a thickness of 2-3 mm under the same conditions as above. The pellet is referred to as Pellet_5:5_ALE.

4.2.3.2 Mixing Before the Ligand Exchange

The third kind of blended material. (2) Before the ligand exchange, DDT/OAM-capped Zn15-CTS and Zn10-CTS nanoparticles were dispersed in DDT separately. Then, both nanoparticle dispersions were mixed in such a way that the weight ratio of Zn15-CTS to Zn10-CTS in blended nanoparticles is 9:1. After mixing, the nanoparticles were washed and subjected to ligand exchange. The resulting nanoparticles were dried in vacuum. The blended nanoparticles were then pelletized into a solid disk with a diameter of 10 mm and a thickness of 2-3 mm using a PECS machine under the same conditions as above. The pellet is referred to as Pellet_9:1_BLE (BLE stands for "before the ligand exchange"). The general scheme for blending materials before the ligand exchange as shown in Figure 4.2.

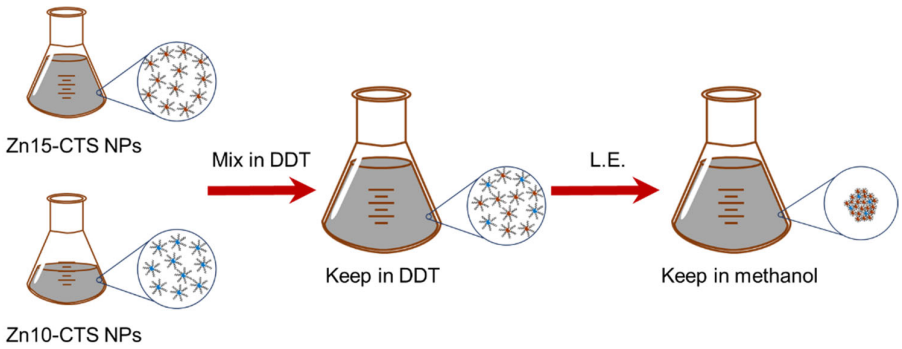

Figure 4.2. General synthetic scheme for blended materials before ligand exchange. ("L.E." denote ligand exchange).

For comparison, we show the data of the pristine Zn15-CTS and Zn10-CTS nanobulk materials, which are referred to as Pellet_10:0 and Pellet_0:10, respectively. The weight of Zn15-CTS and Zn10-CTS NPs in the blended materials are shown in the below Table 4.2.

Table 4.2. The weight of Zn15-CTS and Zn10-CTS in blended nanobulk materials.

Sample	Zn15-CTS (g)	Zn10-CTS (g)
Pellet_10/0	0.850	0
Pellet_9/1_ALE	0.765	0.085
Pellet_5/5_ALE	0.425	0.425
Pellet_9/1_BLE	0.085	0.765
Pellet_0/10	0	0.850

4.2.3.4 Dynamic Light Scattering (DLS) Analysis

Since the blended materials were mixed in liquid, it is necessary to know particle size and size distribution of particles in methanol and DDT. Here, dynamic light scattering (DLS) is used for this measurement. We redispersed the dried Zn15-CTS particles in methanol after ligand exchange and then have its average hydrodynamic particle size measured. In addition, this measurement was performed for the as synthesized Zn15-CTS NPs before ligand exchange when they were dispersed in DDT. For comparison, the concentration in both cases are 0.000465mg/mL. These two samples were chosen for DLS measurement as a reference.

Figure 4.3 shows the particle diameter and statistical size distribution of Zn15-CTS particles dispersed in methanol and DDT. It is clear that the size distribution of dried Zn15-CTS particles after ligand exchange (capped with TU) redispersed in methanol are not uniform indicating the existence of particle aggregation. Because of the aggregation, the measured particle size is in access of 238.2 nm. While in the other one, the size distribution is uniform with a smaller average hydrodynamic particle size of 151.6 nm. The size difference of particles in methanol

and DDT might lead to the structure difference of inclusions in blended materials. Scheme 4.1 illustrates the system in a comprehensible way including fabrication processes.

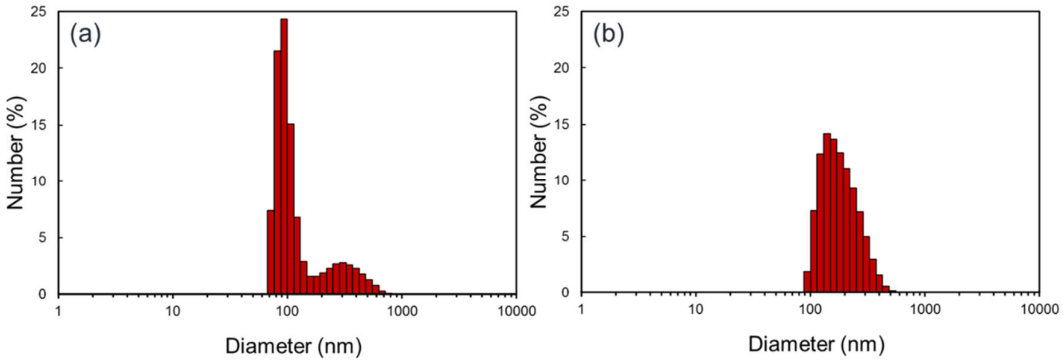

Figure 4.3. Particle diameter of (a) dried Zn15-CTS particles after ligand exchange redispersed in methanol and (b) as-synthesized Zn15-CTS NPs before ligand exchange dispersed in DDT by DLS.

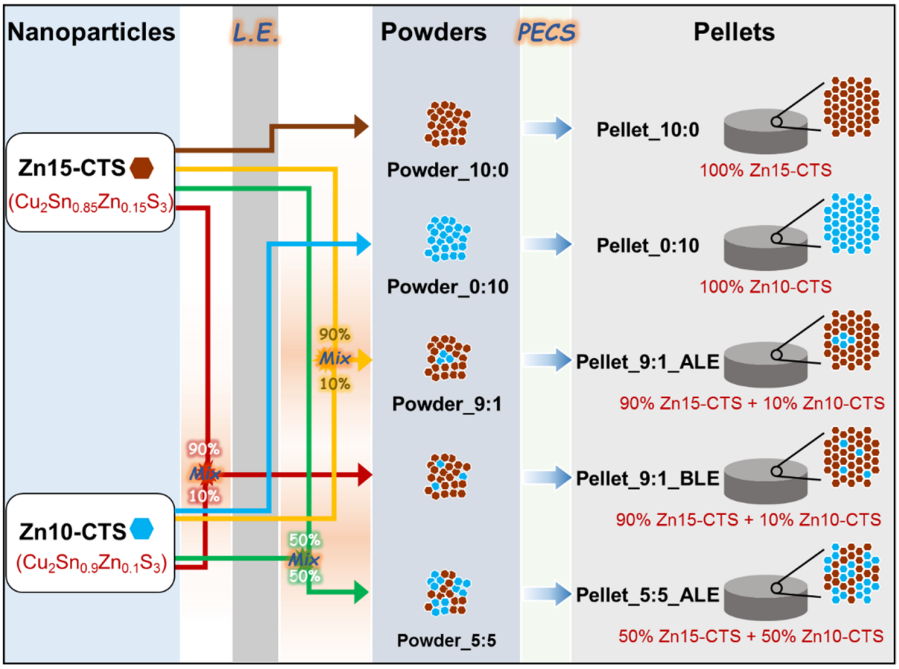

Scheme 4.1. Illustration of five different nanobulk materials in this study including fabrication methods ("L.E." and "PECS" denote ligand exchange and pulse electric current sintering, respectively).

4.3 Characterization Techniques

4.3.1 Structural Characterization

As-synthesized nanoparticles were characterized by transmission electron microscopy (TEM; Hitachi H-7650 operated at 100 kV), X-ray diffraction (XRD; Rigaku MiniFlex600 with Cu Kα), and inductively coupled plasma optical emission spectroscopy (ICP-OES; Shimadzu ICPS-7000). The pellets were characterized by high resolution TEM (HRTEM; Hitachi H-9000NAR operated at 300 kV), selected-area electron diffraction (SAED; using HRTEM), XRD, ICP-OES and a scanning TEM (STEM) equipped with a high-angle annular dark-field (HAADF) detector and energy-dispersive X-ray spectroscopy (EDS) elemental mapping (JEOL JEM-ARM200F operated at 200 kV). The specimens for the cross-sectional STEM analyses and SAED analyses were prepared with a focused-ion beam (FIB) method. The sample preparation by using this method can refer the section 2.3 in Chapter 2.

4.3.2 Thermal Conductivity Measurement

The samples used for thermal conductivity measurements are solid disks with a diameter of 10 mm and thickness of 2-3 mm whose surfaces were coated by graphite spray. First, κ was measured for the pellet in the cross-plane direction by laser flash analysis (Netzsch LFA457). In this method, κ ($W \cdot m^{-1} \cdot K^{-1}$) was calculated as $\kappa = dcD$ where d ($kg \cdot m^{-3}$), c ($J \cdot kg^{-1} \cdot K^{-1}$) and D ($m^2 \cdot s^{-1}$) are density, specific heat and thermal diffusivity of the pellet, respectively. The densities of pellets were determined using a gas pycnometer (Shimadzu AccuPyc II 1340). Carrier thermal conductivity (κ_{car}) was calculated by Wiedemann-Franz's law $\kappa_{car} = L\sigma T$, where L denotes the Lorenz number (2.44×10^{-8} $W \cdot \Omega \cdot K^{-2}$). Then κ_{lat} was calculated as $\kappa_{lat} = \kappa - \kappa_{car}$.

4.3.3 Electrical Transport Properties Measurements

After thermal conductivity measurement, all the solid disks were cut to bars approximately 2 mm × 2 mm × 8 mm. Then S and σ were measured in the inplane direction by ZEM-3 (ULVAC-Riko, Japan). The relative uncertainty of S and σ were estimated to be 5%. The ZT values were

calculated with those uncertainties in mind. *PF* and *ZT* values were calculated as $PF = \sigma S^2$ and $ZT = \sigma S^2 T/\kappa$, respectively.

Three small square disks [~2 (width) × ~2 (length) × ~0.5 (thickness) mm] were cut out of the bar-shaped specimen in pellet_9:1_ALE after the measurements of *S* and σ. The sample preparation are shown in Figure 4.4. The normal direction of two disks is parallel to that of the pellet (inplane specimens). On the contrary, the normal direction of the last disk is perpendicular to that of the pellet (cross-plane specimen). Then, small gold electrodes are attached at the four corners of the faces of both in-plane and cross-plane specimens as shown in Figure 4.4 (c). The electrical resistivity between two adjacent electrodes (ρ_{ij}) was measured using ResiTest8400 (Toyo Corp., Japan) based on Montgomery's method.[25]

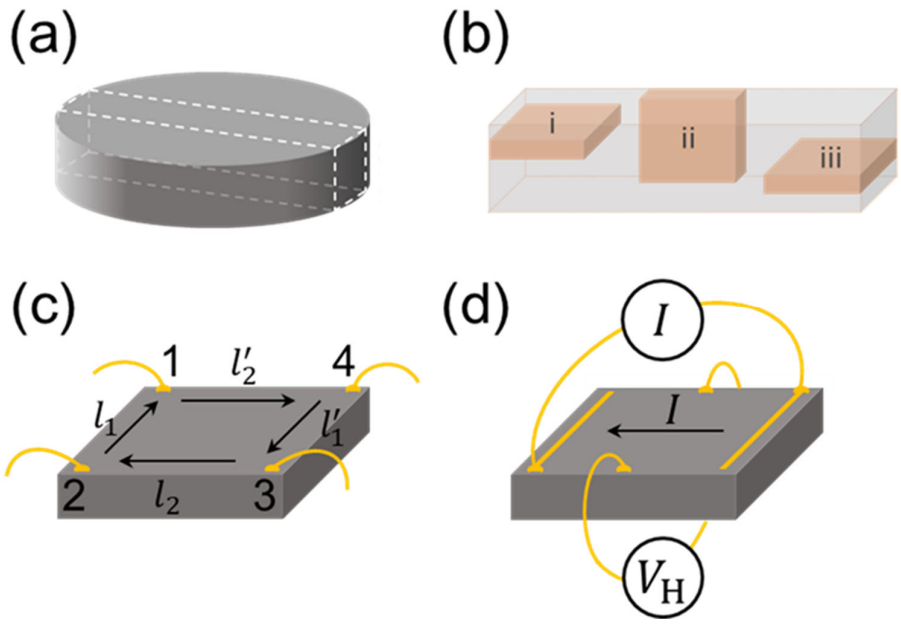

Figure 4.4. Circular disk-shaped pellet_9:1_ ALE (ϕ10 × 2.4 mm) for the measurement of κ. The region enclosed by white dashed lines is a bar-shaped specimen for the measurements of *S* and σ cut out of the circular disk-shaped pellet. (b) Three square disks were cut out of the bar-shaped specimen: (i) in- and (ii) cross-plane specimens for the electrical resistivity measurement and (iii) a rectangular in-plane specimen for the Hall measurement. Schematic illustrations of (c) electrical resistivity measurement based on Montgomery's method[25] and (d) Hall measurement.

All the three pellets were performed hall measurement. The Hall voltage V_H was measured between 10 and 300 K using a physical properties measurement system (PPMS; Quantum Design) by applying a magnetic field of ±5 T with an AC current (60 mA). The electrodes were bonded to the rectangular in-plane specimen using gold paste. Then, the Hall coefficient R_H was calculated as $R_H = V_H d/BI$, where d, B and I are the thickness of specimen, external magnetic field and current, respectively. Assuming single carrier transport, carrier concentration n and Hall mobility μ were calculated as $n = 1/|R_H|e$ and $\mu = R_H\sigma$, where e is the elementary charge.

4.4 Results and Discussion

4.4.1 Morphology and Crystal Structure

Figure 4.5 (a) and (b) show the TEM images of as synthesized Zn15-CTS and Zn10-CTS nanoparticles, respectively. Both nanoparticles are uniform in size with a hexagonal pencil-like morphology (some nanoparticles are standing up and others are lying down on the TEM grid). The average length and width of Zn15-CTS nanoparticles are calculated to be 40 ± 5 nm and 27 ± 2 nm, respectively. The average length and width of Zn10-CTS nanoparticles are also calculated to be 40 ± 4 nm and 25 ± 2 nm, respectively. The Cu:Sn:Zn atomic ratios of as-synthesized Zn15-CTS and Zn10-CTS nanoparticles were determined to be 63:31:6 and 65:31:4, respectively, by ICP-OES.

Figure 4.5 (c) shows the XRD patterns of the Zn15-CTS/Zn10-CTS blended nanoparticles in the weight ratio of 0/10, 10/0, 9/1 and 5/5 from bottom to top. These nanoparticle samples are referred to as Powder_0:10, Powder_10:0, Powder_9:1 and Powder_5:5, respectively. Figure 4.5 (d) shows the XRD patterns of Pellet_0:10, Pellet_10:0, Pellet_9:1_ALE and Pellet_5:5_ALE from bottom to top. The reference XRD patterns of zinc blende (ZB) and

wurtzite (WZ) Cu_2SnS_3 (CTS) were taken from Ref.26. As shown in Figure 4.5 (c), the primary crystal phase of all nanoparticle samples is WZ with small amounts of ZB phase. As shown in Figure 4.5 (d), the phase transition from WZ to ZB is clearly seen for all pellets. Specifically, Pellet_10:0 and Pellet_9:1_ALE have a nearly phase-pure ZB crystal structure, while Pellet_0:10 and Pellet_5:5_ALE contain small amounts of residual WZ phase. The reason why only Pellet_10:0 and Pellet_9:1_ALE could obtain a phase-pure ZB structure is possibly because the phase transition temperature decreased by increasing the Zn impurity concentration.

The mean crystalline sizes (D_{xrd}) were calculated using Scherrer's equation based on the most intense diffraction peak of the primary phase. The values of D_{xrd} for Powder_0:10, Powder_10:0, Powder_9:1 and Powder_5:5 are 20.0, 19.6, 20.9, 18.8 nm, respectively. Note that the values of D_{xrd} agree well with the average width of nanoparticles estimated from TEM images. The D_{xrd} values of Pellet_0:10, Pellet_10:0, Pellet_9:1_ALE and Pellet_5:5_ALE are calculated to be 18.2, 24.5, 30.4, 21.4 nm, respectively, indicating that D_{xrd} remains virtually unchanged during sintering for all pellets. The reason why D_{xrd} of Powder_0:10 slightly decreased after the sintering is due to the broadening of the primary peak of the ZB phase caused by the non-negligible amount of WZ residue.

The Cu:Sn:Zn atomic ratios of Pellet_0:10, Pellet_10:0, Pellet_9:1_ALE and Pellet_5:5_ALE were determined to be 65:31:4, 68:27:5, 64:30:6 and 65:30:5, respectively, by ICP-OES. The densities of Pellet_0:10, Pellet_10:0, Pellet_9:1_ALE and Pellet_5:5_ALE were measured to be 4.56, 4.50, 4.56 and 4.53 g/cm^3, respectively. Considering that the density of monocrystalline ZB CTS is 4.73 g/cm^3, the relative densities of all pellets were estimated to be 95%−97%.

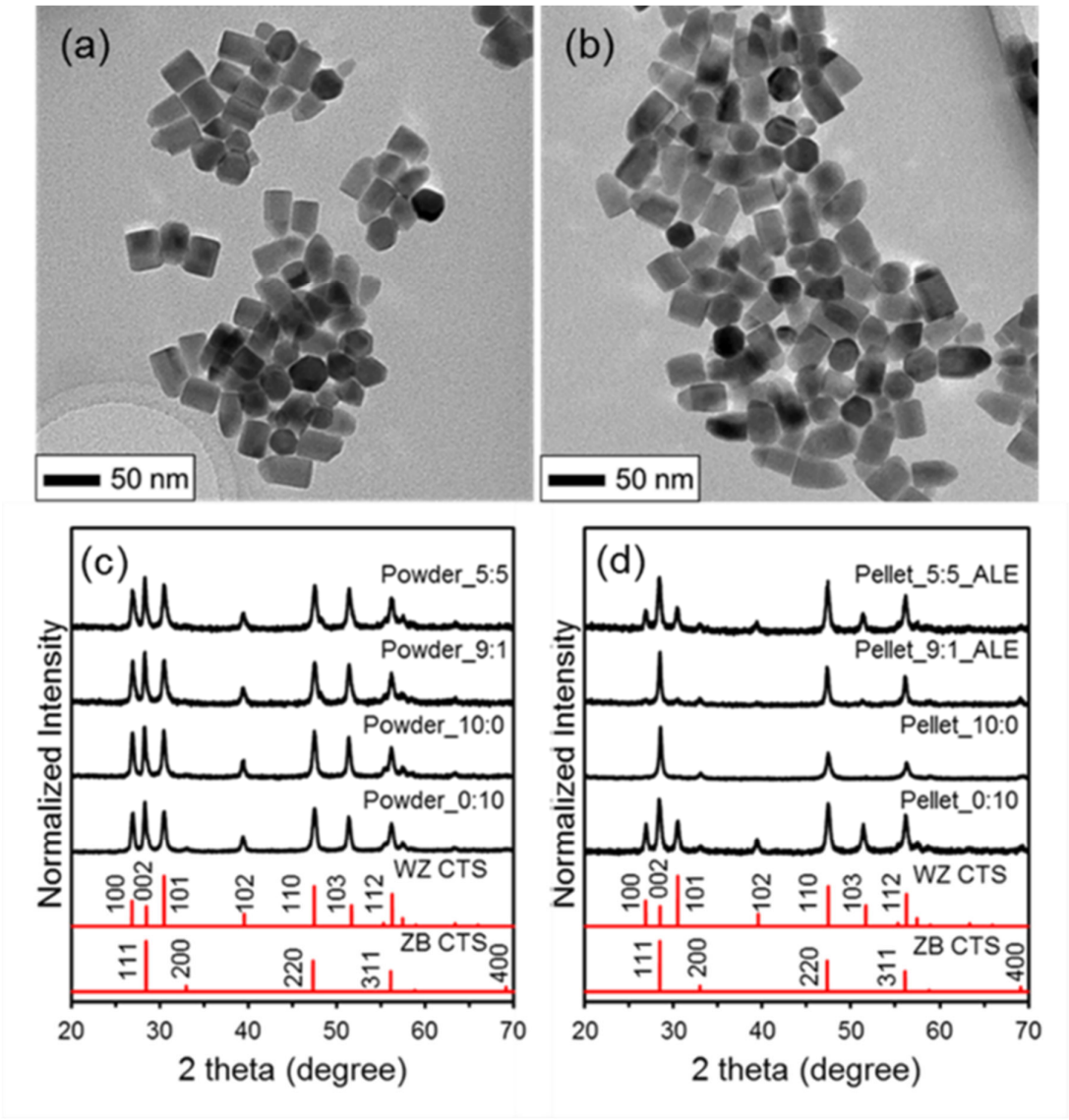

Figure 4.5. TEM images of (a) Zn15-CTS and (b) Zn10-CTS nanoparticles. (c) XRD patterns of nanoparticle samples (Powder_0:10, Powder_10:0, Powder_9:1 and Powder_5:5 from bottom to top). (d) XRD patterns of the pellets (Pellet_0:10, Pellet_10:0, Pellet_9:1_ALE and Pellet_5:5_ALE from bottom to top). The reference XRD patterns (red lines) of zinc blende (ZB) and wurtzite (WZ) Cu_2SnS_3 (CTS) were taken from Ref.26.

4.4.2 Thermoelectric Properties

We measured S and σ in both heating and cooling cycles for all the pellets and found that the values coincide in both cycles are shown in Figure 4.6 and Figure 4.7. Therefore, the values only in the heating cycle for all the pellets are shown in Figure 4.8 for further discussion.

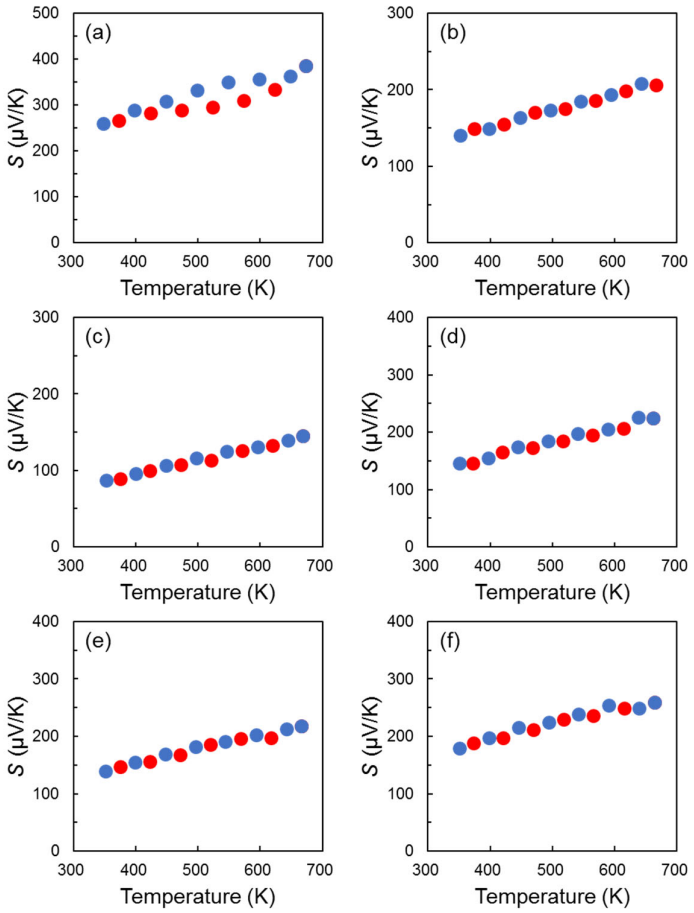

Figure 4.6. Seebeck coefficients of (a) Undoped CTS nanobulk (Ref. 15), (b) Pellet_0:10, (c) Pellet_10:0, (d) Pellet_5:5_ALE, (e) Pellet_9:1_ALE and (f) Pellet_9:1_BLE. Red and blue circles represent data measured in heating and cooling cycles, respectively.

Figure 4.8. Shows the thermoelectric properties of Pellet_0:10, Pellet_10:0, Pellet_9:1_ALE and Pellet_5:5_ALE. For comparison, the data of undoped nonnanostructured monoclinic CTS[7] and undoped CTS nanobulk material[15] are also shown. As seen in Figure 4.8 (a), the *S* value of Pellet_10:0 is much lower than that of Pellet_0:10. In addition, Pellet_10:0 showed a metallic behavior with higher σ, while Pellet_0:10 exhibited a semiconductor behavior with significantly low σ [Figure 4.8 (b)]. This is mainly due to the presence of the residual WZ phase in the pellet.[15] The values of *S* of Pellet_9:1_ALE and Pellet_5:5_ALE are approximately the

same as that of Pellet_0:10 [Figure 4.8 (a)], while the σ and power factor ($PF = \sigma S^2$) of Pellet_9:1_ALE and Pellet_5:5_ALE are in between those of Pellet_0:10 and Pellet_10:0 [Figure 4.8 (b) and (e)].

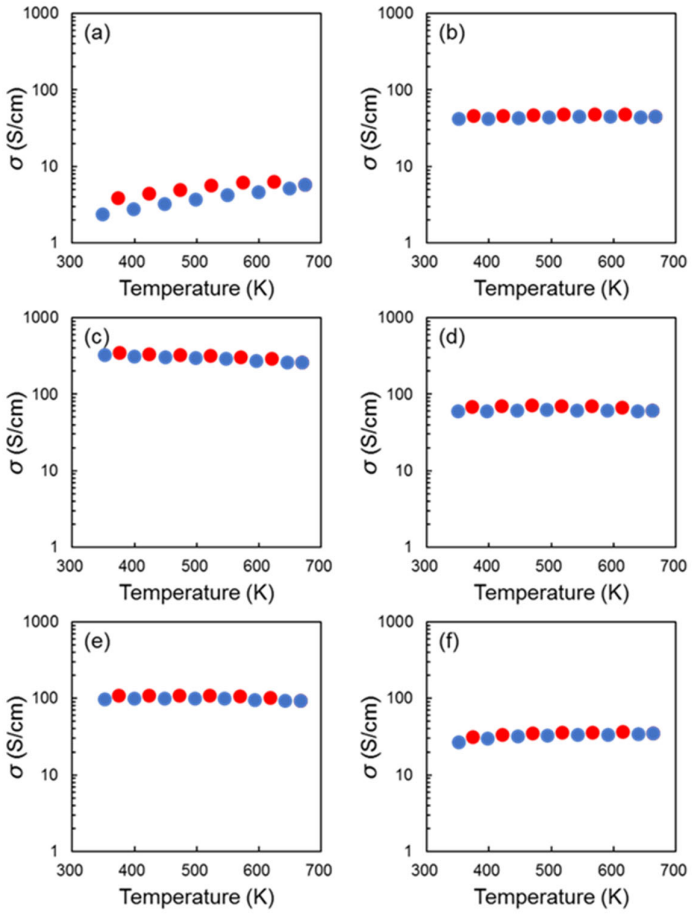

Figure 4.7. Electrical conductivities of (a) Undoped CTS nanobulk (Ref.15), (b) Pellet_0:10, (c) Pellet_10:0, (d) Pellet_5:5_ALE, (e) Pellet_9:1_ALE and (f) Pellet_9:1_BLE. Red and blue circles represent data measured in heating and cooling cycles, respectively.

As seen in Figure 4.8 (c) and (d), Pellet_0:10, Pellet_9:1_ALE and Pellet_5:5_ALE manifested as low κ and κ_{lat} as undoped CTS nanobulk material, suggesting that the phonon scattering is successfully facilitated by nanostructuring and dominated by defect scattering. As a consequence, both blended nanobulk materials (Pellet_9:1_ALE and Pellet_5:5_ALE)

showed ZT = 0.64 and 0.46 at 670 K, respectively [Figure 4.8 (f)]. Because the ZT values of the pristine Zn15-CTS and Zn10-CTS nanobulk materials (Pellet_10:0 and Pellet_0:10) were ZT = 0.37 and 0.33 at 670 K, it is evident that the further enhancement of the ZT value of $Cu_2Sn_{1-x}Zn_xS_3$ nanobulk materials was successful by blending two heterogeneous (but nearly identical) $Cu_2Sn_{1-x}Zn_xS_3$ nanoparticle.

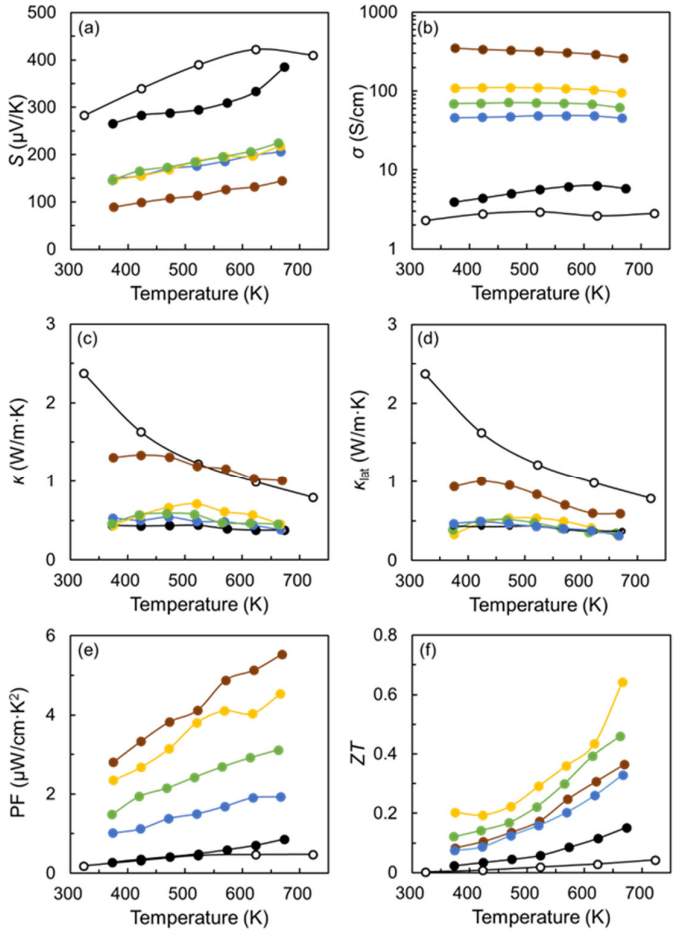

Figure 4.8. (a) S, (b) σ, (c) κ, (d) κ_{lat}, (e) PF and (f) ZT of Pellet_0:10 (filled blue circles), Pellet_10:0 (filled brown circles), Pellet_9:1_ALE (filled yellow circles) and Pellet_5:5_ALE (filled green circles). The open circles represent the data of undoped non-nanostructured monoclinic CTS taken from Ref.7. Filled black circles represent the data of undoped CTS nanobulk taken from Ref.15. It should be noted that we measured S and σ both in heating and cooling cycles and found the values coincide in both cycles. Therefore, the values in only the heating cycle are shown here.

The reason why the *ZT* value of Pellet_9:1_ALE is 1.4 times higher than that of Pellet_5:5_ALE is that *PF* of Pellet_9:1_ALE is much higher than that of Pellet_5:5_ALE despite having almost identical values of κ_{lat}, as shown in Figure 4.8 (d) and (e). From this result, it was confirmed that the inclusion of a small amount of Zn10-CTS nanodomains (ca. 10 vol%) into a Zn15-CTS host material caused an effective reduction of κ_{lat} without significantly deteriorating the charge transport properties, leading to a high *ZT* value of 0.64 (at 673 K).

4.4.3 Electrical Resistivity Anisotropy

Because Pellet_9:1_ALE might have a submicron scale heterogeneous structure, we needed to find out if the pellet is isotropic in terms of charge transport properties, otherwise there might be a risk of overestimating the *ZT* value, because κ was measured for the pellet in the cross-plane direction while *S* and σ were measured in the inplane direction. To precisely measure the electrical resistivity of anisotropic materials, Montgomery's method[25] is employed. Briefly, small electrodes were attached at the four corners of the faces of both in-plane and cross-plane specimens. Then, the electrical resistivity between two adjacent electrodes (ρ_{ij}) was measured, as shown in Figure 4.3 (c).

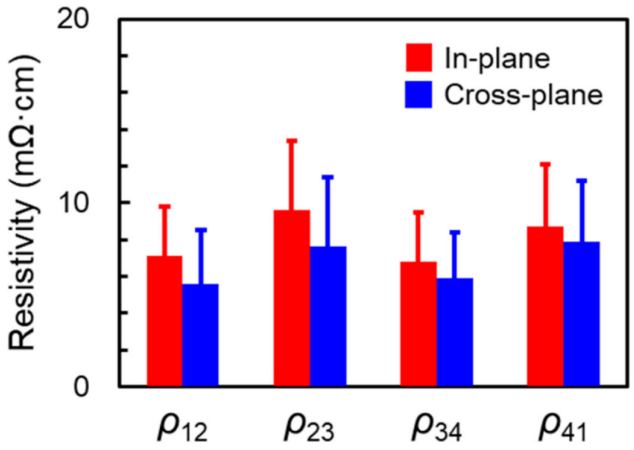

Figure 4.9. In-plane (red) and cross-plane (blue) electrical resistivity of Pellet_9:1_ALE.

The average resistivity of in-plane and cross-plane specimens was measured to be 8.0 ± 2.7 and 6.8 ± 2.7 mΩ·cm, respectively, as shown in Figure 4.9 confirming that Pellet_9:1_ALE is isotropic in terms of charge transport properties.

4.4.4 Sea-Island Structure and Property Relation

Pellet_9:1_ALE was fabricated by mixing a methanol dispersion of TU-capped Zn15-CTS nanoparticles with a methanol dispersion of TU-capped Zn10-CTS nanoparticles in such a way that the weight ratio of Zn15-CTS to Zn10-CTS in blended nanoparticles is 9:1 followed by drying and pelletization. Because the colloidal dispersion stability of TU-capped nanoparticles in methanol is poor, Zn15-CTS and Zn10-CTS nanoparticles could not be fully mixed with each other at the single particle level. Therefore, it is highly possible that aggregates of Zn10-CTS nanoparticles exist in the Zn15-CTS host matrix as nanoinclusions forming a sea-island structure. The structural characteristics of the sea-island structure including the size of islands, the island-to-island spacing, the shape of islands, etc., would influence on thermoelectric properties.

To confirm this supposition, we fabricated another pellet (Pellet_9:1_BLE) with the same mixing ratio. Pellet_9:1_BLE was fabricated by mixing a DDT dispersion of DDT/OAM-capped Zn15-CTS nanoparticles with a DDT dispersion of DDT/OAM-capped Zn10-CTS nanoparticles in such a way that the weight ratio of Zn15-CTS to Zn10-CTS in blended nanoparticles is 9:1 followed by ligand exchange (for more details, see the Experimental Section 4.2.2). Because it is necessary to remove those insulating ligands (DDT and OAM) from the surface of nanoparticles before making a pellet, ligand exchange of the nanoparticles from DDT/OAM to TU was carried out. Then, the resulting TU-capped nanoparticles were dried and pelletized. The colloidal dispersion stability of DDT/OAM-capped nanoparticles in DDT is much higher than that of TU-capped nanoparticles in methanol, and thus Zn15-CTS and Zn10-CTS nanoparticles could be mixed with each other at the single particle level. As a

result, every single Zn10-CTS nanoparticle would be homogeneously dispersed in the Zn15-CTS host matrix with different sea-island structural characteristics from Pellet_9:1_ALE.

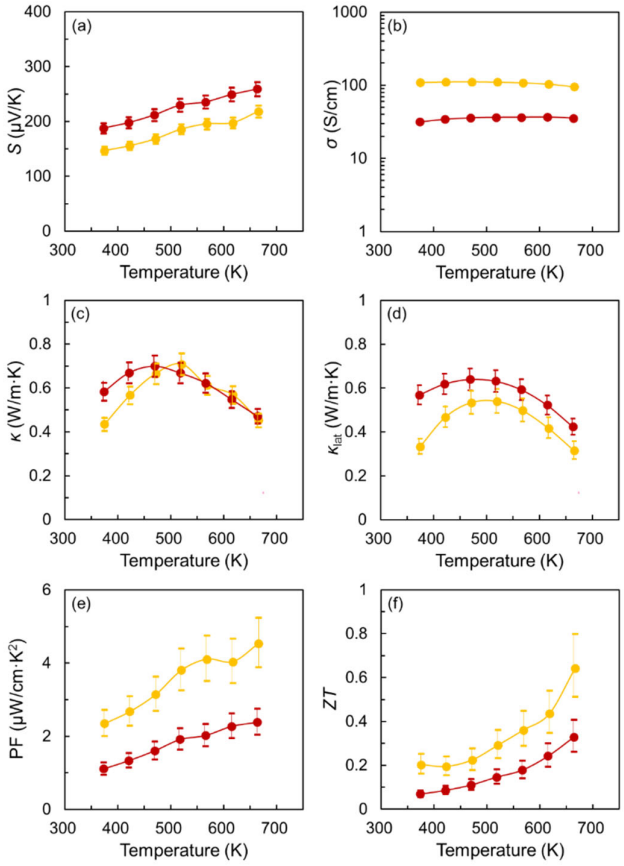

Figure 4.10. (a) *S*, (b) σ, (c) κ, (d) κ_{lat}, (e) *PF* and (f) *ZT* of Pellet_9:1_ALE (yellow circles) and Pellet_9:1_BLE (red circles).

Figure 4.10 Shows the thermoelectric properties of Pellet_9:1_ALE and Pellet_9:1_BLE. As seen in Figure 4.10 (a), (b) and (e), Pellet_9:1_BLE showed higher *S*, lower σ and lower *PF* than Pellet_9:1_ALE, while it manifested as low κ and κ_{lat} as Pellet_9:1_ALE as shown in Figure 4.10 (c) and (d). As a consequence, Pellet_9:1_BLE showed $ZT = 0.33$ at 670 K, as shown in Figure 4.10 (f). The *ZT* values of Pellet_9:1_ALE, Pellet_9:1_BLE, pristine Zn15-CTS and Zn10-CTS nanobulk are summarized in Figure 4.11. The *ZT* value of Pellet_9:1_BLE is as low as those of the pristine Zn15-CTS and Zn10-CTS nanobulk materials as shown in

Figure 4.11. This result strongly suggests that the structural characteristics of the sea-island structure would significantly influence the TE properties. In this particular case, the island-to-island spacing is probably too small to effectively enhance the *ZT* value by reducing κ_{lat} without significantly deteriorating the *PF* value.

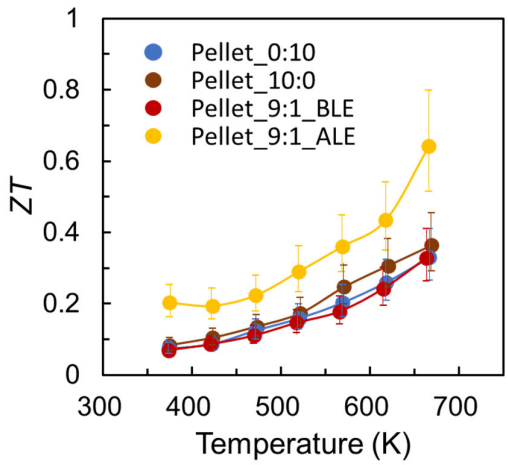

Figure 4.11. *ZT* of Pellet_0:10 (blue circles), Pellet_10:0 (brown circles), Pellet_9:1_ALE (yellow circles) and Pellet_9:1_BLE (red circles).

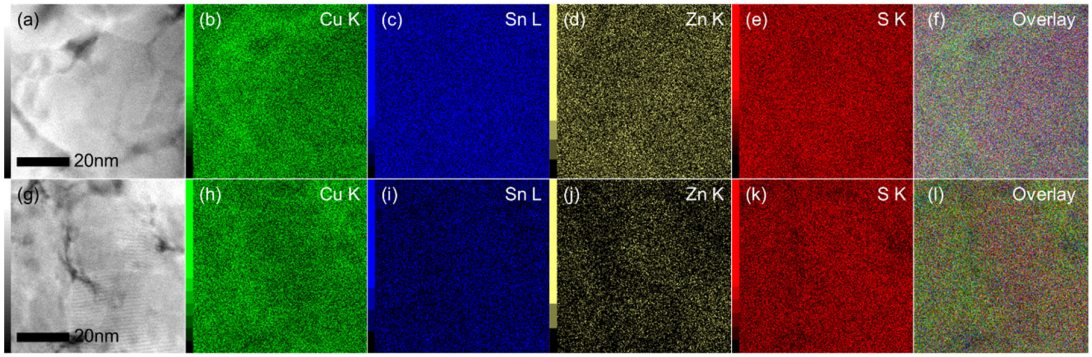

Figure 4.12. Cross-sectional HAADF-STEM and EDS elemental mapping images of (a-f) Pellet_9:1_ALE and (g-l) Pellet_9:1_BLE. (a, g) HAADF-STEM images; (b, h) Cu K line; (c, i) Sn L line; (d, j) Zn K line; (e, k) S K line; and (f, l) overlay.

To confirm the sea-island structures are different from each other between Pellet_9:1_ALE and Pellet_9:1_BLE, cross sectional HAADF-STEM imaging and EDS elemental mapping

were carried out. The cross-sectional HAADF-STEM and EDS elemental mapping images of Pellet_9:1_ALE and Pellet_9:1_BLE are shown in Figure 4.12. The contrast of the STEM-HAADF image is relatively uniform in both cases even though some dark areas were observed suggesting the successful formation of homogeneous pellets. The EDS elemental mapping images also confirm that the pellets are compositionally uniform. However, because the difference in composition between Zn15-CTS and Zn10-CTS domains is quite small, it was extremely difficult to visualize Zn10-CTS nanoinclusions in the Zn15-CTS host matrix by those techniques.

4.4.5 SAED Analyses

To reveal differences in the sea-island structure between Pellet_9:1_ALE and Pellet_9:1_BLE, the SAED analyses using HRTEM were performed for both pellets. Figure 4.13 (a) shows a cross-sectional TEM image of Pellet_9:1_ALE. SAED patterns were obtained from five randomly selected regions within the pellet, as indicated by the number in Figure 4.13 (a), with two different aperture sizes (770 and 280 nm). Figure 4.13 (b) and (c) show SAED patterns obtained from region 1 in Figure 4.13 (a), with aperture sizes of 770 and 280 nm, respectively. SAED peak intensity profiles along the Debye-Scherrer rings indexed to the ZB(111) [as well as WZ(002)] (green circles) and WZ(103) (red circles) planes [Figure 4.13 (d)] after the background subtraction [Figure 4.13 (e)] are shown in Figure 4.13 (f) and (g). SAED peak intensities were summed for each profile, excluding the beams' stop region, and denoted as $I_{ZB(111)}$ and $I_{WZ(103)}$, respectively. The ratios of $I_{WZ(103)}$ to $I_{ZB(111)}$ were calculated with aperture sizes of 770 and 280 nm from five randomly selected regions within Pellet_9:1_ALE. The same analyses were also carried out for Pellet_9:1_BLE. As clearly seen in Figure 4.13 (h), in the case of Pellet_9:1_ALE, $I_{WZ(103)}/I_{ZB(111)}$ calculated with an aperture size of 770 nm are approximately constant for all the regions, while there is considerable variation in the values of $I_{WZ(103)}/I_{ZB(111)}$ calculated with an aperture size of 280 nm between regions. In the case of

Pellet_9:1_BLE, conversely, the values of $I_{WZ(103)}/I_{ZB(111)}$ are virtually constant for all the regions regardless of aperture size [Figure 4.13 (h)].

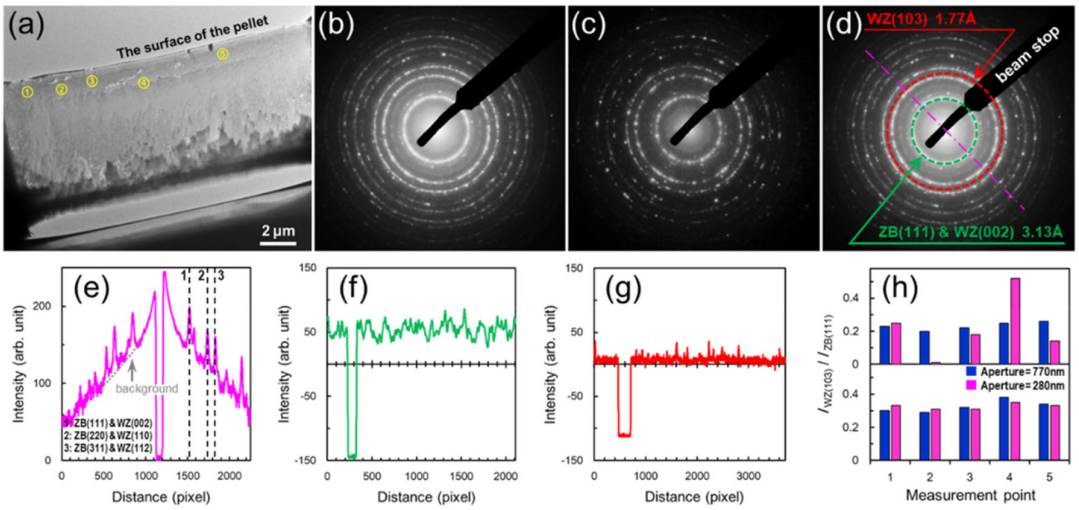

Figure 4.13. (a) Cross-sectional TEM image of Pellet_9:1_ALE. SAED patterns were obtained from five randomly selected regions within the pellet as indicated by the numbers. (b, c) SAED patterns obtained from region 1 in panel a with aperture sizes of (b) 770 and (c) 280 nm. (d) The Debye-Scherer rings indexed to the ZB(111) and WZ(103) planes are indicated by green and red dashed circles, respectively, using the same SAED pattern as in panel b. (e) Line profile of the SAED pattern obtained along the purple dashed-dotted line in panel d. (f, g) SAED peak intensity profiles along (f) green and (g) red circles in panel d after the background subtraction. (h) $I_{WZ(103)}/I_{ZB(111)}$ calculated with aperture sizes of (blue) 770 and (pink) 280 nm from five randomly selected regions within (top) Pellet_9:1_ALE and (bottom) Pellet_9:1_BLE.

These results indicate that Pellet_9:1_ALE has a larger size of islands and larger island-to-island spacing than Pellet_9:1_BLE. In the case of Pellet_9:1_ALE, the average island size is probably larger than 200 nm but much smaller than 700 nm. In addition, the average island-to-island spacing might be larger than 200-300 nm. In the case of Pellet_9:1_BLE, both the average island size and the average island-to-island spacing are presumably smaller than 200 nm. Therefore, σ was significantly reduced, leading to the lower *PF* and lower *ZT* values than for Pellet_9:1_ALE. In other words, it is quite important to precisely control the structural

characteristics of the sea-island structure (not only the volume fraction of nanoinclusions) for effective enhancement of the *ZT* value. In addition, the difference in sea-island structure may lead to a hypothesis that can explain the TE properties differences by taking account the inevitable electron-phonon interaction. Since the Pellet_9:1_BLE has a rather uniform nanoinclusion distribution, the probability of electron scattering is higher compared to that in the Pellet_9:1_ALE. When electron is scattered by the nanoinclusions, it is highly possible to emit a phonon with a certain energy, known as electron-phonon interaction, leading to a lower electrical and a higher lattice thermal conductivities. However, to clarify the contribution of electron-phonon interaction on TE properties, more theoretical analysis is required in the future. In our case, we performed the theoretical analysis of thermal conductivity using the following equation based on Boltzmann theory:

$$K_n = \int \theta(\varepsilon, T)(\varepsilon - \mu)^n \left(-\frac{\partial f_{\mathrm{FD}}}{\partial \varepsilon}\right) \mathrm{d}\varepsilon,$$
$$\sigma(T) = K_0, \quad S(T) = -\frac{1}{|e|T}\frac{K_1}{K_0}, \quad \kappa_{\mathrm{car}}(T) = \frac{1}{|e|^2 T}\left(K_2 - \frac{{K_1}^2}{K_0}\right) \tag{1}$$

where K_n is the transport coefficient, θ is the spectrum conductivity, ε is the energy, μ is the chemical potential, f_{FD} is the Fermi-Dirac distribution function, e is the elementary charge, σ is the electrical conductivity, S is the Seebeck coefficient, and κcar is the carrier thermal conductivity. According to Sommerfeld expansion, κ_{car} can be approximated as

$$\kappa_{\mathrm{car}}(T) = \frac{1}{|e|^2 T} K_2 - S^2 \sigma T \cong L_0 \sigma T - S^2 \sigma T \qquad (E_{\mathrm{F}} \gg k_{\mathrm{B}} T) \tag{2}$$

where E_F is the Fermi energy, L_0 is the Lorentz number of 2.44×10^{-8} V^2K^{-2}. In case of typical metallic system, the term of $S^2\sigma T$ is very small, and thus the second term in Eq. (2) is negligible. However, for the high power factor materials (such as materials in the present study), the second term can't be ignored. Therefore, we calculated κ_{car} of Pellet_9:1_ALE and Pellet_9:1_BLE based on Eq. (2). As a results, the values of κ_{car} of Pellet_9:1_ALE and

Pellet_9:1_BLE at 673 K are calculated to be -0.14 and -0.09 $WK^{-1}m^{-1}$, respectively, indicating that κcar is almost zero for both samples. The negative value of κ_{car} is because the samples in the present study don't meet the condition of $E_F >> k_BT$. Because $Cu_2Sn_{1-x}Zn_xS_3$ is a degenerate semiconductor, the value of L_0 will not significantly differ from 2.44×10^{-8} V^2K^{-2}. Therefore, the lattice thermal conductivity, κ_{lat}, is approximately equal to κ for both samples.

The reason why the lattice thermal conductivities (κ_{lat}) of Pellet_9:1_ALE and Pellet_9:1_BLE seem to be significantly different would be mainly due to the measurement error. Therefore, we added error bars in Figure 4.10 (d). The values of κ_{lat} do not differ significantly each other. Nevertheless, there still remains a slight difference between the values of κ_{lat} of Pellet_9:1_ALE and Pellet_9:1_BLE. This is probably due to the difference in the mean size on nanoinclusions and the separation distance among them. For example, the larger nanoinclusions may be able to effectively scatter phonons. However, it is not clear yet how those structural features influence on κ_{lat}, and thus such a study remains as part of our future research directions. Above this, we think the electron-phonon interaction differs in these two samples is difficult to clarify.

4.4.6 Effective Medium Theory

To further discuss the enhanced thermoelectric properties of blended nanobulk materials (Pellet_9:1_ALE and Pellet_5:5_ALE), the effective medium theory (EMT) and its generalized version taking into account percolation theory (GEMT) have been used to estimate the thermoelectric properties of blended materials where randomly distributed nanoinclusions are embedded in a host matrix.[27-30] According to EMT, the effective Seebeck coefficient (S_{eff}) is given by a mixture rule using the Seebeck coefficients of the host material (S_h) and inclusions (S_i) as

$$(1-\varphi_{\mathrm{i}})\frac{\kappa_{\mathrm{h}}/S_{\mathrm{h}}-\kappa_{\mathrm{eff}}/S_{\mathrm{eff}}}{\kappa_{\mathrm{h}}/S_{\mathrm{h}}+2\,\kappa_{\mathrm{eff}}/S_{\mathrm{eff}}}+\varphi_{\mathrm{i}}\frac{\kappa_{\mathrm{i}}/S_{\mathrm{i}}-\kappa_{\mathrm{eff}}/S_{\mathrm{eff}}}{\kappa_{\mathrm{i}}/S_{\mathrm{i}}+2\,\kappa_{\mathrm{eff}}/S_{\mathrm{eff}}}=0 \quad (1)$$

where φ_{i}, κ_{h}, κ_{i} and κ_{eff} respectively denote the volume fraction of inclusions, the thermal conductivity of the host material (Zn15-CTS), the thermal conductivity of the inclusion phase (Zn10-CTS) and the effective thermal conductivity. The effective electrical conductivity (σ_{eff}) can be calculated based on GEMT as[30]

$$(1-\varphi_{\mathrm{i}})\frac{\sigma_{\mathrm{h}}^{1/t}-\sigma_{\mathrm{eff}}^{1/t}}{\sigma_{\mathrm{h}}^{1/t}+\sigma_{\mathrm{eff}}^{1/t}(1-\varphi_{\mathrm{c}})/\varphi_{\mathrm{c}}}+\varphi_{\mathrm{i}}\frac{\sigma_{\mathrm{i}}^{1/t}-\sigma_{\mathrm{eff}}^{1/t}}{\sigma_{\mathrm{i}}^{1/t}+\sigma_{\mathrm{eff}}^{1/t}(1-\varphi_{\mathrm{c}})/\varphi_{\mathrm{c}}}=0 \quad (2)$$

where φ_{c}, t, σ_{i}, and σ_{h} represent the effective percolation threshold, critical exponent, the electrical conductivities of the inclusion phase and the host material, respectively. The value of t determines the effective percolation slope, and the value of t is normally between 1 and 3. The value of φ_{c} can vary in a wide range to fit the experimental data. In this study, t and φ_{c} were fixed at 1.2 and 0.5, respectively. κ_{eff} can also be calculated based on GEMT as[30]

$$(1-\varphi_{\mathrm{i}})\frac{\kappa_{\mathrm{h}}^{1/t}-\kappa_{\mathrm{eff}}^{1/t}}{\kappa_{\mathrm{h}}^{1/t}+\kappa_{\mathrm{eff}}^{1/t}(1-\varphi_{\mathrm{c}})/\varphi_{\mathrm{c}}}+\varphi_{\mathrm{i}}\frac{\kappa_{\mathrm{i}}^{1/t}-\kappa_{\mathrm{eff}}^{1/t}}{\kappa_{\mathrm{i}}^{1/t}+\kappa_{\mathrm{eff}}^{1/t}(1-\varphi_{\mathrm{c}})/\varphi_{\mathrm{c}}}=0 \quad (3)$$

In Table 4.3, S, σ, κ and ZT (at 670 K) of Pellet_0:10, Pellet_10:0, Pellet_9:1_ALE, Pellet_5:5_ALE, and Pellet_9:1_BLE are summarized.

In Figure 4.14, σ, κ, S and ZT (at 670 K) are plotted as a function of φ_{i} together with theoretical curves obtained by Equations (1)-(3). It is clearly seen that both σ and κ of blended nanobulk materials are greatly reduced in comparison with the theoretical prediction, suggesting that the influence of defect scattering on both carrier and phonon transport properties is significant. Meanwhile, S of blended nanobulk materials is higher than theoretical prediction. As a

consequence, the *ZT* of Pellet_9:1_ALE and Pellet_5:5_ALE is higher than the theoretical prediction, because they have a suitable sea-island structural characteristic for effective enhancement of the *ZT* value, reducing κ_{lat} while maintaining σ. When one compares σ and *S* of Pellet_9:1_BLE with those of Pellet_9:1_ALE, σ of Pellet_9:1_BLE is lower than that of Pellet_9:1_ALE, while *S* of Pellet_9:1_BLE is higher than that of Pellet_9:1_ALE [Figure 4.14 (a) and (c)]. To clarify the underlying physics of this observation, Hall measurements were carried out as discussed below.

Table 4.3. *S*, σ, κ and *ZT* (at 670 K) of pristine and blended nanobulk materials.

	***S* (μV/K)**	**σ (S/cm)**	**κ (W/m·K)**	***ZT***
Pellet_0:10	205.9	45.5	0.38	0.33
Pellet_10:0	145.0	263.0	1.00	0.37
Pellet_9:1_ALE	218.2	95.2	0.45	0.64
Pellet_5:5_ALE	224.5	61.9	0.45	0.46
Pellet_9:1_BLE	259.2	35.5	0.47	0.33

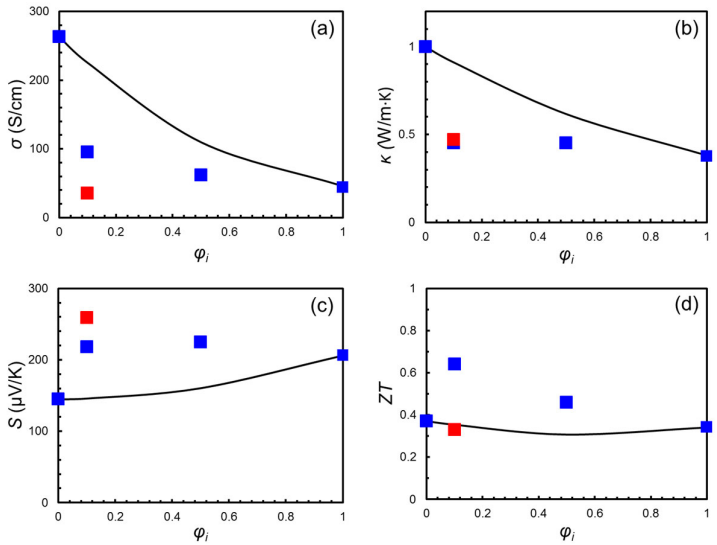

Figure 4.14. (a) σ, (b) κ, (c) *S* and (f) *ZT* plotted as a function of φ_i (at 670 K). Blue squares represent the values of Pellet_10:0, Pellet_9:1_ALE, Pellet_5:5_ALE and Pellet_0:10 (from left to right). Red squares represent the values of Pellet_9:1_BLE. Solid lines correspond to theoretical curves calculated based on Equations (1)-(3).

4.4.7 Hall Measurement

Figure 4.15 (a) and (b) show the temperature dependence of carrier concentration n and Hall mobility μ for Pellet_9:1_BLE, Pellet_9:1_ALE and Pellet_5:5_ALE. The values of n for all pellets are approximately constant between 10 and 300 K, indicating that they are degenerate semiconductor materials. The values of n for both Pellet_9:1_ALE and Pellet_5:5_ALE are larger than those of Pellet_9:1_BLE by about 1.4 times. This result is semi-quantitatively consistent with the difference in S between Pellet_9:1_ALE (or Pellet_5:5_ALE) and Pellet_9:1_BLE [Figure 4.14 (c)]. As shown in Table 4.4, the values of n at room temperature of both Pellet_10:0 and Pellet_0:10 are approximately the same (ca. 2×10^{21} cm^{-3}). In the cases of blended materials, on the other hand, the values of n are less than half of that of pristine materials as shown in Table 4.4 and Figure 4.15.

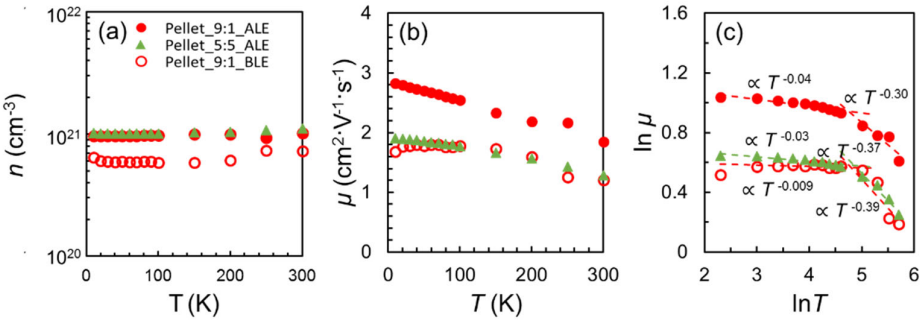

Figure 4.15. (a) Carrier concentration n and (b) Hall mobility μ as a function of T. (c) ln μ – ln T plot. Filled and open red circles represent the data of Pellet_9:1_ALE and Pellet_9:1_BLE, respectively. Green triangle represent the data of Pellet_5:5_ALE.

This result suggests that the interfaces between nanoinclusions and host material might act as trap sites for carriers. Because Pellet_9:1_BLE has a much larger interface area than Pellet_9:1_ALE (or Pellet_5:5_ALE), Pellet_9:1_BLE would have a higher density of trap sites than Pellet_9:1_ALE (or Pellet_5:5_ALE). This could be the reason why the value of n of Pellet_9:1_BLE is lower than that of Pellet_9:1_ALE (or Pellet_5:5_ALE). Meanwhile, the μ of all pellets decreases with increasing temperature.

Table 4.4. *S, σ, n* and μ (at r.t.) of pristine and blended nanobulk materials.

	S ($\mu V \cdot K^{-1}$)	σ ($S \cdot cm^{-1}$)	n (cm^{-3})	μ ($cm^2 \cdot V^{-1} \cdot s^{-1}$)
Pellet_9:1_ALE	132.7	107.1	1.02×10^{21}	0.65
Pellet_9:1_BLE	167.0	28.4	7.28×10^{20}	0.24
Pellet_10:0	79.9	364.8	2.07×10^{21}	1.10
Pellet_0:10	126.0	45.3	1.96×10^{21}	0.14

Figure 4.15 (c) shows ln μ – ln T curves of Pellet_9:1_BLE, Pellet_9:1_ALE and Pellet_5:5_ALE. Normally, when the impurity scattering is the domain scattering mechanism, the material exhibits a temperature dependence of $T^{3/2}$ on carrier mobility. As temperature increasing, the domain scattering mechanism changes from impurity scattering to neutral scattering, then acoustic phonon scattering. Subsequently, the T dependence transforms from $T^{3/2}$ to T^0 to $T^{-3/2}$.[31, 32] For our materials, we fitted the ln μ – ln T curves of Pellet_9:1_ALE, Pellet_9:1_BLE and Pellet_5:5_ALE using a simple model $\ln\mu = r\ln T + A$, with r being the scattering rate factor and A being an off-set as shown in Figure 1 (c). In 10K-200K, Pellet_9:1_ALE, Pellet_5:5_ALE, Pellet_9:1_BLE exhibit $T^{-0.04}$, $T^{-0.03}$and $T^{-0.009}$ dependence while they show $T^{-0.30}$, $T^{-0.37}$ and $T^{-0.39}$ dependence in 200K-300K. The scatter ratio is 0.04, 0.03 and 0.009 for Pellet_9:1_ALE, Pellet_5:5_ALE, Pellet_9:1_BLE, respectively in 10K-200K. The scatter ratio is 0.30, 0.37 and 0.39 for Pellet_9:1_ALE, Pellet_5:5_ALE, Pellet_9:1_BLE, respectively in 200K-300K. Since then, it signify that neutral impurity scattering is dominant in 10K-200K, while it also indicates that acoustic phonon scattering probability increases with temperature in 200K-300K.

From the Figure 4.15 (c), it can be concluded that the carrier scattering mechanisms of Pellet_9:1_BLE, Pellet_9:1_ALE and Pellet_5:5_ALE remain basically the same, while the values of μ of Pellet_9:1_ALE are always larger than those of Pellet_9:1_BLE and

Pellet_5:5_ALE, because the sea-island structure of Pellet_9:1_ALE is beneficial for maintaining the high μ of the Zn15-CTS host material, even though φ_i of Pellet_9:1_ALE and Pellet_9:1_BLE are the same.

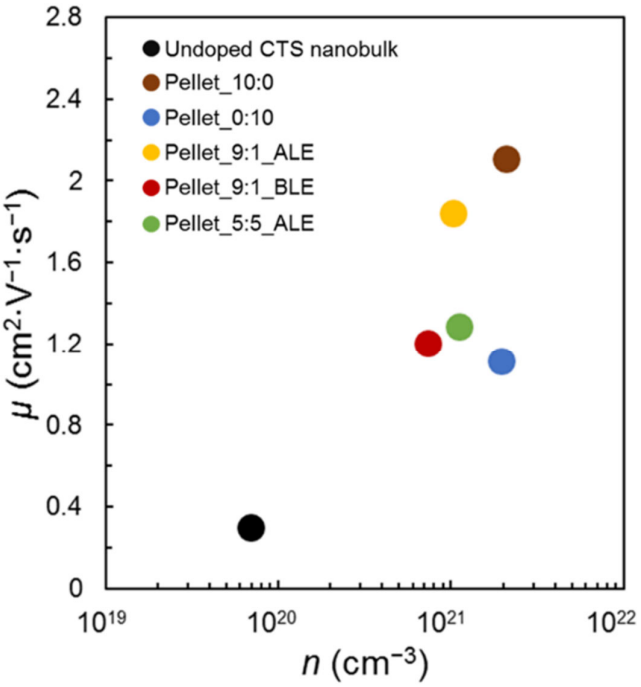

Figure 4.16. Room-temperature Hall mobility as a function of n. Yellow, red and green circles represent the values of Pellet_9:1_ALE, Pellet_9:1_BLE and Pellet_5:5_ALE, respectively. Black, blue and brown circles represent the values of undoped CTS nanobulk (Ref.15), Pellet_0:10 and Pellet_10:0, respectively.

In order to see whether there is an existence of the modulation doping effect[33, 34] for Pellet_9:1_BLE, Pellet_9:1_ALE and Pellet_5:5_ALE, we plotted μ as a function of n as shown in Figure 4.16. As seen in Figure 4.16, the values of μ scatter suggesting that there is a possibility of the existence of the modulation doping effect in the blended nanobulk materials. It remains as a future work to clarify whether the modulation doping effect is responsible for

the larger μ of Pellet_9:1_ALE. Through the discussion above, the possible mechanism of carrier and phonon transport in Pellet_9:1_ALE and Pellet_9:1_BLE in this study could be described in the following illustration scheme 4.2.

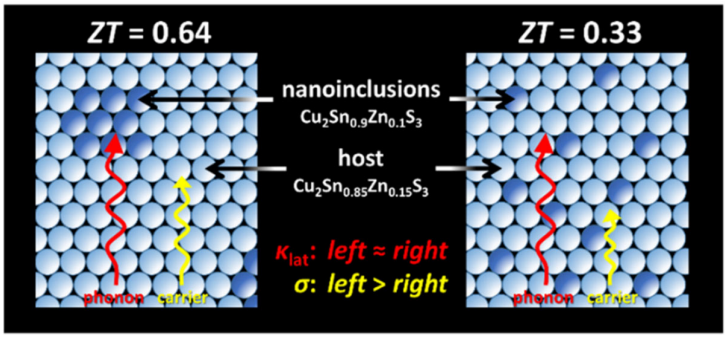

Scheme 4.2. Illustration of the possible mechanism of carrier and phonon transport in Pellet_9:1_ALE and Pellet_9:1_BLE.

4.5 Conclusions

The $Cu_2Sn_{1-x}Zn_xS_3$ system contains environmentally benign and abundant elements and exhibits modest thermoelectric properties at a relatively low temperature range. In theory, introducing nanoinclusions into a $Cu_2Sn_{1-x}Zn_xS_3$-based thermoelectric material in a controlled manner will enable us to enhance its *ZT* value in comparison to the homogeneous counterpart by reducing κ_{lat} while maintaining *PF*. In this study, we chemically synthesized $Cu_2Sn_{0.85}Zn_{0.15}S_3$ (Zn15-CTS) and $Cu_2Sn_{0.9}Zn_{0.1}S_3$ (Zn10-CTS) nanoparticles and the resulting nanoparticles were pelletized by a pulse electric current sintering method. The pristine Zn15-CTS nanobulk material exhibits high σ, high κ and $ZT = 0.37$ at 670 K, while the pristine Zn10-CTS nanobulk exhibits low σ, low κ and $ZT = 0.33$ at 670 K. Surprisingly, the blended $Cu_2Sn_{1-x}Zn_xS_3$ nanobulk obtained by pelletizing a mixture of Zn15-CTS and Zn10-CTS nanoparticles in a weight fraction of 9:1 mixed after the ligand exchange showed a maximum *ZT* value of

0.64 at 670 K. However, the blended nanobulk obtained by pelletizing a mixture of Zn15-CTS and Zn10-CTS nanoparticles in a weight fraction of 9:1 mixed before the ligand exchange showed a $ZT = 0.33$ at 670 K. This result highlights the importance of nanoscale-architectural control of thermoelectric materials to further enhance the thermoelectric figure of merit without using rare and/or toxic elements.

References

(1) Ge, Z.-H.; Zhang, B.-P.; Chen, Y.-X.; Yu, Z.-X.; Liu, Y.; Li, J.-F. Synthesis and Transport Property of $Cu_{1.8}S$ as a Promising Thermoelectric Compound. *Chem. Commun.* **2011**, *47*, 12697−12699.

(2) Suekuni, K.; Tsuruta, K.; Kunii, M.; Nishiate, H.; Nishibori, E.; Maki, S.; Ohta, M.; Yamamoto, A.; Koyano, M. High-performance Thermoelectric Mineral $Cu_{12-x}Ni_xSb_4S_{13}$ Tetrahedrite. *J. Appl. Phys.* **2013**, *113*, 043712.

(3) Suekuni, K.; Kim, F. S.; Nishiate, H.; Ohta, M.; Tanaka, H. I.; Takabatake, T. Highperformance Thermoelectric Minerals: Colusites $Cu_{26}V_2M_6S_{32}$ (M = Ge, Sn). *Appl. Phys. Lett.* **2014**, *105*, 132107.

(4) He, Y.; Day, T.; Zhang, T.; Liu, H.; Shi, X.; Chen, L.; Snyder, G. J. High Thermoelectric Performance in Non-Toxic Earth-Abundant Copper Sulfide. *Adv. Mater*. **2014**, *26*, 3974-3978.

(5) Lu, X.; Morelli, D. T.; Xia, Y.; Ozolins, V. Increasing the Thermoelectric Figure of Merit of Tetrahedrites by Co-Doping with Nickel and Zinc. *Chem. Mater*. **2015**, *27*, 408-413.

(6) Yang, D.; Su, X.; Yan, Y.; He, J.; Uher, C.; Tang, X. Mechanochemical Synthesis of High Thermoelectric Performance Bulk Cu_2X (X = S, Se) Materials. *APL Mater*. **2016**, *4*, 116110.

(7) Shen, Y.; Li, C.; Huang, R.; Tian, R.; Ye, Y.; Pan, L.; Koumoto, K.; Zhang, R.; Wan, C.; Wang, Y. Eco-friendly P-type Cu_2SnS_3 Thermoelectric Material: Crystal Structure and Transport Properties. *Sci. Rep.* **2016**, *6*, 32501.

(8) Suekuni, K.; Takabatake, T. Research Update: Cu–S Based Synthetic Minerals Efficient Thermoelectric Materials at Medium Temperatures. *APL Mater.* **2016**, *4*, 104503.

(9) Tang, Y.-Q.; Ge, Z.-H.; Feng, J. Synthesis and Thermoelectric Properties of Copper Sulfides via Solution Phase Methods and Spark Plasma Sintering. *Crystals*. **2017**, *7*, 141.

(10) Zhang, D.; Yang, J.; Jiang, Q.; Zhou, Z.; Li, X.; Xin, J.; Basit, A.; Ren, Y.; He, X. MultiCations Compound Cu_2CoSnS_4: DFT Calculating, Band Engineering and Thermoelectric Performance Regulation. *Nano Energy.* **2017**, *36*, 156-165.

(11) Ge, Z.-H.; Salvador, J. R.; Nolas, G. S. Selective Synthesis of Cu_2SnSe_3 and Cu_2SnSe_4 Nanocrystals. *Inorg. Chem.* **2014**, *53*, 4445-4449.

(12) Zhang, D.; Yang, J.; Jiang, Q.; Zhou, Z.; Li, X.; Xin, J.; Basit, A.; Ren, Y.; He, X.; Chu, W.; Hou, J. Combination of Carrier Concentration Regulation and High Band Degeneracy for Enhanced Thermoelectric Performance of Cu_3SbSe_4. *ACS Appl. Mater. Interfaces.* **2017**, *9*, 28558-28565.

(13) Tan, Q.; Sun, W.; Li, Z.; Li, J.-F. Enhanced Thermoelectric Properties of Earth Abundant Cu_2SnS_3 via In Doping Effect. *J. Alloys Compd*. **2016**, *672*, 558-563.

(14) Zhao, H.; Xu, X.; Li, C.; Zhang, R.; Huang, R.; Lv, Y.; Li, D.; Hu, X.; Pan, L.; Wang, Y. Cobalt-Doping in Cu_2SnS_3: Enhanced Thermoelectric Performance by Synergy of Phase Transition and Band Structure Modification. *J. Mater. Chem. A.* **2017**, *5*, 23267-23275.

(15) Zhou, W.; Shijimaya, C.; Takahashi, M.; Miyata, M.; Mott, D.; Koyano, M.; Ohta, M.; Akatsuka, T.; Ono, H.; Maenosono, S. Sustainable Thermoelectric Materials Fabricated by using $Cu_2Sn_{1-x}Zn_xS_3$ Nanoparticles as Building Blocks. *Appl. Phys. Lett*. **2017**, *111*, 263105.

(16) Girard, S. N.; He, J.; Zhou, X.; Shoemaker, D.; Jaworski, C. M.; Uher, C.; Dravid, V. P.; Heremans, J. P.; Kanatzidis, M. G. High Performance Na-doped PbTe-PbS

Thermoelectric Materials: Electronic Density of States Modification and Shape Controlled Nanostructures. *J. Am. Chem. Soc*. **2011**, *133*, 16588-16597.

(17) Biswas, K.; He, J.; Blum, I. D.; Wu, C.-I.; Hogan, T. P.; Seidman, D. N.; Dravid, V. P.; Kanatzidis, M. G.; High-Performance Bulk Thermoelectrics with All-Scale Hierarchical Architectures. *Nature*. **2012**, *489*, 414-418.

(18) Zhao, L.-D.; Lo, S.-H.; He, J.; Li, H.; Biswas, K.; Androulakis, J.; Wu, C.-I.; Hogan, T. P.; Chung, D.-Y.; Dravid, V. P.; Kanatzidis, M. G. High Performance Thermoelectrics from Earth-Abundant Materials: Enhanced Figure of Merit in PbS by Second Phase Nanostructures. *J. Am. Chem. Soc.* **2011**, *133*, 20476-20487.

(19) Lee, Y.; Lo, S.-H.; Androulakis, J.; Wu, C.-I.; Zhao, L.-D.; Chung, D.-Y.; Hogan, T. P.; Dravid, V. P.; Kanatzidis, M. G. High-Performance Tellurium-Free Thermoelectrics: AllScale Hierarchical Structuring of p-Type PbSe-MSe Systems (M = Ca, Sr, Ba). *J. Am. Chem. Soc.* **2013**, *135*, 5152-5160.

(20) Jood, P.; Ohta, M.; Kunii, M.; Hu, X.; Nishiate, H.; Yamamoto, A.; Kanatzidis, M. G. Enhanced Average Thermoelectric Figure of Merit of N-Type $PbTe_{1-x}I_x$–MgTe. *J. Mater. Chem. C.* **2015**, *3*, 10401-10408.

(21) Jood, P.; Mehta, R. J.; Zhang, Y.; Peleckis, G.; Wang, X.; Siegel, R. W.; Borca-Tasciuc, T.; Dou, S. X.; Ramanath, G. Al-Doped Zinc Oxide Nanocomposites with Enhanced Thermoelectric Properties. *Nano Lett*. **2011**, *11*, 4337-4342.

(22) Mohanraman, R.; Sankar, R.; Chou, F.-C.; Lee, C.-H.; Iizuka, Y.; Muthuselvam, I. P.; Chen, Y.-Y. Influence of Nanoscale Ag_2Te Precipitates on the Thermoelectric Properties of the Sn Doped P-type $AgSbTe_2$ Compound. *APL Mater*. **2014**, *2*, 096114.

(23) Nozariasbmarz, A.; Roy, P.; Zamanipour, Z.; Dycus, J. H.; Cabral, M. J.; LeBeau, J. M.; Krasinski, J. S.; Vashaee, D. Comparison of Thermoelectric Properties of

Nanostructured Mg_2Si, $FeSi_2$, SiGe, and Nanocomposites of SiGe-Mg_2Si, SiGe-$FeSi_2$. *APL Mater*. **2016**, *4*, 104814.

(24) Pan, Y.; Aydemir, U.; Sun, F.-H.; Wu, C.-F.; Chasapis, T. C.; Snyder, G. J.; Li, J.-F. Self-Tuning n-Type $Bi_2(Te,Se)_3$/SiC Thermoelectric Nanocomposites to Realize High Performances up to 300 °C. *Adv. Sci.* **2017**, *4*, 1700259.

(25) Montgomery, H. C. Method for Measuring Electrical Resistivity of Anisotropic Materials. *J. Appl. Phys*. **1971**, *42*, 2971-2975.

(26) Liang, Q. Phase-Controlled Synthesis of Cu_2SnS_3 Nanocrystals: The Effect of Redox Conditions on the Initial Binary $Cu_{2-x}S$ Nucleation. *Eur. J. Inorg. Chem*. **2016**, *2016*, 3634-3640.

(27) Sonntag, J. Thermoelectric Power in Alloys with Phase Separation (Composites). *J Phys.: Condens. Matter.* **2009**, *21*, 175703.

(28) Gelbstein, Y. Thermoelectric Power and Structural Properties in Two-phase Sn/SnTe Alloys. *J. Appl. Phys.* **2009**, *105*, 023713.

(29) Vaney, J. B.; Piarristeguy, A.; Ohorodniichuck, V.; Ferry, O.; Pradel, A.; Alleno, E.; Monnier, J.; Lopes, E. B.; Gonçalves, A. P.; Delaizir, G.; Candolfi, C.; Dauscher, A.; Lenoir, B. Effective Medium Theory Based Modeling of the Thermoelectric Properties of Composites: Comparison between Predictions and Experiments in the Glass-Crystal Composite System $Si_{10}As_{15}Te_{75}$-$Bi_{0.4}Sb_{1.6}Te_3$. *J. Mater. Chem. C*. **2015**, *3*, 11090-11098.

(30) McLachlan, D. S.; Blaszkiewicz, M.; Newnham, R. E. Electrical Resistivity of Composites. *J. Am. Ceram. Soc.* **1990**, *73*, 2187-2203.

(31) Marcano, G.; Rincón, C.; Chalbaud, L. M. De.; Bracho, D. B.; Sánchez Pérez, G. Crystal growth and structure, electrical, and optical characterization of the semiconductor Cu_2SnSe_3. *J. Appl. Phys.* **2001**, 90, 15.

(32) Ng, H. M.; Doppalapudi, D.; Moustakas, T. D. The role of dislocation scattering in n-type GaN films. *Appl. Phys. Lett.* **1998**, 73, 821-823.

(33) Yu, B.; Zebarjadi, M.; Wang, H.; Lukas, K.; Wang, H.; Wang, D.; Opeil, C. Dresselhaus, M.; Chen, G.; Ren, Z. Enhancement of Thermoelectric Properties by Modulation-Doping in Silicon Germanium Alloy Nanocomposites. *Nano Lett*. **2012**, *12*, 2077-2082.

(34) Pei, Y.-L.; Wu, H.; Wu, D.; Zheng, F.; He, J. High Thermoelectric Performance Realized in a BiCuSeO System by Improving Carrier Mobility through 3D Modulation Doping. *J.Am. Chem. Soc*. **2014**, *136*, 13902-13908.

Chapter 5: Summary and Future Prospects

5.1 Summary

Throughout the experiments and analysis, the settled objectives for this research could be concluded as achieved. The conclusions and achievements are summarized as follows.

In the introduction, the brief information of thermoelectric technology based on Seebeck effect for energy conversion has been discussed. The outlook of the relationship between conversion efficiency and the dimensionless figure of merit *ZT* of thermoelectric materials has been expounded. The topic then changed to the strategies of how to increase the *ZT* values in thermoelectric materials revolving around the following parameters: Seebeck coefficient, electrical conductivity and thermal conductivity. The classical strategies have been listed. After that, the typical thermoelectric materials for thermoelectric application have also been briefly introduced.

Based on the development status and existing problems, we put our attentions on the study of copper tin sulfide as thermoelectric material which contains environmentally friendly, inexpensive and earth abundant elements. The current research works regarding the development and strategies used for improving the *ZT* value of copper tin sulfide have been mentioned. Cu_2SnS_3 is a popular material for photoelectric. For thermoelectric researches, it started from 2016, briefly new. Moreover, the main fabrication process is solid state method. We are the first who using chemical methods to fabricate Cu_2SnS_3 nanoparticles as building block to introduce mesoscale defects into pellets, which helps to reduce the lattice thermal conductivity. In the meantime, Zn doping was employed to enhance the electrical conductivity of nanobulk.

Common chemical synthesis methods for nanoparticles synthesis have been generally introduced along with their mechanisms and impact elements. For the sake of efficiency and

energy-saving, two chemical methods, (i) one pot chemical method and (ii) hot injection method, were chosen in our study for synthesis. By using them, all the strategies (nanostructing and all-scale hierarchical architecturingc, Zn doping) can be combined together easily. Moreover, the two methods allowed us to control over the size, shape and phase of materials easily. As a result, Cu-Sn-S TE nanomaterials were fabricated using these synthetic techniques in this dissertation.

$Cu_2Sn_{1-x}Zn_xS_3$ (x = 0 ~ 0.2) NPs was successfully fabricated by using one pot chemical method. Ligand exchange was performed to remove the extra surface long chain organics on the nanoparticles, which might have an impact on electrical transport. Afterwards, pulse electric current sintering technique was applied to make dense nanobulk materials for thermoelectric property measurements.

It was found that the CTS system exhibits P-type behavior and modest thermoelectric properties at a relatively low temperature range. Introducing nanograins into a CTS-based thermoelectric material successfully enhanced its *ZT* value in comparison to the non-nanostructured counterpart by reducing lattice thermal conductivity while maintaining power factor. Further enhancement of the *ZT* value has been achieved through doping of Zn in these materials. In addition, the wurtzite crystal structure might has reverse effect on the electron transport properties. However, it is not clear which has a stronger effect, whether the the wurtzite structure itself, or the interface between zincblend and wurtzite. As a result, the highest *ZT* value of 0.37 at 670 K is achieved in both $Cu_2Sn_{0.95}Zn_{0.05}S_3$ and $Cu_2Sn_{0.85}Zn_{0.15}S_3$ nanostructured materials. However, this value was comparable to the *ZT* value at the same temperature of the $Cu_2Sn_{0.9}Zn_{0.1}S_3$ non-nanostructured material.

Keeping the advantages of the nanostructing and exploring the effect of controllable size and shape of material on the TE properties, the Cu-Sn-S particles with controllable size and shape were fabricated by using one pot chemical and hot injection method. Eventually, CTS pellets

with three identical grain sizes (28.6 nm, 39.3 nm, 47.2 nm) have been fabricated under controllable conditions. However, unintentional grain size growth was found in all pellets. Thus, the sintering conditions should be further optimized. Nevertheless, the compositional analysis suggested that all pellets showed Sn poor which suggested that the synthesis condition should be further optimized.

Finally, the TE properties were measured for each sample and the relationship between grain sizes and TE performance was investigated. It showed that the thermal conductivity in nanostructured CTS reduced more efficiently with decreasing grain size compared to that in the non-nanostructured CTS material, because of the enhanced phonon scattering at grain boundaries. Surprisingly, a thermal conductivity close to the theoretically predicted lowest value was measured from nanostructured CTS material with a grain size of ~ 30 nm. In addition, all the pellets shown high Seebeck coefficient. Even though the main impact elements (crystal structure, composition difference and grain size) on the electrical transport property in these pellets is still unclear, the results in this study still provide considerable insight and valuable information of how to prepare nano particles and pellets for fabrication of TE materials with controllable grain size.

Lastly, we opened an avenue for introducing inclusions into host materials by using chemical method. Further improvement of TE properties in blended $Cu_2Sn_{1-x}Zn_xS_3$ has been achieved. The structures and sizes of nanoinclusions were found to have a strong effect on electrical transport. In addition, the blended $Cu_2Sn_{1-x}Zn_xS_3$ nanobulk obtained by pelletizing a mixture of Zn15-CTS and Zn10-CTS nanoparticles in a weight fraction of 9:1, which mixed after the ligand exchange, showed a maximum ZT value of 0.64 at 670 K. However, the blended nanobulk obtained by pelletizing a mixture of Zn15-CTS and Zn10-CTS nanoparticles in a weight fraction of 9:1 mixed before the ligand exchange only showed a $ZT = 0.33$ at 670 K. This result highlights the importance of nanoscale-architectural control of thermoelectric materials to

further enhance the thermoelectric figure of merit without using rare and/or toxic elements. The observed behavior can be attributed to electron-phonon interaction that takes place at the interfaces between grains and inclusions. However, we didn't find a well developed theory can support this hypothesis.

5.2 Future Prospects

Based on the conclude work above in chapter 2, $Cu_2Sn_{1-x}Zn_xS_3$ (x = 0 ~ 0.2) NPs were successfully fabricated by chemical method. During the research, it was found that it will be very interesting to investigate the TE properties of pure ZB phase Zn doped CTS. The further improvement of the *ZT* value might be achieved by blending two or more different types of NPs [*e.g.,* ZB phase Zn-doped CTS and mixed-phase (ZB + WZ) Zn-doped CTS] for making a bulk material and/or controlling mesoscale structures by tuning sintering conditions. The research of doping other elements in the nanostructured CTS material is also attractive.

The research work in chapter 3 suggested that it is necessary to further optimize the synthesis conditions to avoid the Sn poor exist in pellets by increasing the input feeding amount of Sn source or increase the synthesis time. To prevent grain size growth and get high dense bulk materials, the sintering conditions could be carefully investigated in detailed. Further enhancement of *ZT* values of the low electrical conductivity CTS material could be expected by compositing metal materials with the small size nanostructured CTS materials. In addition, it will be very interesting to investigate the TE properties of CTS bulk materials fabricate from quantum size particles.

In chapter 4, we concluded that it has advantage to obtain higher *ZT* value in $Cu_2Sn_{1-x}Zn_xS_3$ nanobulk TE system by mixing and changing the weight ratio of Zn15-CTS and Zn10-CTS nanoparticles. However, we don't know whether the maximum *ZT* value of blended nanobulk materials has been achieved or not, because of the lacking in systematic investigations of the

structure and the sizes of the inclusions in the host material. In the future, we will continue to investigate other weight ratios of Zn15-CTS and Zn10-CTS nanoparticles mixed after ligand exchange such as 8/2, 7/3 to obtain an even higher *ZT* value.

List of Publication

Paper

1. W. Zhou, P. Dwivedi, C. Shijimaya, M. Ito, K. Higashimine, T. Nakada, M. Takahashi, D. Mott, M. Miyata, M. Ohta, H. Miwa, T. Akatsuka, and S. Maenosono: “Enhancement of the Thermoelectric Figure of Merit in Blended $Cu_2Sn_{1-x}Zn_xS_3$ Nanobulk Materials”. *ACS Appl. Nano Mater*. 1, (2018) 4819.
2. W. Zhou, C. Shijimaya, M. Takahashi, M. Miyata, D. Mott, M. Koyano, M. Ohta, T. Akatsuka, H. Ono, and S. Maenosono: “Sustainable Thermoelectric Materials Fabricated by using $Cu_2Sn_{1-x}Zn_xS_3$ Nanoparticles as Building Blocks”. *Appl. Phys. Lett*. 111, (2017) 263105.

Conference Presentations

Oral presentation

1. **W. Zhou,** P. Dwivedi, K. Higashimine, M. Miyata, M. Ohta, H. Miwa, T. Akatsuka, and S. Maenosono: "Structure-Property Relations in Thermoelectric Nanobulk Materials Fabricated from $Cu_2Sn_{1-x}Zn_xS_3$ Nanoparticles"日本化学会第 99 春季年会, 16-19 March 2019, 甲南大学, 神戸, 兵庫.
2. **W. Zhou**, C. Shijimaya, K. Higashimine, M. Ohta, M. Miyata, D. Mott, T. Akatsuka, H. Ono, M. Koyano, and S. Maenosono: "Nanostructured Thermoelectric Material Composed of Heterogeneous $Cu_2Sn_{1-x}Zn_xS_3$ Nanoparticles"日本化学会第 98 春季年会, 20-23 March 2018, 日本大学理工学部, 船橋, 千葉.
3. **W. Zhou**, P. Dwivedi, C. Shijimaya, M. Ito, K. Higashimine, T. Nakada, M. Takahashi, D. Mott, M. Miyata, M. Ohta, H. Miwa, T. Akatsuka, and S. Maenosono: "Enhancement of Thermoelectric Figure of Merit in Blended $Cu_2Sn_{1-x}Zn_xS_3$ Nanobulk Materials"第 15 回日本熱電学会学術講演会, 13-15 September 2018, 東北大学, 仙台, 宮城.
4. **W. Zhou**, P. Dwivedi, C. Shijimaya, M. Ito, K. Higashimine, T. Nakada, M. Takahashi, D. Mott, M. Miyata, M. Ohta, H. Miwa, T. Akatsuka, and S. Maenosono:"Improvement of Thermoelectric Performance of $Cu_2Sn_{1-x}Zn_xS_3$ Nanobulk Materials Fabricated by a Bottom-up Approach"第 69 回コロイドおよび界面化学討論会, 18-20 September 2018, 筑波大学, つくば, 茨城.
5. P. Dwivedi, **W. Zhou**, M. Ohta, M. Miyata, H. Takida, T. Akatsuka, and S. Maenosono: "Nanobulk Thermoelectric Materials Fabricated from Chemically Synthesized $Cu_3Al_{1-x}Zn_xSnS_5$ Nanocrystals" 38th Annual International Conference on Thermoelectrics and 4th Asian Conference on Thermoelectrics (ICT/ACT2019), 30 June - 4 July 2019, Hwabaek International Convention Center, Gyeongju, South Korea.
6. P. Dwivedi, **W. Zhou**, M. Ohta, M. Miyata, H. Miwa, T. Akatsuka, and S. Maenosono: "Chemical Synthesis of Cu-Al-Sn-S Nanocrystals toward Sustainable Thermoelectric Materials"日本化学会第 99 春季年会, 16-19 March 2019, 甲南大学, 神戸, 兵庫.
7. P. Dwivedi, **W. Zhou**, M. Ohta, M. Miyata, H. Miwa, T. Akatsuka, and S. Maenosono:

"Nanobulk Thermoelectric Materials Composed of Chemically-Synthesized Cu-Al-Sn-S Nanocrystals" 第 15 回日本熱電学会学術講演会, 13-15 September 2018, 東北大学, 仙台, 宮城.

8. 費 舒杰, 中田 豪, **周 薇**, P. Dwivedi, 太田 道広, 赤塚 威夫, 前之園 信也: "Co-Sb-S 熱電ナノ粒子の化学合成と構造解析" 日本化学会第 99 春季年会, 16-19 March 2019, 甲南大学, 神戸, 兵庫.
9. T. Nakada, C. Shijimaya, K. Higashimine, M. Takahashi, **W. Zhou**, P. Dwivedi, M. Ohta, H. Miwa, T. Akatsuka, M. Miyata, and S. Maenosono: "Sustainable Thermoelectric Materials Fabricated by using Chemically-Synthesized Tetrahedrite Nanoparticles as Building Blocks"日本化学会第 99 春季年会, 16-19 March 2019, 甲南大学, 神戸, 兵庫.
10. T. Nakada, C. Shijimaya, M. Takahashi, **W. Zhou**, D. Mott, M. Ohta, T. Akatsuka, H. Ono, and S. Maenosono: "Chemical Synthesis of Tetrahedrite Nanoparticles as Building Blocks for Sustainable Thermoelectrics" 日本化学会第 98 春季年会, 20-23 March 2018, 日本大学理工学部, 船橋, 千葉.
11. 中田 豪, 四十万谷 智子, 東嶺 孝一, 高橋 麻里, **周 薇**, P. Dwivedi, D. Mott, 太田 道広, 赤塚 威夫, 三輪 大, 小野 博信, 宮田 全展, 前之園 信也: "サステイナブル熱電変換材料に向けたテトラヘドライトナノ粒子の合成と評価" 第 15 回日本熱電学会学術講演会, 13-15 September 2018, 東北大学, 仙台, 宮城.

Poster presentation

1. **W. Zhou**, P. Dwivedi, K. Higashimine, M. Miyata, M. Ohta, H. Takida, T. Akatsuka, and S. Maenosono: "Structure-Property Relations in Thermoelectric Nanobulk Materials Fabricated from Cu_2SnS_3 Nanoparticles" 38th Annual International Conference on Thermoelectrics and 4th Asian Conference on Thermoelectrics (ICT/ACT2019), 30 June - 4 July 2019, Hwabaek International Convention Center, Gyeongju, South Korea.
2. **W. Zhou**, A. Ito, C. Shijimaya, K. Higashimine, M. Ohta, M. Miyata, D. Mott, T. Akatsuka, H. Ono, M. Koyano, and S. Maenosono:" $Cu_2Sn_{1-x}M_xS_3$ Nanoparticles for Sustainable Thermoelectrics" The 15th International Conference on Advamced Materials (IUMRS-ICAM 2017), 27 August - 1 September 2017, Yoshida Campus, Kyoto University, Kyoto, Japan.
3. **W. Zhou**, C. Shijimaya, K. Higashimine, M. Ohta, M. Miyata, D. Mott, T. Akatsuka, H. Ono, M. Koyano, and S. Maenosono: " $Cu_2Sn_{1-x}M_xS_3$ (M=Zn, Fe) Nanoparticles for Sustainable Thermoelectrics" The IRAGO Conference 2017, 1-2 November 2017, The University of Electro-Communications, Tokyo, Japan.
4. **W. Zhou**, C. Shijimaya, P. Dwivedi, T. Nakada, M. Takahashi, D. Mott, M. Koyano, M. Ohta, H. Miwa, T. Akatsuka, H. Ono, and S. Maenosono:"Nanostructured Thermoelectric Material Composed of Heterogeneous $Cu_2Sn_{1-x}Zn_xS_3$ Nanoparticles"ナノ学会第 16 回大会, 10-12 May 2018, 東京大学武田先端知ビル, 東京.
5. **W. Zhou**, C. Shijimaya, P. Dwivedi, T. Nakada, M. Takahashi, D. Mott, M. Koyano, M. Ohta, H. Miwa, T. Akatsuka, H. Ono, and S. Maenosono: "Thermoelectric Properties of Mixed Phase $Cu_2Sn_{1-x}Zn_xS_3$ Heterostructured Nanoparticle Material"Asian Symposium on

Nanoscience and Nanotechnology 2018, 12-14 May 2018, Takeda Building, The University of Tokyo, Tokyo.

6. T. Nakada, C. Shijimaya, M. Takahashi, **W. Zhou**, D. Mott, M. Ohta, T. Akatsuka, H. Ono, and S. Maenosono:"Polyol Mediated Synthesis and Characterization of Tetrahedrite Nanoparticles for Sustainable Thermoelectrics" The 3rd International Conference on Polyol Mediated Synthesis (IC-PMS 2018), 25-27 June 2018, Instituto de Ciencia de Materiales de Madrid, Madrid, Spain.
7. 中田 豪, 四十万谷 智子, 高橋 麻里, **周 薇**, モット デリック, 太田 道広, 赤塚 威夫, 小野 博信, 前之園 信也: "サステイナブル熱電変換材料に向けたテトラヘドライトナノ粒子の合成と評価" 応用物理学会第 65 回春季講演会, 17-20 March 2018, 早稲田大学, 新宿, 東京.
8. T. Nakada, C. Shijimaya, M. Takahashi, **W. Zhou**, M. Ohta, D. Mott, T. Akatsuka, H. Ono, and S. Maenosono: "Chemical Synthesis of Tetrahedrite Nanoparticles as Building Blocks for Sustainable Thermoelectrics" The IRAGO Conference 2017, 1-2 November 2017, The University of Electro-Communications, Tokyo, Japan.